

V72-23947

NASA CR-120921

GASL TR-771

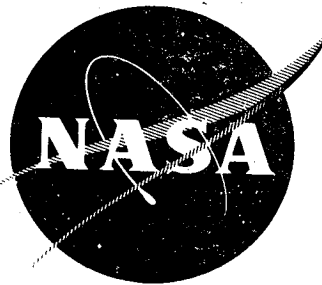
**CASE FILE
COPY**

ANALYTICAL STUDY OF GRAVITY EFFECTS

ON LAMINAR DIFFUSION FLAMES

by R. B. Edelman, O. Fortune, and G. Weilerstein

GENERAL APPLIED SCIENCE LABORATORIES, INC.



prepared for

NATIONAL AERONAUTICS AND SPACE ADMINISTRATION

NASA Lewis Research Center
Contract NAS3-14378

Report No. NASA CR-129021		2. Government Accession No.		3. Recipient's Catalog No.	
Title and Subtitle ANALYTICAL STUDY OF GRAVITY EFFECTS ON LAMINAR DIFFUSION FLAMES				5. Report Date February 1972	
				6. Performing Organization Code	
Author(s) R. B. Edelman, O. Fortune and G. Weilerstein				8. Performing Organization Report No. GASL TR-771	
				10. Work Unit No.	
Performing Organization Name and Address General Applied Science Laboratories, Inc. Merrick & Stewart Avenues Westbury, New York 11590				11. Contract or Grant No. NAS 3-14378	
				13. Type of Report and Period Covered 6/2/71-1/2/72 Contractor Report	
Sponsoring Agency Name and Address National Aeronautics and Space Administration Washington, D. C.				14. Sponsoring Agency Code	
Supplementary Notes Project Manager, Mr. Thomas Cochran					
<p>Abstract A mathematical model is presented for the description of axisymmetric laminar-jet diffusion flames. The analysis includes the effects of inertia, viscosity, diffusion, gravity and combustion. These mechanisms are coupled in a boundary layer type formulation and solutions are obtained by an explicit finite difference technique. A dimensional analysis shows that the maximum flame width radius, velocity and thermodynamic state characterize the flame structure. Comparisons with experimental data showed excellent agreement for normal gravity flames and fair agreement for steady state low Reynolds number zero gravity flames. Kinetics effects and radiation are shown to be the primary mechanisms responsible for this discrepancy. Additional factors are discussed including ellipticity and transient effects.</p>					
7. Key Words (Suggested by Author(s)) laminar combustion diffusion flame gravity viscosity inertia				18. Distribution Statement Unclassified - Unlimited	
9. Security Classif. (of this report) Unclassified		20. Security Classif. (of this page) Unclassified		21. No. of Pages 136	
				22. Price \$3.00	

* For sale by the National Technical Information Service, Springfield, Virginia 22151

1. The first part of the document is a list of names and addresses of the members of the committee. The names are listed in alphabetical order, and the addresses are given below each name. The list includes names such as Mr. J. H. Smith, Mr. W. B. Jones, and Mr. C. D. Brown, among others.

2. The second part of the document is a list of the names of the members of the committee who have been elected to the office of Chairman. The names are listed in alphabetical order, and the addresses are given below each name. The list includes names such as Mr. J. H. Smith, Mr. W. B. Jones, and Mr. C. D. Brown, among others.

3. The third part of the document is a list of the names of the members of the committee who have been elected to the office of Secretary. The names are listed in alphabetical order, and the addresses are given below each name. The list includes names such as Mr. J. H. Smith, Mr. W. B. Jones, and Mr. C. D. Brown, among others.

4. The fourth part of the document is a list of the names of the members of the committee who have been elected to the office of Treasurer. The names are listed in alphabetical order, and the addresses are given below each name. The list includes names such as Mr. J. H. Smith, Mr. W. B. Jones, and Mr. C. D. Brown, among others.

5. The fifth part of the document is a list of the names of the members of the committee who have been elected to the office of Auditor. The names are listed in alphabetical order, and the addresses are given below each name. The list includes names such as Mr. J. H. Smith, Mr. W. B. Jones, and Mr. C. D. Brown, among others.

6. The sixth part of the document is a list of the names of the members of the committee who have been elected to the office of Clerk. The names are listed in alphabetical order, and the addresses are given below each name. The list includes names such as Mr. J. H. Smith, Mr. W. B. Jones, and Mr. C. D. Brown, among others.

7. The seventh part of the document is a list of the names of the members of the committee who have been elected to the office of Librarian. The names are listed in alphabetical order, and the addresses are given below each name. The list includes names such as Mr. J. H. Smith, Mr. W. B. Jones, and Mr. C. D. Brown, among others.

8. The eighth part of the document is a list of the names of the members of the committee who have been elected to the office of Steward. The names are listed in alphabetical order, and the addresses are given below each name. The list includes names such as Mr. J. H. Smith, Mr. W. B. Jones, and Mr. C. D. Brown, among others.

9. The ninth part of the document is a list of the names of the members of the committee who have been elected to the office of Reader. The names are listed in alphabetical order, and the addresses are given below each name. The list includes names such as Mr. J. H. Smith, Mr. W. B. Jones, and Mr. C. D. Brown, among others.

10. The tenth part of the document is a list of the names of the members of the committee who have been elected to the office of Scribe. The names are listed in alphabetical order, and the addresses are given below each name. The list includes names such as Mr. J. H. Smith, Mr. W. B. Jones, and Mr. C. D. Brown, among others.

TABLE OF CONTENTS

	Page
1. SUMMARY	1
2. INTRODUCTION	2
3. ANALYTICAL MODEL FORMULATION	4
a. Fickian Diffusion	8
b. Multicomponent Diffusion	11
c. Turbulent Transport	16
d. Combustion Model	16
e. Boundary Conditions	18
4. APPLICATION OF THE MODEL	19
a. Fickian Diffusion	19
b. Multicomponent Diffusion	21
c. Turbulent Diffusion	22
d. Negative Buoyancy and Flow Reversal	23
5. MODEL REFINEMENTS	25
a. Kinetics Effects - Partial Oxidation	25
b. Elliptic Effects	28
c. Transient Effects	30
6. DIMENSIONAL ANALYSIS	32
7. PARAMETRIC STUDY	36
8. SUMMARY OF RESULTS	39
9. APPENDICES	42
A - FINITE DIFFERENCE SOLUTION OF THE CONSERVATION EQUATIONS	42
B - COMBUSTION MODEL	50
C - LIST OF SYMBOLS	54
REFERENCES	58
FIGURES	

1. SUMMARY

A theoretical study was performed on the effects of gravity level and environmental composition upon the structure of laminar hydrocarbon diffusion flames. The study was made on vertically oriented, axisymmetric, fully developed laminar fuel jets issuing into a quiescent atmosphere.

The mathematical formulation includes the effects of inertia, viscosity, diffusion and gravity. Combustion is treated with an equilibrium model, and both Fick's Law and multicomponent representations were used to model the diffusion process. These mechanisms were coupled in a boundary layer type formulation and the resulting equations were solved by an explicit finite difference technique.

The principal data used for comparison with the model predictions was obtained from a NASA Lewis drop tower. Flame shapes for methane under normal gravity and zero gravity conditions were provided by color photography. The Reynolds number based on fuel jet conditions ranged from approximately 5 to 300. The remaining data were obtained from the literature and were limited to normal gravity conditions. A dimensional analysis shows that the flame structure is characterized by the maximum flame width radius, velocity and thermodynamic state. With the aid of the theoretical model these properties have been related to their counterparts at the jet exit plane.

The comparison between theory and experiment for steady state flames showed excellent agreement for all normal gravity flames while under zero gravity conditions the predictions at the lower Reynolds numbers showed generally wider flames than were observed. The absence of kinetics and radiation effects was shown to be the primary cause for this difference between theory and experiment. The addition of partial oxidation models in the formulation substantiated this conclusion while the experimentally observed "orange-reddish" colors lent credence to the presence of soot and "cool," or slow oxidation, zones within the flames.

2. INTRODUCTION

The structure of laminar diffusion flames has been the subject of investigation for a great many years. Applications include energy utilization with interest expanding more recently to include the general problem of fire hazards. It is the latter problem that we are most interested in here. In this connection the ignition and propagation of the fires will invariably occur in a quiescent or very low velocity environment where the basic combustion process does indeed involve laminar flow. Moreover, our specific interest is in fires aboard spacecraft where the effects of gravity level and environmental composition in terms of oxygen concentration are crucial additional considerations.

A review of the existing literature shows that in each case a significant gap exists between the particular set of experimental data and the isolated correlations that have been attempted. The gap is in establishing a basic understanding of the structure of laminar diffusion flames in terms of first principles. That is, there has been a dearth of systematic mathematical modeling on this problem.

The recent work of References 1 and 2 has adequately summarized the state-of-the-art regarding such mathematical modeling of laminar diffusion flames. The existing work may be categorized in terms of (1) semi-empirical approaches based upon correlation of specific data typified by the work of References 3 and 4; and (2) special solutions of the conservation equations typified by References 5 and 6.

The semi-empirical approaches were ground-breaking works but nevertheless produced correlations which differ in functional dependence between the various authors. Thus, while attempting to provide an understanding of the problem, a degree of confusion and misleading conclusions have resulted. This is typified by the recent work of Reference 7, where a combination of attempts to extend existing correlations with the aid of heuristic arguments concludes that the laminar diffusion flame does not depend explicitly upon a Reynolds number. The result of this is a prediction of flame length as a function of gravity level which is just the opposite of what is in fact observed!

Common to the special solutions of the conservation equations is the absence of the gravity force while the assumption of similar solutions is also made. Specifically, Burke and Schumann, Reference 5, developed a classical solution for a ducted diffusion flame assuming uniform constant velocity and constant coefficients. This reduced the problem to one of solving the single homogeneous linear partial differential equation for an element mass fraction characterizing the fuel. The solution of such an equation is relatively simple but it does not contain the mechanisms that are necessary to characterize the true structure of diffusion flames. More importantly, the benefit of obtaining a simple solution in this manner precludes systematic extensions necessary to build a more realistic model. Reference 6 treats the unbounded laminar diffusion flame and solutions are obtained assuming similarity while gravity effects are neglected. Again, the limitations are analogous to these associated with the Burke-Schumann problem.

What has been required is an approach which at the start recognizes the mechanisms which are of potential importance while providing a basis necessary to readily and systematically extend the model to include additional mechanisms. Specifically, the coupling of velocity, thermal and chemical species fields, is needed. Furthermore, the mechanisms which influence their behavior must be coupled together within an analytical framework of sufficient generality so that such primitive assumptions including similarity and constant transport properties are not dictated by the solution technique and as such are not required.

This report is devoted to the development of a mathematical model and solution technique which is designed to provide the generality needed to gain a basic understanding of laminar diffusion flames influenced by gravity. The approach involves a finite difference solution of the describing partial differential equations for mass, momentum and energy applied to a basic vertical axisymmetric fuel jet configuration.

This approach recognizes that the velocity, temperature and concentration fields are dependent upon each other while the finite difference solution eliminates restrictions on the generality of the boundary conditions as well as providing a framework which may be readily extended without requiring a new solution technique to be developed from scratch. The effects included are: diffusion, inertia, viscosity, combustion and gravity.

The work described in this report includes the mathematical formulation, a comparison of the theory with experiments, a dimensional analysis, and a parametric study. In addition, a critical evaluation of the weaknesses of the model is given and a delineation of model refinements is presented.

3. ANALYTICAL MODEL FORMULATION

A schematic of the flow field of the vertical laminar jet is shown in Figure 1. The flow is axisymmetric and for now is viewed in a steady state configuration. The fuel jet velocity profile will generally be nonuniform and for fully developed laminar flow will be parabolic. The pure fuel case involves a flat (constant) concentration profile across the jet. Similarly, for an adiabatic tube ($T_o = T_e$) the fuel temperature will be constant across the tube. Thus, even if the mechanisms forcing the respective development of the velocity, temperature and species, fields were similar, there is non-similarity in these boundary conditions ruling out, in general, similar solutions.

Now, the velocity, temperature, and species fields are controlled by the distribution of momentum, energy and mass.

Momentum. - The fuel is injected at some finite velocity into the quiescent surroundings. The velocity difference produces a shear force resulting in an interchange of momentum between the fuel jet and its surroundings. This tends to equalize the velocities which in our case means a deceleration of the fuel velocity toward zero. This process of diffusive transport of momentum causes the jet to spread and entrain environmental gas into the mixing region. Simultaneously, a pressure nonuniformity develops due, in general, to the velocity variations and due to any environmental pressure variation impressed upon the mixing zone. This may be "favorable" (causing acceleration) or "adverse" (causing deceleration). In the jet problem it is instructive to consider the "impressed" pressure variation only, assuming that the static pressure is radially invariant and the flow is boundary-layer like. In this case the local pressure gradient (in the axial direction) is equal to the

pressure gradient in the environment. This is a favorable pressure gradient since it is equal to the gravity force ($-g\rho$). The combination of pressure gradient and local gravity force yields the "buoyant" force and will cause an acceleration of the flow for $(\rho_e - \rho) > 0$. Note, however, that the value of the buoyant force can be locally negative. Thus, in the near jet fuel rich, cool region, away from the flame front, the "buoyant" force will be negative for heavier-than-air fuels such as butane. This can result in stagnating the flow locally with the attendant formation of a recirculation zone. This will be discussed later in connection with a comparison of our model with Wohl's experiments (Reference 4). For light fuels like methane, the buoyant force is always positive. This is of particular interest in connection with the recent work, previously mentioned, by Cochran and Masica, References 1 and 2.

Thus, there are three direct effects upon the velocity field: (a) shear or molecular diffusion of momentum, (b) pressure gradient, and (c) gravity, where (b) and (c) combine to give the buoyant force in the jet problem.

Energy. - The temperature field is affected by several processes. In the vertical jet problem the convection of energy is a primary mode of energy transport and therefore depends upon those mechanisms which alter the velocity field. In general the velocity field can alter the thermal field directly through viscous dissipation and by the rate at which non-dissipative pressure work is done. These effects are negligible in our low speed problem. Additional mechanisms in the jet problem which will be shown to be most important are the heat release rate due to combustion, the heat conduction away from the flame front, and the energy transported due to diffusion of species. Thus, the temperature field also depends upon composition in terms of its effect upon density, specific heat, the transport coefficients as well as the direct effect upon the species production rate, \dot{W}_i , which is an exponential function of temperature.

Species Diffusion. - The concentration field is affected by the convection of species through the flow and therefore by the velocity field. The mechanisms which directly "force" changes in a given specie are the chemical production rate of that specie and the diffusion of that specie. As the fuel comes into contact with the environmental gas the resulting concentration gradients produce a diffusional flux of environmental gas into the fuel (and fuel diffuses outward into the environment). These diffusional

gradients produce an air/fuel ratio distribution ranging from fuel rich on the axis ($x \leq L$, Figure 1) to fuel lean in outer regions of the mixing zone. The surface upon which the equivalence ratio is unity will correspond to the maximum temperature in the flow field and is referred to as the "flame front."

The primary assumption is that diffusive processes are important only in the radial direction.

Governing equations. - The development of an analytical tool can serve in several ways: (1) provide direct predictions, (2) interpret experimental data and (3) provide the basis for meaningful dimensionless parameters which characterize the process and as such can aid in organizing experimental data. The first two aspects are an inherent part of a formulation written directly in terms of the variables of the problem in dimensional form. To aid in achieving the latter aspect from a basic formulation it is helpful to introduce appropriate characteristic quantities and thereby non-dimensionalize the describing equations. It is customary practice to do this by normalizing the variables directly in terms of the boundary conditions. However, it will be shown here that the resulting dimensionless groups do not truly characterize the process and that this is due to the large variation in flow properties throughout the domain of interest. Accordingly, the current approach involves the introduction of a set of characteristic quantities which are based upon some state within the flow that more accurately reflects the flame structure. Although this study has shown that the state of flow at the maximum flame width point (including the flame radius and velocity) is appropriate, the development given here is general. For this purpose the following variables are introduced:

$$\begin{aligned}
 \bar{u} &\equiv u/u^* & \bar{x} &\equiv x/r^* \\
 \bar{r} &\equiv r/r^* & \bar{\mu} &\equiv \mu/\mu^* \\
 \bar{\rho} &\equiv \rho/\rho^* & \Delta\phi &\equiv \frac{\bar{\rho}_e - \bar{\rho}}{\bar{\rho}_e - 1} = \frac{\rho_e - \rho}{\rho_e - \rho^*} \\
 \bar{H} &\equiv H/H^* \\
 \bar{v} &\equiv v/u^*
 \end{aligned}
 \tag{1}$$

Where, as cited above, the starred quantities are evaluated at a point in the flow which best characterizes the process.

Assuming (1) that diffusive processes are important only in the direction normal to the primary flow direction, (2) that combustion is diffusion controlled, and (3) that the flow is steady and axisymmetric, the describing equations in non-dimensional form are:

Continuity

$$\frac{\partial(\bar{\rho}\bar{u}\bar{r})}{\partial\bar{x}} + \frac{\partial(\bar{\rho}\bar{v}\bar{r})}{\partial\bar{r}} = 0 \quad (2)$$

Momentum

$$\begin{aligned} \bar{\rho}\bar{u} \frac{\partial\bar{u}}{\partial\bar{x}} + \bar{\rho}\bar{v} \frac{\partial\bar{u}}{\partial\bar{r}} &= \left(\frac{1}{Re}\right) \frac{1}{\bar{r}} \frac{\partial(\bar{\mu}\bar{r}\partial\bar{u}/\partial\bar{r})}{\partial\bar{r}} \\ &+ \left(\frac{Gr}{Re^2}\right) \bar{\Delta}\bar{\rho} \end{aligned} \quad (3)$$

Diffusion of Elements

$$\bar{\rho}\bar{u} \frac{\partial\bar{\alpha}^l}{\partial\bar{x}} + \bar{\rho}\bar{v} \frac{\partial\bar{\alpha}^l}{\partial\bar{r}} = - \left(\frac{1}{Re}\right) \frac{1}{\bar{r}} \frac{\partial(\bar{r}\bar{J}^l)}{\partial\bar{r}} \quad (4)$$

Energy

$$\bar{\rho}\bar{u} \frac{\partial\bar{H}}{\partial\bar{x}} + \bar{\rho}\bar{v} \frac{\partial\bar{H}}{\partial\bar{r}} = \left(\frac{1}{Re}\right) \frac{1}{\bar{r}} \frac{\partial}{\partial\bar{r}} \left\{ \frac{\bar{\mu}\bar{r}}{Pr} \frac{\partial\bar{h}}{\partial\bar{r}} - \bar{r} \sum_k (\bar{h}^k \bar{j}^k) \right\} \quad (5)$$

where the above parameters: Reynolds, Grashof numbers are defined as:

$$\begin{aligned} Re &= \frac{\rho^* u^* r^*}{\mu^*} = \text{Reynolds No.} & Gr &= \frac{\rho^* r^{*3} g}{\mu^*} \left(\frac{\rho_e - \rho^*}{\rho^*} \right) = \\ & & &= \text{Grashof No.} \end{aligned} \quad (6)$$

To complete the description of the problem in terms of the basic variables, $(u, T \text{ and } \alpha^k)$, additional relations are required. Specifically, the equations of state, expressions for the diffusional fluxes, j^k and \tilde{j}^l , and the definition of the chemical state in terms of a combustion model, are needed. These are described below:

Equations of State

$$\rho = \frac{p}{RT \sum_i \alpha^i / w^i} \quad ; \quad i = \text{all gaseous species} \quad (7)$$

$$h = \sum_k \alpha^k h^k \quad (8)$$

where

$$h = H - u^2/2 \quad (9)$$

Diffusional Fluxes, j^k and \tilde{j}^l

For laminar flows both Fick's Law and multicomponent models have been employed to express the diffusional fluxes in terms of the basic properties of the flow. The Fickian model is simple and can be expected to be adequate under conditions where the diffusing gases do not differ significantly in their respective molecular weights. The multicomponent representation is algebraically complex and expresses the direct coupling of each diffusional flux to the entire species field. This model is potentially more accurate than Fick's Law, depending upon how well the set of binary diffusion coefficients are known.

a. Fickian Diffusion

Assuming that all diffusion coefficients, D_{kj} , are equal, is equivalent to reducing the mixture to a set of binary subsystems comprised of the specie of interest and the remaining mixture. The diffusional mass flux for the k^{th} specie is then given by:

$$j^k = - \rho \bar{D} \frac{\partial \alpha^k}{\partial \bar{r}} \quad (10)$$

For this case it is possible to define a Schmidt number such that

$$j^k = - \frac{\mu}{Sc} \frac{\partial \alpha^k}{\partial \bar{r}} \quad (11)$$

or

$$j^k = - \frac{\mu^*}{Scr^*} \bar{\mu} \frac{\partial \alpha^k}{\partial \bar{r}}$$

and

$$\bar{j}^k = - \frac{1}{Sc} \bar{\mu} \frac{\partial \alpha^k}{\partial \bar{r}} \quad (12)$$

The corresponding diffusional mass flux for each ℓ element is given by:

$$\bar{\tilde{j}}^\ell = - \frac{1}{Sc} \bar{\mu} \frac{\partial \tilde{\alpha}^\ell}{\partial \bar{r}} \quad (13)$$

where

$$\tilde{\alpha}^\ell = \sum_k \bar{\nu}^{k\ell} \frac{w_k^\ell}{w_k} \alpha^k \quad (14)$$

so that

$$\bar{\tilde{j}}^\ell = \sum_k \bar{\nu}^{k\ell} \frac{w_k^\ell}{w_k} j^k \quad (15)$$

and $\bar{\nu}^{k\ell}$ is the amount of element ℓ in specie k . Now, substitution of Eqs. (12) and (13) into the above conservation equations introduces the Schmidt Number as an additional parameter, where Sc = ratio of diffusivity of momentum to the diffusivity of mass. Thus, the working forms of the element and energy conservation equations are given by:

$$\bar{\rho} \bar{u} \frac{\partial \tilde{\alpha}^l}{\partial \bar{x}} + \bar{\rho} \bar{v} \frac{\partial \tilde{\alpha}^l}{\partial \bar{r}} = \frac{1}{\text{ReSc}} \frac{1}{\bar{r}} \frac{\partial}{\partial \bar{r}} \left(\bar{r} \bar{\mu} \frac{\partial \tilde{\alpha}^l}{\partial \bar{r}} \right) \quad (16)$$

and

$$\bar{\rho} \bar{u} \frac{\partial \bar{H}}{\partial \bar{r}} + \bar{\rho} \bar{v} \frac{\partial \bar{H}}{\partial \bar{r}} = \frac{1}{\text{Re}} \frac{1}{\bar{r}} \frac{\partial}{\partial \bar{r}} \left\{ \bar{\mu} \bar{r} \left[\frac{1}{\text{Pr}} \frac{\partial \bar{h}}{\partial \bar{r}} + \frac{1}{\text{Sc}} \sum_k \bar{h}^k \frac{\partial \alpha^k}{\partial \bar{r}} \right] \right\} \quad (17)$$

As part of the "simple" transport mechanism model the Schmidt Number and Prandtl Number are treated as specified quantities. This reduces the problem of transport property definition to that of specifying a relationship between the absolute viscosity, μ , and the local thermodynamic properties. For this purpose the Sutherland Law is used based upon the properties for air:

$$\mu = \frac{1.458 \times 10^{-6} T^{1.5}}{T + 110.4} \left(\frac{\text{kg}}{\text{m-sec.}} \right) \quad (18)$$

where T is in $^{\circ}\text{K}$. Although this expression is for air (independent of the actual composition) the primary dependence upon temperature is retained. The differences that do exist between the levels of viscosity predicted by the Sutherland Law and the actual values associated with, say, pure fuel, air and products of combustion are found to have some effect upon the accuracy of the flame structure predictions but not to the extent of altering the conclusions regarding the mechanisms responsible for the particular flame behavior. Nevertheless, to provide a quantitative measure of the potential improvement in the accuracy of the predictions, a detailed transport property model including multicomponent diffusion, has been developed.

b. Multicomponent Diffusion

As cited above, potential improvements in the accuracy of the predictions are afforded by a detailed transport property representation. The improvements can be expected to be most significant at low Reynolds Number and at low g-levels where diffusive processes dominate, and for chemical systems where the dominant species vary significantly in their respective molecular weights.

For non-equal diffusion coefficients the generalized multicomponent diffusion formulation given in Reference 8 is appropriate. In terms of mass fractions, α^k , the required relations are given by:

$$\frac{1}{\rho} \sum_{j=1}^N \frac{1}{w_j} \frac{\partial}{\partial r} (\alpha_j^k - \alpha_j^k) = \sum_{j=1}^N \frac{1}{w_j} (\alpha_j \frac{\partial \alpha^k}{\partial r} - \alpha^k \frac{\partial \alpha_j}{\partial r}) \quad (19)$$

and

$$\sum_{j=1}^N j^j = 0 \quad (20)$$

where N is the number of species. Equation (19) provides N-1 independent relations for the j^k diffusional mass fluxes and Eq. (20) completes their description. The diffusional mass fluxes for the elements are related to corresponding species fluxes, those relations of the type given by Eq. (15), viz.

$$\tilde{j}^l = \sum_k \nu^{kl} \frac{w^l}{w_k} j^k \quad (21)$$

The details of the matrix inversion technique and the coupling to the conservation equations are described in Appendix A. To accomplish the desired solution certain information is required by Eqs. (19) and (20). Specifically, the mass fractions, their gradients and the density must be known.

These are, in fact, determined in the course of generating the flow field as discussed in detail in Appendix A. In addition, the δ_{kj} must be specified and these are determined based upon the kinetic theory analysis given in Reference 8, viz;

$$\delta_{kj} = \frac{2.663 \times 10^{-2} T^{1.5}}{P \Omega_{kj}^{(1,1)}} \Gamma_{kj} \left(\frac{m}{sec} \right) \quad (22)$$

Where $[T] = ^\circ K$, and $[P] = \frac{N}{m^2}$

In addition,

$$\Gamma_{kj} = \frac{1}{\sigma_{kj}^2} \sqrt{\frac{W_k + W_j}{2W_k W_j}} \quad (23)$$

with the collision cross-section given by:

$$\sigma_{kj} = \frac{\sigma_k + \sigma_j}{2} \quad (24)$$

Finally, the collision integral, $\Omega_{kj}^{(1,1)}$, as tabulated in Reference 8 as a function of the reduced τ_{kj} temperature, T/ϵ_{kj} , has been curve fit for the present application. The resulting equation is given by:

$$\Omega_{kj}^{(1,1)} = 1.5146 - 0.62499 \tau_{kj} + 0.10023 \tau_{kj}^2 \quad (25)$$

Where,

$$\tau_{kj} = \ln (T/\epsilon_{kj}) \quad (26)$$

and

$$\epsilon_{kj} = \sqrt{\epsilon_k \epsilon_j} \quad (^\circ K) \quad (27)$$

The required properties for the participating species are given in Table I, below.

Now, consistent with this detailed computation of the diffusion coefficients, both the viscosity, μ , and the conductivity, λ , are computed using the following mixture rules, Reference 8.

Viscosity

$$\mu = \sum_{k=1}^N \frac{\alpha_k \mu_k}{\alpha_k + \sum_{\substack{j=1 \\ j \neq k}}^N \frac{[1 + \beta_{kj} \sqrt{\frac{\mu_k}{\mu_j}}]^2}{\gamma_{kj}}} \alpha_j \quad (28)$$

where

$$\beta_{kj} = \left(\frac{w_j}{w_k} \right)^{\frac{1}{4}} \quad (29)$$

and

$$\gamma_{kj} = \frac{w_j}{w_k} \sqrt{8 \left(1 + \frac{w_k}{w_j} \right)} \quad (30)$$

with

$$\mu_k = \frac{2.6693 \times 10^{-6} \sqrt{TW^k}}{\sigma_k^2 \Omega_k(2,2)} \left(\frac{\text{kg}}{\text{m-sec}} \right) \quad (31)$$

and,

$$\Omega_k^{(2,2)} = 1.6507 - 0.6688 \tau_k + 0.10725 \tau_k^2 \quad (32)$$

where $\Omega_k^{(2,2)}$ has been curve fit from the tabulation given in Reference 8.

TABLE I

CONSTANTS FOR TRANSPORT PROPERTY CALCULATIONS

<u>GAS</u>	<u>W</u>	<u>σ (Å)</u>	<u>ϵ (°K)</u>
H ₂ O	18.016	2.641	809.1
H ₂	2.016	2.827	59.7
O ₂	32.	3.467	106.7
CO	28.011	3.69	91.7
CO ₂	44.011	3.941	195.2
N ₂	28.016	3.798	71.4
CH ₄ *	16.043	3.758	148.6
C (gas)	12.011	3.385	30.6

* Constants for other fuels are available for input.

Thermal Conductivity

The mixture rules for the thermal conductivity are given by:

$$\lambda = \sum_{k=1}^{N \text{ gases}} \left[\frac{a_k \lambda'_k}{a_k + \sum_{\substack{j=1 \\ j \neq k}}^N a_j n_{kj} \zeta_{kj}} + \frac{a_k \lambda''_k}{a_k + \sum_{\substack{j=1 \\ j \neq k}}^N a_j n_{kj}} \right] \frac{\text{Joule}}{(\text{m-sec-}^\circ\text{K})} \quad (33)$$

where

$$\lambda'_k = 3.75 \frac{\tilde{R}}{W_k} \mu_k \quad (34)$$

and

$$\lambda''_k = \lambda'_k \frac{[0.352 C_p^k W_k^k - 0.88]}{\tilde{R}} \quad (35)$$

with

$$\tilde{R} = 8.3143 \times 10^3 \frac{(\text{J})}{\text{kgm-mole } ^\circ\text{K}} \quad (36)$$

and

$$n_{kj} = \frac{\left[1 + \sqrt{\frac{\lambda'_k}{\lambda'_j}} \beta_{kj} \right]^2}{\gamma_{kj}} \quad (37)$$

$$\zeta_{kj} = 1 + \frac{2.41 (W_k - W_j) (W_k - 0.142 W_j)}{(W_k + W_j)^2} \quad (38)$$

Note that

$$\tilde{J}^k = \sum_k \nu^{kl} \frac{W^l}{W^k} J_k$$

c. Turbulent Transport

Although the emphasis in the current study is on the structure of laminar flames, certain of the available experimental data extends into the transitional and fully developed turbulent regimes, References 4 and 9. In order to provide a means of interpreting some of these data, provision has been made in the model to account for turbulent exchange of mass, momentum, and energy. The approach here involves replacing the laminar transport properties with their turbulent counterparts. In this regard the Fickian framework is employed and with the specification of "turbulent" Schmidt and Prandtl numbers (usually taken equal to unity) the problem reduces to modeling the eddy viscosity. Based upon previous work, Reference 10, the following model has been found to be adequate:

$$\mu_t = k r_{1/2} (\rho u) \epsilon \quad (39)$$

where k is an empirical constant and $r_{1/2}$ is a measure of the scale of turbulence and is taken at the radius where the mass flux, (ρu) , is at its average value.

Applications of the Fick's Law, multicomponent diffusion and turbulent property transport representations are discussed in the subsequent sections in connection with the predictions of flame structure.

d. Combustion Model

An assumption which has been employed in simple treatments of diffusion flames is that all the heat is released on the surface where the fuel/air ratio is stoichiometric (Reference 6). This "flame sheet" assumption is extremely restrictive and is not necessary. Its use is generally coupled to similar solution techniques where accuracy is sacrificed strictly for the sake of mathematical simplification. A more accurate combustion model is offered in terms of basic equilibrium theory. In a diffusion flame the application of this theory leads to

a "local" equilibrium state at each point within the flow field. Thus, a solution of the conservation equations, Eqs. (2), (3), (4) and (5), provides the velocity, element mass fractions and total enthalpy at a known local pressure level. Of this information the element mass fractions, static enthalpy and pressure, define the chemical equilibrium state. This includes the mass fractions and static temperature. Because the flow field is nonuniform the local point-by-point equilibrium condition is referred to as "shifting" equilibrium. The advantages of using shifting equilibrium are that, (1) it is not complex, and (2) dissociation can be accounted for. This technique has already been successfully applied in connection with application to diffusion flames (Reference 10).

Now, in considering the potential adequacy of an equilibrium combustion model, the basic consideration was the residence time within the diffusion flames. It is shown later that the characteristic residence times for the data analyzed in this report are typically of the order of 10 milliseconds.

Experience at GASL with hydrocarbon-air finite rate chemistry models (c.f. References 11 and 12) verified that the above characteristic times are generally in excess of the combustion times required for hydrocarbons at the temperatures and pressures encountered in the flame. For example, Figure 2 of Reference 11 shows the ignition delay and total reaction times for a methane-air combustion process where it is important to note that the ignition delay and reaction times for most gaseous hydrocarbons, and certainly for hydrogen, are shorter than that of methane. Hence, it would appear to be adequate to employ an equilibrium chemistry model to describe most normal gravity flames and stable zero gravity flames of interest in this report. Of course, the logic leading to this conclusion is based upon (1) that the temperature levels are, in fact, of the order of 2000°K, and (2) that the reaction times for "hot" combustion in premixed systems are meaningful for diffusive flames.

The basic model employed in this work was developed from the results of detailed equilibrium computations for hydrocarbon combustion. The features of the model are described in Appendix B. The adequacy of the model in representing detailed equilibrium predictions is summarized in Figures 3 and 4. For our current applications, typified by the lower initial temperature, Figure 3, the agreement is quite good over the entire equivalence ratio range. Although not crucial to the current study, it should be noted that for higher initial temperatures, dissociation effects become significant and the agreement is relatively poor in the near stoichiometric regime, Figure 4.

e. Boundary Conditions

The following conditions represent the boundary conditions required to set the problem for the steady axisymmetric vertical jet flow in an infinite environment:

$$0 \leq r \leq r_j \quad \left\{ \begin{array}{l} @ x = 0 \\ H = H_o(r) \\ u = u_o(r) \\ \alpha_i = \alpha_{io}(r) = 1 \text{ for pure fuel} \\ v = 0 \end{array} \right. \quad \begin{array}{l} \text{Note: Arbitrary initial} \\ \text{profiles may be specified} \\ \text{including parabolic for} \\ \text{the velocity.} \end{array} \quad (40)$$

$$r > r_j \quad \left\{ \begin{array}{l} H = H_e \\ u = u_e \quad \{u_e = 0 \text{ for the quiescent environment} \\ \alpha_i = \alpha_{ie} \end{array} \right. \quad (41)$$

$$@ x \geq 0$$

$$r \rightarrow \infty \quad \left\{ \begin{array}{l} u = 0 \\ H = H_e \\ \alpha_i = \alpha_{ie} \end{array} \right. \quad (42)$$

$$r = 0 \quad \left\{ \begin{array}{l} \frac{\partial u}{\partial r} = \frac{\partial H}{\partial r} = \frac{\partial \alpha_i}{\partial r} = 0 \text{ (symmetry)} \\ v = 0 \end{array} \right. \quad (43)$$

where

$$H = \frac{u^2}{2} + \sum_i \alpha_i h_i \quad (44)$$

and the h_i 's are determined with specification of the temperature. In addition to the boundary conditions, the "impressed" pressure field must be specified. This is given by

$$\frac{dp_e}{dx} = - \rho_e g \quad (45)$$

In summary, the model accounts for the cross-coupling between the velocity, temperature and species fields as influenced by gravity; arbitrary transport coefficients which depend upon the local state; and shifting equilibrium combustion.

4. APPLICATIONS OF THE MODEL

a. Fickian Diffusion

The preceding discussion concentrated on the elements of a rather detailed model for diffusion flames. There are virtually no restrictions on the specification of boundary conditions and a general treatment for the transport coefficients of mass, momentum and energy is retained.

This section describes the utility of the model to (1) predict experimental observations, (2) delineate the relative importance of those mechanisms which are included in the model, (3) provide the basis for establishing meaningful characteristic parameters to aid in data interpretation and correlation, and (4) pinpoint theoretical and experimental aspects which need further consideration. The bulk of our attention during this study has been devoted to the experimental work for which both normal gravity and zero gravity data was available - namely the methane-air flames of Cochran and Masica (c.f. References 1, 2 and data supplied in a private communication from Mr. Thomas H. Cochran, June 23, 1971). To supplement this work, the normal gravity data of Wohl, et al. (Reference 4), and Hawthorne and Hottel (References 3 and 9) was examined. Also, parametric studies were made for methane-air, ethylene-air and propylene-air flames, and the results are available for comparison with future experimental work.

The first step in the application of the model was to verify that we could successfully predict the normal gravity flame lengths of Reference 1. As shown in Figure 5, good agreement was obtained between the analysis and the data for these relatively large fuel nozzle radius flames by postulating a Prandtl number of 0.8 and a Schmidt number of 0.5. It may be noted that when unity Prandtl and Schmidt numbers were assumed (for the initial conditions of Test 20, Reference 1), a theoretical flame length of twice the experimental length was obtained. When the higher fuel flow rate/smaller nozzle experimental data became available, (private communication from Mr. Thomas H. Cochran, June 23, 1971), a further comparison of theoretical and experimental flame lengths was made, as shown in Figure 6. It was found that for the higher fuel flow rates ($Q > 5 \text{ cm}^3/\text{sec}$) that the use of a Schmidt number value of 0.6 yielded better agreement with the experimental data. This value was used in all subsequent calculations. For the initial zero-g comparisons the operating conditions corresponding to the preceding normal-g methane flames were used. A comparison of flame length predictions with the experimental results for a series of normal-g and zero-g methane cases is summarized in Figure 7.

These direct comparisons show generally excellent agreement for the normal-g flames and fair agreement for the steady state 0-g flames. In particular, for these specific sets of methane cases the predicted 0-g flame lengths are generally somewhat shorter than the observed lengths. In all cases, however, the observed trends for this set of data are predicted where here the 0-g flames are longer than the normal-g flames. In addition, these buoyant flames are too complex to be treated by similar solutions, and thus analyses such as that by Goldburg and Cheng (Reference 6) are inappropriate. For example, the non-similarity of the calculated radial velocity profiles for a methane-air normal gravity flame is shown in Figure 8. In the near, cool inner region where diffusion dominates, the flow is decelerated. Then, downstream as the flow is heated due to combustion, buoyancy becomes important and the flow is accelerated.

Nevertheless, the preceding study for these 0-g flames showed that the predicted flames, based upon Fickian diffusion, were not only shorter but broader than indicated by the experiments, particularly at the lower Reynolds numbers as shown on Figure 9.

b. Multicomponent Diffusion

The theoretical calculations described in the preceding discussions were based upon the Fickian representation for diffusive transport. As cited in Section 3, the importance of detailed transport property considerations suggested the inclusion of a multicomponent diffusion model and comparisons have been made with the Fickian diffusion model and with experimental data where it was available. These comparisons are shown in Figures 10 through 13. In general it appears that for the hydrocarbon flames there are not gross differences between the multicomponent and the Fickian analyses, Figures 10 through 12. However, for the hydrogen flame there does appear to be a significant effect, Figure 13. This is to be expected since the diffusion coefficients are sensitive to the molecular weights of the chemical species. However, comparison was made using an isolated piece of normal gravity laminar data of Hawthorne (Reference 9), and shows that the Fickian flame length ($\phi = 1$) is about 150 cm while

the multicomponent prediction yields a length of between 115 and 120 cm. Although the multicomponent prediction is closer to the experimental value, L_{fe} , the agreement is still poor. Although this prediction shows the potential importance of multicomponent diffusion, the discrepancy between the prediction and the single data point needs further experimental information before this limited comparison can be truly assessed.

Furthermore, the potential importance of soot in the 0-g hydrocarbon flames dictates that a multicomponent representation be used to account for slow diffusion of the soot, particularly relative to the gaseous species.

In general, then, it is desirable to retain the multicomponent transport model for further comparisons and general refinement of the flame model as well as for further studies in connection with sooty flames.

c. Turbulent Diffusion

Although turbulent flames are not of direct concern in this study, certain available data have been analyzed to demonstrate the overall utility of the model for analyzing turbulent as well as laminar flames. For this purpose the turbulent hydrogen and propane normal gravity flame data of Hawthorne and Hottel (Reference 3) was used. The turbulent viscosity model used, as discussed above, was of the form:

$$\mu_T = K r_{1/2} (\rho u) \xi$$

As shown in Figures 14 and 15, good agreement with experimental results was obtained for both the hydrogen and the propane flames.

Thus, it appears that the same model framework may be used for laminar and turbulent flames provided that the appropriate transport property relations are employed.

d. Negative Buoyancy and Flow Reversal

In terms of overall data evaluation an interesting and rather important observation was made. In particular, a start was made in analyzing the butane-air data of Wohl, et al. (Reference 4) as reported on pp. 58-60 of Reference 13. It was found there that the experimental flame length for the highest fuel flow rates ($Re_o = 3,140$) could be reproduced by imposing a viscosity level, typical of transitional flow (laminar-to-turbulent) while for a lower fuel rate ($Re_o = 249$) the flow field calculation was terminated by the occurrence of a stagnation point indicating the start of a recirculation region. The recirculation is due to the persistence, for the heavier than air fuel, of a negative buoyancy effect in the near jet region which is equivalent to a strong adverse pressure gradient.

Upon examining the butane data of Wohl in more detail, it was found that recirculation was predicted even for fuel flow rates as high as $100 \text{ cm}^3/\text{sec}$, with initially turbulent fuel Reynolds numbers ($Re_o = 2,030$). Velocity profiles illustrating the onset of the recirculation region are shown in Figure 16. This is a very clear indication that the possibility of local recirculation for heavier than air fuels must be kept in mind, and anticipated for other "heavy" hydrocarbons.

As will be discussed below, negative Grashof number profiles were also obtained in the near region of the propylene evaluation case (where the fuel/air weight ratio was 1.59), although acceleration due to heating occurred prior to the onset of recirculation. The fact that the analysis of all of the laminar butane-air data was sensitive to and significantly affected by the negative buoyancy phenomena, suggests additional areas of importance in terms of practical applications. This includes fires not only involving fuel vapors which are heavier than air but also conditions where the flame is decelerated.

Thus, further exploration of the occurrence of recirculation is indicated.

The preceding comparisons between theory and experiment show excellent agreement between the basic Fick's Law model and the normal gravity data, while for low Reynolds number, zero gravity flames, the model yields wider steady state flames than observed. However, the inclusion of a multi-component model for diffusion provided some reduction in this discrepancy. Finally, application of the basic model to turbulent flames shows excellent agreement between theory and experiment.

Now, the excellent agreement obtained for the normal gravity flames suggested that a more detailed examination be made to determine the steps required to improve the model in the low Reynolds number, zero gravity regime. Potential mechanisms responsible for the discrepancy between the basic theory and experiment at these conditions include kinetic, elliptic and transient effects.

5. MODEL REFINEMENTS

a. Kinetics Effects - Partial Oxidation

The fact that many of the zero gravity flames were observed to have an orange-reddish appearance, seemed to indicate that significant amounts of solid carbon were being formed by pyrolysis in the fuel rich portions of these flames. In addition, such colors are typical of cool flame phenomena involving partial oxidation of the fuel. Both pyrolysis/soot formation and the cool flame oxidation process will reduce the temperature levels in the actual flames. Finally, the presence of soot in these flames will tend to further reduce the temperature levels through the mechanism of thermal radiation.

One of the principal effects of a reduction in temperature level is a decrease in the diffusion rate with an attendant reduction in flame width. To provide a means of assessing the importance of such phenomena a set of simple "partial" oxidation models have been employed. Specifically, the partial oxidation models employed were:

- (a) Fuel is burned to H_2O and $C(s)$
- (b) Fuel is burned to CO and H_2 (and $C(s)$ in the most fuel rich portion of the flame)
- (c) Fuel is burned to H_2O and CO

These models are "psuedo" complete combustion models selected such that the specification of the "element" concentration defines the species mass fractions without the need for any detailed "equilibrium" computations. As such, they are similar to the basic complete combustion model detailed in Appendix B. Of these, the first two models are the most significant since the first provides for the maximum production of solid carbon possible, and thus enables us to observe the extreme case of

total fuel pyrolysis without subsequent downstream carbon oxidation. The second model also provides for a significant reduction in the flame temperature level. Also, the limit of non-reacting, or frozen chemical flow, with the pure fuel mixing with the ambient air, was also employed to provide a "base line" (minimum mixing rate) for comparison purposes.

As may be seen in Figure 17, a dramatic reduction in theoretical flame width was obtained by using the partial oxidation models. Indeed, the theoretical results for r_m/r_o now lie within the scatter of the zero gravity steady-state flame data. More detailed information is shown in Figures 18 through 21.

The methane-air flames shown in Figures 18 and 19 (tests 7 and 8 of Private communication from Mr. Thomas H. Cochran, June 23, 1971), mark the transition between an extinguished zero gravity flame ($Q = .75 \text{ cm}^3/\text{sec}$) and an established, steady zero-g flame ($Q = 1.08 \text{ cm}^3/\text{sec}$) for .051 cm radius burner.

Figure 19 shows the experimental data together with analytic predictions made using three combustion models as designated on the figure. In addition, the stoichiometric surface is shown for a calculation made assuming no combustion. Here it is important to note that the respective maximum temperature "flame" surfaces shown correspond to stoichiometric conditions associated with the particular combustion model. The frozen flow stoichiometric surface, however, corresponds to the "complete," or full chemistry model. Now, considering the stoichiometric surface for the full chemistry model with and without combustion, it is seen that this surface becomes long and narrow, as the heat release is reduced. However, the stoichiometric surfaces, corresponding to the partial oxidation models show smaller flame radii, as desired, but also shorter flame lengths, Figure 19. This behavior is observed even for the steady state predictions of flames that actually quenched during the drop test sequence, Figure 18. These results suggest that the heat release mechanism is not a uniform one throughout the flow field. Rather, in the near jet region partial combustion producing soot and partially oxidized species dominates the reaction process while upon flowing downstream the continued heating and increased residence time provides the conditions for these species to begin to burn off. As a consequence, the

actual flame front would traverse the various "fixed" stoichiometric surfaces associated with each partial oxidation model and is consistent with the experimental observations as shown, for example, in Figure 18.

The extent to which our findings for the methane-air system can be generalized to other fuel/oxidizer/diluent systems needs to be determined. Ideally, the availability of zero gravity flame data for both hydrogen-air and high carbon to hydrogen ratio fuel systems, such as acetylene-air or propylene-air, would make it possible to isolate the contribution of the soot kinetics to the zero gravity flame quenching process. While quantitative data for the propylene-air system was not available during the course of this study, some qualitative results did become available for ethylene-air and propylene-air diffusion flames (c.f. Communication from Mr. Thomas H. Cochran to R. B. Edelman), and this encouraged us to perform certain parametric studies for these systems. In particular, it is known that unlike the methane-air flames the steady-state zero gravity propylene-air flames are smaller than the equivalent normal gravity flames. Also, it has been remarked that the ethylene and propylene flames (with a hydrogen/carbon molar ratio of 2) appear to be redder and sootier than the equivalent methane flames (with $(H)/(C) = 4$). An explanation for the shrinkage in the observed steady-state zero-g flame can be made on the basis of the partial oxidation process. As shown in Figures 20 and 21, several complete combustion chemical models were used in making both normal-g and zero-g predictions for a low fuel flow rate ($Q = .22$ cc/sec) propylene-air flame. The theoretical flame lengths using the various models were:

<u>Chemistry Model</u>	<u>$L_f(1-g)$ (cm)</u>	<u>$L_f(0-g)$ (cm)</u>
Complete combustion	.60	.83
CO and H_2	-	.44
H_2O and C(s)	.26	.35

Thus, while for a given chemical model the ratio of the normal gravity to zero gravity theoretical flame lengths is roughly $4/3$, the ratio can be as low as .58 if one assumes "total pyrolysis" in the zero gravity flame, and full complete combustion for the normal gravity flame. The centerline and radial

temperature profiles shown in Figures 22 and 23, and the isotherm map on Figure 24 show clearly that even using the low level energy release CO-H₂ partial oxidation model the temperature levels are sufficiently high to promote the formation of soot in the fuel rich regions. This conclusion is substantiated by the data of Reference 14, which shows that soot can form at temperatures of the order of 1000°K depending upon the residence time and equivalence ratio.

Although general qualitative agreement is obtained in terms of predicting the increase of flame length and width as the gravity level is reduced, it appears that the accuracy of the predictions for the 0-g flame is dependent upon the kinetics of the combustion process.

b. Elliptic Effects

Although the studies presented so far have indicated a number of mechanisms which need additional consideration, their importance has been discussed within the context of a parabolic system of conservation equations. The question arises as to the potential importance of elliptic effects in terms of the data that has been analyzed in this study. The significant deviations between theory and experiment occur for the lowest Reynolds number cases. This has already been partly resolved in terms of reduced temperature levels associated with kinetics effects and radiation. Nevertheless, axial diffusion effects must also play a role in the flame structure at sufficiently low Reynolds numbers. For example, boundary layer theory is known to apply when the lateral domain of influence is "small" compared with the axial extent of interest. Specifically, for laminar flow the relationship between the lateral dimensions, δ , and some characteristic axial length is:

$$\frac{\delta}{L} \sim \frac{1}{\sqrt{Re_L}} \quad (46)$$

where, $Re_L = \frac{\rho_m u_m L}{\mu_m}$ (47)

This choice for Reynolds number is based upon the Dimensional Analysis, Section 6, and δ_m , μ_m and u_m are the density, viscosity, and velocity, respectively, evaluated at the maximum flame width point.

The "condition" for boundary layer theory to apply is:

$$\frac{\delta}{L} \ll 1 \quad (48)$$

Although the condition required by Eq. (48) is somewhat ambiguous it is sufficient to define boundaries of applicability based upon a reasonable requirement for accuracy of the solution. What is needed then is a condition that satisfies the requirement that lateral diffusion dominates over axial diffusion. For this purpose it is sufficient to require,

$$\frac{\delta}{L} \leq .1 \quad (49)$$

for the solution to be "very good." This condition, via Eq. (46) implies that the "running" Reynolds number, Re_L , be such that:

$$Re_L \geq 100 \quad (50)$$

Now, since no distinct boundary of applicability can be defined a broader definition for the adequacy of the boundary layer theory is appropriate. This has been selected according to the following criteria:

$$\begin{aligned} Re_L &\geq 100 \text{ very good} \\ 25 &\leq Re_L \leq 100 \text{ adequate} \\ Re_L &\leq 25 \text{ poor} \end{aligned} \quad (51)$$

Now, relating Re_L to Re_m yields the desired limits, viz:

$$Re_L = Re_m \frac{L}{r_m} \quad (52)$$

where L is the flame length.

Figure 25 shows a composite of experimental and theoretical results including the boundaries defined by Eq. (51). The agreement for normal-g (open symbols) is very good until the "poor" domain is encroached. Even there, as already observed, the results are actually good, indicating that for normal gravity the effect of buoyancy tends to make the basic boundary layer criteria conservative. The zero-g comparison is worse as previously cited, but the trend is consistent with the boundaries defined by Eq. (51). Moreover, the prior analysis of the effect of reduced temperature levels including the effects of kinetics would result in a leftward shift of the theoretical 0-g curve. Thus, better agreement can be anticipated with boundary layer theory except at the lowest Re_m 's i.e. - $Re_m \sim 5$, when appropriate kinetics effects and radiation losses are taken into account.

c. Transient Effects

Thus far in this discussion emphasis has been based upon the importance of kinetics in terms of its relationship to the relatively large residence times associated with low Reynolds number flows particularly under 0-g conditions. There is yet another consideration associated with the residence times encountered under zero-g conditions and this is related to transient effects associated with drop tower experiments. If the non-steady term had been included in our conservation equations (Section 3) a parameter characterizing the relative importance of transient effects would have appeared. The particular parameter is the Strouhal number which relates the residence time to the time, τ_c , associated with the event which in this case is the drop sequence, viz.:

$$\text{Strouhal Number} = \frac{r_m}{u_m \tau_c} \quad (53)$$

Now, referring to Figure 26 it is seen that the characteristic residence times, $\tau_m = r_m / u_m$ are substantially larger for the 0-g cases than for the corresponding normal-g conditions. It is further noted that for $\tau_m \sim 100$ msec, sustained combustion under 0-g conditions is not observed. The data of References 1 and 2 show that when quenching occurs it is generally preceded by the attainment of a minimum flame length in times on the order of 50 to 100 milliseconds. This is an unambiguous characteristic time, τ_c , associated with the sudden change in gravity level. The Strouhal number, is, therefore, on the order of unity or greater.

Thus, the hot products of normal-g combustion are retained within these 0-g flames because of the extreme reduction in convective transport associated with the low Reynolds number cases. The retention of the hot combustion gases shields the flame zone from fresh oxygen while promoting pyrolysis of the fresh fuel being steadily injected directly into the flame zone. Thus, before the flame can adjust to a steady state configuration with convective transport matching diffusive transport, a critical reduction in temperature occurs. This affects the kinetics of the oxidation process and there results a reduced heat release rate until sustained combustion may no longer be possible and the flame "quenches." This is indeed what is shown by Figure 26.

It appears then that in addition to the various partial oxidation processes described above that for low Reynolds numbers, transient effects must also be considered.

The results of the study thus far have shown that while there are mechanisms that need additional attention, the basic behavior is predicted for the steady state flames including the 0-g configurations. Thus, a dimensional analysis has been performed and is discussed in the next section.

6. DIMENSIONAL ANALYSIS

A dimensional analysis can serve to (1) define the controlling parameters necessary for scaling purposes, (2) aid in organizing experimental results and (3) indicate the relative importance of the mechanisms controlling the process. As cited in Section 2, however, the most meaningful set of values of the flow properties which enter into the dimensionless groups are not necessarily the basic initial and boundary conditions. In fact, order of magnitude variations in the transport properties and flow variables are common in these diffusion flames. Thus, the approach here involves (a) finding a local state within the flow that best characterizes the flame and (b) relating those state properties to the given boundary conditions. The result is a set of relations which permit the evaluation of the various parameters including Reynolds number and Grashof number given the boundary conditions.

Upon a review of the various direct calculations it became apparent that the flow field structure is most dependent upon the properties associated with the heated zones within the flow. This suggested that the flame front properties should be used including a consistent velocity and dimension. The maximum flame width point was selected since the maximum flame width radius, r_m , is not only unambiguous but gives a true characteristic measure of the flame size.

To verify this hypothesis a systematic study was performed to determine the implications of this model. Figure 26 shows a result of correlating the maximum flame width velocity, u_m , with the associated flame width, r_m . This theoretical result includes normal-g and 0-g configurations and the results indicate that there is a good "universal" correlation. The significance of this result is twofold: (1) it provides one relationship between maximum flame width properties and the boundary conditions and (2) it is consistent with our earlier representation of the data. The first point is discussed in detail later in connection with relating the dimensionless groups to the boundary conditions. The second point is crucial in terms of the relationship between flame length and the volumetric flow. Examination of Eq. (4), Section 3, shows that:

$$L_f \sim Q^* (\sim u^* r^{*2}) \quad (54)$$

Now, letting the starred quantities be the fuel jet values gives:

$$L_f \sim Q(\sim u_o r_o^2) \quad (55)$$

where Q is the volumetric flow rate of fuel. This is precisely what is predicted and what is observed experimentally (c.f. Figures 5 and 6). Now from Figure 27 it is seen that:

$$u_m r_m^2 \equiv u_o r_o^2 \quad (56)$$

Thus,

$$L_f \sim u_m r_m^2 \quad (57)$$

which is what Eq. (4) Section 3, indicates when the starred quantities are replaced by the maximum flame width properties. It should be noted that "equations" (55) and (57) may also be written:

$$\frac{L_f}{r_o} \sim Re_o \quad (58)$$

and

$$\frac{L_f}{r_m} \sim Re_m \quad (59)$$

respectively. Thus, introducing the maximum flame width properties is thus far totally consistent with the existing observations.

At this point the study was devoted to evaluating the adequacy of the resulting dimensionless groups in characterizing the overall flame behavior in terms of the effect of buoyancy. It was found that such a meaningful representation of the behavior of the methane-air flames in terms of the maximum flame width dimensionless groups (Gr/Re^2 and $1/Re$) in explaining the relative importance of the buoyancy, viscous and inertia forces in the flame did indeed result. For example, Figure 28 shows the theoretical predictions for the relative importance of buoyancy, over the range of conditions of the associated experimental studies in References 1 and 2. These results are consistent with those experiments as shown back in Figure 7. Namely, the effect of buoyancy is relatively important over the entire range covered by the experiments. A composite of the theoretical results is shown in Figure 29 showing that at constant Reynolds number the effect of inertia increases relative to buoyancy as the initial fuel jet radius (and Q) is increased. Conversely, at the lower Reynolds number, large r_0 , conditions, the effect of buoyancy is most dominant and these flames are subject to the more drastic change upon going from normal-g to zero-g conditions. Thus, the effects of transient adjustments and kinetics are expected to be most important in this regime. Since these effects are intimately connected to the residence time an attempt was made to relate the relative theoretical effect of buoyancy under normal-g to the observed quenching process. The result is shown in Figure 30. The correspondence between the increase in residence time with the buoyancy effect is shown and a cutoff for stable 0-g flames is indeed obtained. This result is consistent with the results previously shown in Figure 26 and, in fact, the correlation shown in Figure 30 will carry over when presented as a function of the effective 0-g residence time, τ_m , which in terms of the actual magnitude of those times lends further credence to the relevance of the use of maximum flame width properties.

To complete the development of these "effective" characteristic parameters the final step relating the maximum flame width state to the fuel jet conditions was carried out.

For a specific fuel/oxidizer/diluent combination, the stoichiometric flame temperature, density, viscosity, etc., are either known or readily calculated. However, the maximum flame radius, (r_m) and its associated velocity (u_m) are generally not known prior to performing a detailed experiment or performing a reliable calculation.

Hence, one must relate r_m and u_m to the specified boundary conditions which requires two relations. This has been done for the methane-air system with the aid of the numerical predictions that have been made during the course of this study in comparison with the experimental data (Private communication from Mr. Thomas H. Cochram, June 23, 1971).

Regarding the existing data, the essential experimental data given is the flame lengths and maximum widths and whether or not a steady-state zero gravity flame existed. Now, the work presented thus far indicates the importance of chemical kinetics, particularly for the zero-gravity flames. Hence, we were led to correlate the fuel conditions by means of a "fuel time", τ_o , defined as the burner nozzle radius divided by the bulk fuel burner exit velocity. As shown in Figure 31, a correlation for $r_m = r_m(\tau_o, r_o)$ was indeed found. Both theoretical and experimental results are shown in Figure 31 and it should be noted that the theoretical predictions are within the scatter of the experimental data. To complete the definition a second relation was required relating r_m and u_m to the boundary conditions which has already been described in connection with Figure 27.

Now, in Figure 31 it is shown that for normal gravity flames ($\bar{g} = 1$) it is possible to relate both theoretical and experimental values of r_m/r_o (within the scatter of the results) to τ_o . However, this relation is not unique with respect to gravity level. As shown in Figure 32 the relation between the average of the theoretical predictions of r_m/r_o and τ_o shows a systematic influence due to gravity for non-zero gravity levels, and then is abruptly different for zero gravity flows. This is indicative of the persistence of the importance of the buoyancy effect even for gravity levels as low as 0.1-g for the laminar methane-air diffusion flames.

The relation between r_m/r_o and τ_o is of the form $r_m/r_o = a - m \log_{10} \tau_o$. Figure 33 shows for non-zero gravity, m is essentially constant, and a may be expressed as $a = 10.5e^{-.603\bar{g}}$. Then, $r_m/r_o = (10.5 e^{-.603\bar{g}}) - 3.7 \log_{10} \tau_o$. It is interesting to note that the experimental data for methane falls on the extension of the straight line shown in Figure 31. The expression for r_m/r_o for values of \bar{g} intermediate between 0 and 0.1

can be further defined by more computations. However, here, as in any dimensional analysis, we are concerned with order of magnitude results in the computation of the dimensionless groups, while the variation in r_m/r_o would be less than a factor of 2 even for very low gravity levels. In summary, it appears that the maximum flame width properties best characterize the steady state flames that have been investigated here. In addition, relating the results in terms of these parameters has aided in pinpointing the relevance of buoyancy and residence time upon the observed flame quenching process.

Now, to provide additional insight into the effects of both gravity level and the environmental oxygen concentration a parametric study was performed. This study utilized Fickian diffusion and "complete" combustion. The results of this study are discussed in the next section.

7. PARAMETRIC STUDY

A parametric study can serve several purposes: (1) Provide direct predictions on flame structure as affected by gravity level and environmental oxygen concentration, (2) demonstrate the detail available for comparison with in-depth flame measurements and (3) indicate the utility of the model to guide the design of experiments tailored to provide additional detailed data for verification of more refined theoretical models.

Numerical solutions for the parametric study of the two cases were made, and are presented in this section.

The initial conditions for the parametric study were:

Fuel	r_o (cm)	T_o ($^{\circ}$ K)	Q (cc/sec)	T_e ($^{\circ}$ K)	P_e (atm)
Methane	.051	294	5.15	294	1
Propylene	.051	294	.24	294	1
Fuel	\bar{g}	Environment Oxygen Level			Re_o
Methane	0, $\frac{1}{2}$, 1	air, 50%, 100%			195
Propylene	0, $\frac{1}{2}$, 1	air, 50%, 100%			34.5

In Figures 34 through 43 the theoretical flames shapes shown are obtained in the computations made for the above initial conditions. Several observations may be made from these results:

For the methane flames, when experimental data were available (1-g and 0-g methane/air) there was very good agreement between the data and the theoretical flame length and width predictions. The initial fuel Reynolds number, Re_o , was 195. As shown in Figures 37 and 38, the effective flame Reynolds number, Re_m , based upon local conditions is over an order of magnitude less than Re_o . This behavior is similar to that observed by Wohl, et al. (Reference 4) in their much higher speed butane-air flames; namely, that an initially turbulent, or transitional, fuel jet actually developed smoothly into a laminar flame. For the methane-air flames, the effective flame Reynolds number is still high enough so that a relatively long, thin flame develops, even in the absence of buoyancy, as shown for the zero-gravity flames of Figure 38. However, for the propylene flames (Figures 39 through 43) where the fuel Reynolds number is almost an order of magnitude less ($Re_o = 34.5$), the resulting flame Reynolds numbers are of the order of unity, or less, and the flames are very squat.

A summary of the theoretical shape factors obtained for the methane and propylene flames is shown in Figure 44. The relatively stronger influence of oxidizer composition versus gravity level upon the shape factor is evident, as is the squatness of all of the propylene flames.

A summary of the influence of fuel and environment composition, and gravity level, upon the buoyancy force is shown in Figure 45, expressed in terms of a crossplot of the representative flame Grashof number versus the initial fuel Grashof number. It may be seen that once the flame survives the tendency toward recirculation, typified by a negative fuel Grashof number, the most important influence on the strength of the buoyant force (and hence the length of the flame) is the nature of the environment. Hotter burning oxygen flames have higher viscosity levels, and hence mix more rapidly yielding shorter flames.

The influence of the environmental composition is further illustrated in Figures 46 through 63, showing the axial histories, from the nozzle exit to the stoichiometric flame closure, of the centerline temperatures, velocities, and viscosities of the theoretical flames. The very high temperature levels reached for the pure oxygen and 50% oxygen-50% nitrogen environments are partly the result of chemical dissociation effects (i.e., the formation of OH, H, O, etc.) not being included in the "complete combustion" chemistry model. Plots of the centerline viscosity were included to underline the dependence of the local, laminar mixing process upon the local temperature level and the related combustion process.

For both the methane and propylene evaluation cases, a representative set of conditions was chosen ($\bar{g} = \frac{1}{2}$ and a 50% oxygen environment), and radial profiles of temperature, velocity, stoichiometric (equivalence) ratio, Reynolds number, Grashof number, and viscosity were plotted and are presented in Figures 64 through 74. In addition maps of constant mass flow (streamlines) and constant temperature (isotherms) were constructed from the appropriate radial profiles and are shown in Figures 75 through 77.

The radial temperature profiles in Figures 64 and 65, and the associated isotherm maps in Figures 76 and 77, clearly illustrate that for the 50% oxygen environment the lack of a dissociation mechanism in the "complete combustion" chemistry model results in calculated flame temperatures that are of the order of 1000°K higher than those that would occur for an equilibrium chemistry model accounting for dissociation effects.

This excessively high temperature - low density portion of the flow field, of course, contributes to the excessive squatness of the propylene flame. The effect of using "partial oxidation" chemistry models to lower the flame temperature level would result in an improved representation of the flame chemistry, and in the computation of a narrower, more realistic theoretical flow field. However, even then the globularity of the low speed propylene flame will result in a relatively large surface area, thus contributing to potential radiant heat transfer losses.

In Figure 75, the shapes of typical constant mass flow streamlines are plotted. Both the volumetric expansion of the streamlines that were initially in the fuel jet as well as the entrainment and acceleration of environmental gas may be observed. Figures 76 and 77 indicate that high temperatures will persist on the axis for a significant distance downstream of the stoichiometric flame edge closure.

8. SUMMARY OF RESULTS

This report represents a theoretical study of the effects of gravity and environmental composition upon the structure of laminar, hydrocarbon diffusion flames. The model has been used to predict experimental observations and to perform parametric studies which have produced the following observations:

1. For complete combustion the model predicts increasing flame length and width with decreasing gravity level and decreasing environmental oxygen concentration. The predicted effect of g-level is observed in the bulk of the experimental data whereas the effect of oxygen concentration needs verification. However, including partial oxidation and reduced temperature levels in the model yields predictions which show that a reversal in the trend with g-level can occur and may be an explanation for some isolated observations made on the heavier hydrocarbon.

2. The accuracy of the predictions is generally excellent for normal-g flames while for the corresponding steady state zero-g flames the predictions at the lower Reynolds numbers showed generally wider flames than were observed.

In arriving at these overall findings the importance of certain mechanisms controlling the detailed structure of diffusion flames have been delineated:

3. Variable transport properties including non-unity Schmidt and Prandtl numbers must be taken into account.
4. A dimensional analysis shows that the state of the flow at the maximum flame width point characterizes the flame behavior. Furthermore, this local state can be related to the boundary conditions.
5. The dimensionless groups that characterize low speed diffusion flames are the Grashof number, Gr, Reynolds number, Re, Prandtl number, Pr and Schmidt number, Sc. It is further noted that combining Gr and Re to form the Froude number, $(Fr \propto (Gr/Re^2)^{-1})$ does not eliminate Re as an independent controlling parameter.
6. Fickian diffusion is shown to be adequate although preliminary application of an extended model including multi-component diffusion provides some improvement in the agreement between predictions and experimental data.

7. Shifting equilibrium in the limit of complete combustion is an adequate model for the bulk of the normal-g flames but it is shown that partial oxidation models provide an improvement in the accuracy of the predictions under zero gravity conditions. This study suggests that partial combustion associated with the oxidation kinetics is important. Pyrolysis and soot formation are also shown to be of potential relevance in terms of their effect upon the local molecular weight (buoyant force) and radiation.
8. Incipient recirculation is predicted for heavy hydrocarbons when sufficiently large negative buoyancy arises. Unfortunately, the available data are not sufficiently detailed to verify that this occurs. However, the effect of pyrolysis cited above would tend to reduce the magnitude of the negative buoyancy and minimize the occurrence of recirculation.
9. Axial diffusion of mass, energy and momentum (elliptic effects) becomes important at very low Re , zero-g conditions. This is evident from the observation of globular flames, particularly as quenching is approached.

In general, the model presented here has provided a tool for accurate predictions of diffusion flame structure over wide ranges of conditions including gravity level and environmental composition. Furthermore, an improved understanding of the basic mechanisms has been gained and regimes of operating conditions requiring the inclusion of additional effects have been delineated.

9. APPENDICES

APPENDIX A - FINITE DIFFERENCE SOLUTION OF THE CONSERVATION EQUATIONS

Summary

The governing flow field conservation equations are transformed, into the von Mises plane, and then solved numerically employing an explicit finite difference technique.

Calculation Procedure

The solution of the system of conservation equations presented in Section 2 provides the details of the flow field including the velocity, temperature, and species fields. Gross characteristics including combustion lengths and flow deflections are also obtained.

The global continuity equation can be eliminated from the system of differential equations by introducing the von Mises coordinates as the independent variables. The transformation, $x, r, \rightarrow x, \Psi$, is defined according to the relations:

$$\rho u r^N = \Psi^N \Psi_r \quad (A-1a)$$

$$- \rho v r^N = \Psi^N \Psi_x \quad (A-1b)$$

where

$$N = \begin{cases} 0 & \text{- plane two-dimensional flow} \\ 1 & \text{- axisymmetric flow} \end{cases}$$

Introduction of (B-1a) and (B-1b) into the differential equations results in:

Element Conservation

$$\frac{\partial \tilde{\alpha}_i}{\partial x} = \frac{1}{\Psi^N} \frac{\partial}{\partial \Psi} \left[\frac{Le}{Pr} \frac{\mu \rho u}{\Psi^N} r^{2N} \frac{\partial \tilde{\alpha}_i}{\partial \Psi} \right] \quad (A-2)$$

Momentum

$$\frac{\partial u}{\partial x} = \frac{1}{\Psi^N} \frac{\partial}{\partial \Psi} \left[\frac{\mu \rho u}{\Psi^N} r^{2N} \frac{\partial u}{\partial \Psi} \right] + \frac{1}{\rho u} (\rho_e - \rho) g \quad (A-3)$$

Energy

$$\begin{aligned} \frac{\partial H}{\partial x} = \frac{1}{\Psi^N} \frac{\partial}{\partial \Psi} \left[\frac{\mu \rho u}{\Psi^N} r^{2N} \frac{1}{Pr} \left\{ \frac{\partial H}{\partial \Psi} + \right. \right. \\ \left. \left. + \sum_i h_i (Le-1) \frac{\partial \alpha_i}{\partial \Psi} \right\} \right] - g \end{aligned} \quad (A-4)$$

The physical, r , coordinate is obtained by the inverse transformation:

$$r^{N+1} = (N+1) \int_0^{\Psi} \frac{\Psi^N}{\rho u} d\Psi \quad (A-5)$$

and the transverse component of velocity, v , is given by:

$$v = - \frac{\Psi^N \Psi_x}{\rho r^N} \quad (A-6)$$

Boundary Conditions

The governing equations are parabolic and require initial conditions at $x = 0$ and boundary conditions at $\Psi = \infty$ and $\Psi = 0$. The initial and boundary conditions are:

$$\begin{aligned} \text{at } x = 0, \quad 0 \leq \Psi \leq \Psi_j \\ u = u_o, \quad H = H_o, \quad \tilde{\alpha}_j = (\tilde{\alpha}_j)_o \\ x = 0; \quad \Psi \geq \Psi_J \quad \tilde{\alpha}_j = (\tilde{\alpha}_j)_e \\ u = u_e(0), \quad H = H_e \end{aligned} \quad (A-7)$$

at $x \geq 0$; $\Psi \rightarrow \infty$; $\tilde{\alpha}_j = (\tilde{\alpha}_j)_e$

$$u = u_e(x), \quad H = H_e$$

where

$$\frac{dp_e}{dx} - \rho_e g = 0 \quad (A-8)$$

and

$$H_e = \text{constant} \quad (A-9)$$

The conditions expressed by Eqs. (B-7), (B-8) and (B-9) with symmetry at $\Psi = 0$ completes the specification of the boundary conditions.

The solution of the governing system has been obtained employing an explicit finite difference technique (B-1).^{*} Figure (B-1) shows a generic point, $(n+1, M)$ in the x - Ψ grid network. The finite difference formulation for the calculation of the flow at the point $(n+1, M)$ is obtained by using the following explicit difference relations where P is any one of the three pertinent variables, u , $\tilde{\alpha}$, or H :

$$\frac{\partial P}{\partial x} = \frac{P_{n+1, M} - P_{n, M}}{\Delta x} \quad (A-10)$$

$$\frac{\partial P}{\partial \Psi} = \frac{1}{2} \frac{P_{n, M+1} - P_{n, M-1}}{\Delta \Psi} \quad (A-11)$$

$$\frac{\partial}{\partial \Psi} \left[b \frac{\partial P}{\partial \Psi} \right] = \frac{b_{n, M+1/2} [P_{n, M+1} - P_{n, M}] - b_{n, M-1/2} [P_{n, M} - P_{n, M-1}]}{\Delta \Psi^2} \quad (A-12)$$

where

$$b = \frac{\rho_e u}{\Psi} \quad (A-13)$$

^{*}(B-1): Zeiberg, S., and Bleich, G., "Finite Difference Calculations of Wakes," AIAA Preprint 63-449. Also GASL TR-338, February 1963.

$$b_{n, M+\frac{1}{2}} = \frac{1}{2} \left[b_{n, M} + b_{n, M+1} \right] \quad (A-14)$$

and

$$\Psi = M(\Delta\Psi) \quad (A-15)$$

The conservation equations in difference form are:

Elements

$M = 0$:

$$\begin{aligned} (\tilde{\alpha}_j)_{n+1,0} = (\tilde{\alpha}_j)_{n,0} + \frac{2(1-N)\Delta x}{(\Delta\Psi)^2} \left[\frac{(\rho u)^{1-N} \text{Le } \mu}{\text{Pr}} \right]_{n,0} \\ \left[(\tilde{\alpha}_j)_{n,1} - (\tilde{\alpha}_j)_{n,0} \right] \end{aligned} \quad (A-16a)$$

$M \neq 0$:

$$\begin{aligned} (\tilde{\alpha}_j)_{n+1} = (\tilde{\alpha}_j)_{n,M} + \frac{\Delta x}{M^N (\Delta\Psi)^{2+N}} \left\{ \left(\frac{\text{Le } b}{\text{Pr}} \right)_{n, M+\frac{1}{2}} (\tilde{\alpha}_j)_{n, M+1} - \right. \\ \left. - \left[\left(\frac{\text{Le } b}{\text{Pr}} \right)_{n, M+\frac{1}{2}} + \left(\frac{\text{Le } b}{\text{Pr}} \right)_{n, M-\frac{1}{2}} \right] (\tilde{\alpha}_j)_{n, M} + \right. \\ \left. + \left(\frac{\text{Le } b}{\text{Pr}} \right)_{n, M-\frac{1}{2}} (\tilde{\alpha}_j)_{n, M-1} \right\} \end{aligned} \quad (A-16b)$$

Momentum:

$M=0$

$$U_{n+1,0} = U_{n,0} + \frac{2(1+N)\Delta x}{(\Delta\Psi)^2} \left[(\rho u)^{1-N} \mu \right]_{n,0} [U_{n,1} - U_{n,0}] + (\rho_e - \rho_o) g \frac{\Delta x}{(\rho u)_{n,0}} \quad (A-17a)$$

$M \neq 0$

$$\begin{aligned}
 U_{n+1,M} = & U_{n,M} + \frac{\Delta x}{M^N (\Delta \Psi)^{2+N}} \left\{ (b)_{n,M+\frac{1}{2}} U_{n,M+1} - \right. \\
 & \left. - [b_{n,M+\frac{1}{2}} + b_{n,M-\frac{1}{2}}] U_{n,M} + b_{n,M-\frac{1}{2}} U_{n,M-1} \right\} - \\
 & + (\rho_e - \rho) g \frac{\Delta x}{(\rho u)_{n,m}} \quad (A-17b)
 \end{aligned}$$

Energy

$M=0$:

$$\begin{aligned}
 H_{n+1,0} = & H_{n,0} + \frac{2(1+N)\Delta x}{(\Delta \Psi)^2} [(\rho u)^{1-N} \mu]_{n,0} \left\{ \left(\frac{1}{Pr} \right)_{n,0} [H_{n,1} - H_{n,0}] + \right. \\
 & \left. + \sum_i (h_i \frac{Le-1}{Pr})_{n,0} [(\alpha_i)_{n,1} - (\alpha_i)_{n,0}] \right\} \quad (A-18a)
 \end{aligned}$$

$M \neq 0$:

$$\begin{aligned}
 H_{n+1,M} = & H_{n,M} + \frac{\Delta x}{M^N (\Delta \Psi)^{2+N}} \left\{ \left(\frac{b}{Pr} \right)_{n,M+\frac{1}{2}} H_{n,M+1} - \left[\left(\frac{b}{Pr} \right)_{n,M+\frac{1}{2}} + \right. \right. \\
 & \left. \left. + \left(\frac{b}{Pr} \right)_{n,M-\frac{1}{2}} \right] H_{n,M} + \left(\frac{b}{Pr} \right)_{n,M-\frac{1}{2}} H_{n,M-1} \right. \\
 & \left. + \sum_i \left[b h_i \left(\frac{Le-1}{Pr} \right) \right]_{n,M+\frac{1}{2}} (\alpha_i)_{n,M+1} - \right. \\
 & \left. - \sum_i \left[\left(b h_i \frac{Le-1}{Pr} \right)_{n,M+\frac{1}{2}} + \left(b h_i \frac{Le-1}{Pr} \right)_{n,M-\frac{1}{2}} \right] (\alpha_i)_{n,M} + \right. \\
 & \left. + \sum_i \left[b h_i \frac{Le-1}{Pr} \right]_{n,M-\frac{1}{2}} (\alpha_i)_{n,M-1} \right\} \quad (A-17b)
 \end{aligned}$$

Step Size Control

The step size in the explicit finite difference scheme is controlled by a stability criterion and from studies of linear parabolic partial differential equations there results the following condition, Reference (B-2):

$$\frac{\Delta \Psi^2}{(1+N)6} \left[\frac{Pr}{Le \mu (\rho u)^{1-N}} \right]_{n,o} \geq \Delta x \leq \frac{1}{3} \frac{M^N (\Delta \Psi)^{2+N}}{\left(\frac{Le_b}{Pr} \right)_{n,M+\frac{1}{2}} + \left(\frac{Le_b}{Pr} \right)_{n,M-\frac{1}{2}}} \quad (A-19)$$

Although the partial differential equations are non-linear, the present explicit difference formulation results in a locally linear system and Eq. (B-19) provides an estimate of the stable step size. The computer program has as an input an arbitrary fraction which can be chosen to cut the above step size in the event a stability problem arises.

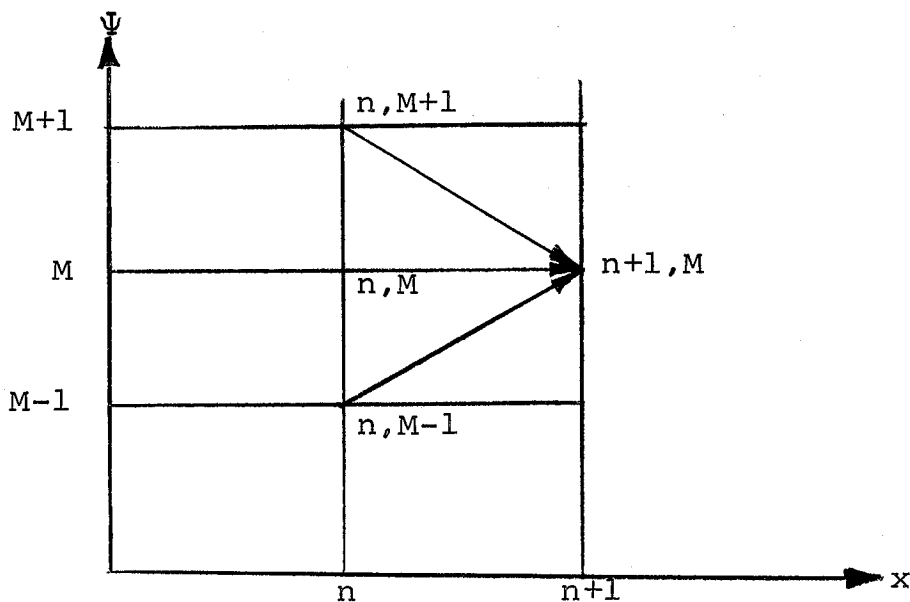


Figure A-1. - Schematic of the Grid Network Used in the Explicit Finite Difference Technique. The Arrows Indicate the Calculation of the Flow Field Point $n+1, M$ from Data at Station n .

(B-2) Richtmyer, R. D., Difference Methods for Initial-Value Problems, Interscience Publishers, New York, 1957.

The finite difference form for the multicomponent diffusion analysis, presented in Section 2, is formulated in a similar manner, with the significant addition that the diffusional mass fluxes, J_i , in Eq. (19) must be determined by the following matrix techniques:

$$\begin{bmatrix} E_{1,1} & E_{1,2} & \cdots & E_{1,N} \\ E_{2,1} & E_{2,2} & \cdots & E_{2,N} \\ E_{N-1,1} & E_{N-1,2} & \cdots & E_{N-1,N} \\ \rho & \rho & \cdots & \rho \end{bmatrix} \begin{bmatrix} J_1 \\ J_2 \\ J_{N-1} \\ J_N \end{bmatrix} = \begin{bmatrix} F_{1,1} & F_{1,2} & \cdots & F_{1,N} \\ F_{2,1} & F_{2,2} & \cdots & F_{2,N} \\ F_{N-1,1} & F_{N-1,2} & \cdots & F_{N-1,N} \\ 0 & 0 & \cdots & 0 \end{bmatrix} \begin{bmatrix} \frac{\partial \alpha_1}{\partial r} \\ \frac{\partial \alpha_2}{\partial r} \\ \frac{\partial \alpha_{N-1}}{\partial r} \\ \frac{\partial \alpha_N}{\partial r} \end{bmatrix}$$

Since the solution of the conservation equations is by an explicit technique, all of the following parameters which are required to solve for the J_i 's are known:

α_i - mass fraction of species

W_i - molecular weights

ρ - density

$\partial \alpha_i / \partial r$ - the partial derivatives of species in the radial direction

D_{ij} - the diffusion coefficients which form an (NxN) symmetric matrix, i.e.,

$$D_{ij} = D_{ji}$$

The solution vector J comes from

$$[E] \cdot [J] = [\bar{F}] \quad (A-20)$$

The method of solution is by elimination using the largest pivotal divisor. At each stage of forward elimination, an interchange of rows is performed if and when necessary, to insure division by a sufficiently large non-zero element. The forward solution obtains the J_N variable in N forward stages. The backward solution for each of the remaining variables, $J_{N-1}, J_{N-2}, \dots, J_1$ is obtained by successive substitutions.

APPENDIX B - COMBUSTION MODEL

The basic model formulation for the laminar diffusion flame requires an accurate definition of the thermal field rather than the details of the chemical species. Thus, the selection of a chemical system in terms of the number and kinds of species is somewhat arbitrary.

Nonetheless equilibrium as well as kinetic computations require the specification of species. For a system in chemical equilibrium the two principal parameters controlling the accuracy of the assumed set of species are the initial reactant temperature and the fuel/air ratio. Of course, for the determination of the equilibrium state the pressure must also be specified. However, the pressure effect is of secondary importance. Basically then, the temperature and equivalence ratio control the equilibrium state in terms of the degree of dissociation.

In a hydrocarbon-air system the principal products of combustion are H_2O and CO_2 . Furthermore, for fuel lean conditions O_2 will appear while in the fuel rich regime combustibles will be present. However, dissociation of the major species results in the presence of additional species including H , O , OH and CO , in the fuel lean regime, and under fuel rich conditions even more species, including a variety of hydrocarbon fragments, C_xH_y , and soot, $C(s)$ will appear. At temperatures above about $2500^\circ K$ (which is beyond the experimental flame temperature in air environments) the dissociation of nitrogen will start to become significant and species like NO will appear.

As cited above, the principal quantity of interest is the temperature. The objective then was to establish the feasibility of effectively representing the chemical system for the prediction of temperature with less concern for the minute details of the species. It was shown in Section 2 that this indeed could be done for the conditions of interest in the present work ($T \gtrsim 2500^\circ K$). In particular, the entire spectrum of equivalence ratios is modeled by three distinct regimes defined according to the fuel oxygen ratio, Figure B.1.

In the lean regime complete oxidation of the fuel forming CO_2 and H_2O is assumed. The upper limit for this regime is the stoichiometric point where the atom balance is given by:

$$\frac{1}{2} \tilde{\beta}_H + 2\tilde{\beta}_C = \tilde{\beta}_O \quad (\text{B.1})$$

where $\tilde{\beta}$'s are the molar concentrations. In terms of element mass fractions this relationship is given by:

$$\frac{1}{2} \frac{\tilde{\alpha}_H}{W_H} + \frac{2\tilde{\alpha}_C}{W_C} = \frac{\tilde{\alpha}_O}{W_O} \quad (\text{B.2})$$

Accordingly, the lean regime is defined within the limits:

$$\frac{\tilde{\alpha}_O}{W_O} \geq \frac{1}{2} \frac{\tilde{\alpha}_H}{W_H} + \frac{2\tilde{\alpha}_C}{W_C} \geq 0 \quad (\text{B.3})$$

and the specie mass fractions are given by:

$$\alpha_{\text{H}_2\text{O}} = \frac{1}{2} \tilde{\alpha}_H \frac{W_{\text{H}_2\text{O}}}{W_H} \quad (\text{B.4})$$

$$\alpha_{\text{CO}_2} = \tilde{\alpha}_C \frac{W_{\text{CO}_2}}{W_C} \quad (\text{B.5})$$

$$\alpha_{\text{O}_2} = W_{\text{O}_2} \left[\frac{1}{2} \frac{\tilde{\alpha}_O}{W_O} - \frac{1}{4} \frac{\tilde{\alpha}_H}{W_H} - \frac{\tilde{\alpha}_C}{W_C} \right] \quad (\text{B.6})$$

In the fuel rich side it is observed that CO appears in substantial quantities, and depending upon the degree of richness, pure fuel appears.

In zone A of Figure B.1, it is found that the molar concentration of water is essentially constant and that carbon is oxidized to CO_2 and CO . This domain is bounded by the limits:

$$\frac{2\tilde{\alpha}_c}{W_c} + \frac{1}{2} \frac{\tilde{\alpha}_H}{W_H} > \frac{\tilde{\alpha}_O}{W_O} \geq \frac{\tilde{\alpha}_c}{W_c} + \frac{1}{2} \frac{\tilde{\alpha}_H}{W_H} \quad (\text{B.7})$$

wherein the species mass fractions are given by:

$$\alpha_{\text{H}_2\text{O}} = \frac{1}{2} \tilde{\alpha}_H \frac{W_{\text{H}_2\text{O}}}{W_H} \quad (\text{B.8})$$

$$\alpha_{\text{CO}} = W_{\text{CO}} \left[2 \frac{\tilde{\alpha}_c}{W_c} - \frac{\tilde{\alpha}_O}{W_O} + \frac{1}{2} \frac{\tilde{\alpha}_H}{W_H} \right] \quad (\text{B.9})$$

$$\alpha_{\text{CO}_2} = W_{\text{CO}_2} \left[\frac{\tilde{\alpha}_O}{W_O} - \frac{1}{2} \frac{\tilde{\alpha}_H}{W_H} - \frac{\tilde{\alpha}_c}{W_c} \right] \quad (\text{B.10})$$

In zone B pure fuel, C_nH_m , begins to appear and the mole fraction of CO decreases. Hence the bounds are:

$$\infty > \frac{\tilde{\alpha}_c}{W_c} + \frac{1}{2} \frac{\tilde{\alpha}_H}{W_H} > \frac{\tilde{\alpha}_O}{W_O} \quad (\text{B.11})$$

and the species mass fractions are given by:

$$\alpha_{\text{CO}} = W_{\text{CO}} \left[\frac{\tilde{\alpha}_c}{W_c} - n \frac{\tilde{\alpha}_{\text{C}_n\text{H}_m}}{W_{\text{C}_n\text{H}_m}} \right] \quad (\text{B.12})$$

$$\alpha_{\text{C}_n\text{H}_m} = \frac{W_{\text{C}_n\text{H}_m}}{m+2n} \left[\frac{\tilde{\alpha}_H}{W_H} + \frac{2\tilde{\alpha}_c}{W_c} - \frac{2\alpha_O}{W_O} \right] \quad (\text{B.13})$$

$$\alpha_{H_2O} = W_{H_2O} \left[\frac{1}{2} \frac{\alpha_H}{W_H} - \frac{m}{2} \frac{\alpha_{C_n H_m}}{W_{C_n H_m}} \right] \quad (B.14)$$

Also note that since nitrogen is assumed not to react in any one of the three regimes it satisfies the following relationship throughout:

$$\alpha_{N_2} = \tilde{\alpha}_N \quad (B.15)$$

As previously cited this model represents the thermal field quite well for the temperatures of interest ($T \leq 2500^\circ K$).

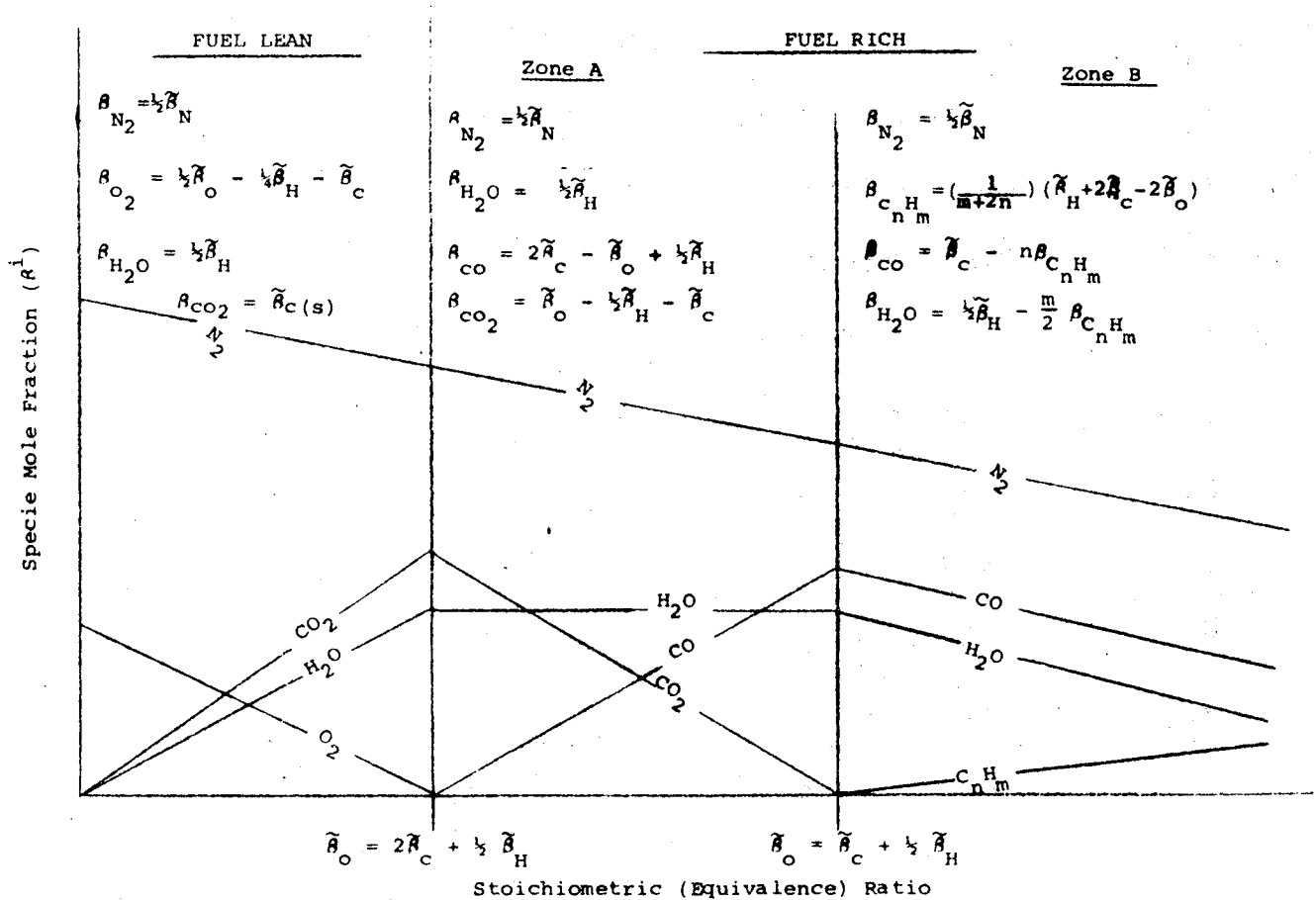


Figure B.1 - Schematic of GASL Full Complete Combustion Chemistry Model

APPENDIX C - LIST OF SYMBOLS

Nomenclature

b	coefficient in the finite difference formulation defined by Eq.
c_p	constant pressure specific heat
D_{ij}	binary diffusion coefficient
Gr	Grashof number
g	acceleration due to gravity
H	mixture stagnation enthalpy
h	mixture static enthalpy
h_i	static enthalpy of the i^{th} species
\tilde{j}	element diffusional mass flux
j	specie diffusional mass flux
k	thermal conductivity
L_f	flame length
N	number of species
P	pressure
Pr	Prandtl number
Q	flow rate
\tilde{R}	universal gas constant
Re	Reynolds number
r	radial coordinate

$r_{1/2}$	half radius
S	flame shape factor
Sc	Schmidt number
T	temperature
u	axial component of velocity
v	radial component of velocity
W	molecular weight
w_i	chemical production of the i^{th} species
w_j	molecular weight of the j^{th} species
w_k	molecular weight of the k^{th} species
x	streamwise coordinate
α	mass fraction
$\tilde{\alpha}$	element mass fraction
μ	viscosity
ρ	density
φ	stream function defined by Eq. (A-1)
Ω	reduced collision integrals
Γ_{kj}	weighted inverse square of the collision cross section
σ_{kj}	collision cross section
ϵ_{kj}	potential energy function

τ_{kj}	reduced temperature
γ_{kj}	molecular weight function
β_{kj}	molecular weight ratio function
η_{kj}	weighted conductivity function
ζ	molecular weight function
λ''_k	partial conductivity function
λ'_k	partial conductivity function
τ_c	characteristic test time
τ_m	characteristic residence time
δ	boundary layer thickness
ϕ	equivalence ratio $\left(\frac{(\text{fuel/air})}{(\text{fuel/air})_{\text{stoichiometric}}} \right)$
σ_k	collision diameter of k^{th} specie
σ_j	collision diameter of j^{th} specie
β_i	mole fraction of the i^{th} specie

Subscripts

e	environment
c	center line
f	flame
i, k	i and k^{th} species
j	j^{th} element
m	maximum flame width

(n,m) generic point in the finite difference grid
o initial fuel conditions
t turbulent
* characteristic value

Superscripts

k kth specie
l lth element

BIBLIOGRAPHY

1. Cochran, T. H. and Masica, W. J., "Effects of Gravity on Laminar Gas Jet Diffusion Flames," NASA TN D-5872, June 1970.
2. Cochran, T. H. and Masica, W. J., "An Investigation of Gravity Effects on Laminar Gas Jet Diffusion Flames," NASA TM X-52757, August 1970.
3. Hottel, H. C. and Hawthorne, W., "Diffusion in Laminar Flame Jets," Third Symposium on Combustion, Flame and Explosion Phenomena, Williams and Wilkins Co., 1949.
4. Wohl, K., Gazley, C. and Kapp, N., "Diffusion Flames," Third Symposium on Combustion, Flame, and Explosion Phenomena, Williams and Wilkins Company, 1949.
5. Burke, S. P. and Schumann, T. E., "Diffusion Flames," Industrial and Engineering Chemistry, v. 20, No. 10, pp. 998-1004, October 1928.
6. Goldburg, A., Cheng Sin-I, "A Review of the Fluid Dynamic Problem Posed by the Laminar Jet Diffusion Flame," Combustion and Flame, v. 9, No. 3, September 1965, pp. 259-272.
7. McMahon, J. F., Kuwata, M., and Essenhigh, R. H., "A Phenomenological Analysis of Unenclosed Laminar Jet Flames," Paper 71-72, Western States Section, The Combustion Institute, Denver 1971.
8. Hirschfelder, J. O., Curtiss, C. F. and Bird, R. B., "Molecular Theory of Gases and Liquids," John Wiley and Sons, Inc., New York, 1954, Ch. 8.
9. Hawthorne, W. R., "The Mixing of Gas and Air in Flames," Doctoral Thesis, MIT, 1939.

10. Edelman, R., "Diffusion Controlled Combustion for Scram-jet Applications," I. Analysis & Results of Calculations, GASL TR-569, 1965. Also presented at the 5th Joint Propulsion Specialists Conference, Colorado, 1965.
11. Chinitz, W. and Baurer, T., "An Analysis of Nonequilibrium Hydrocarbon-Air Combustion," presented at the 1965 Fall Meeting of the Western States Section/The Combustion Institute, October, 1965. Also GASL TR-546.
12. Edelman, R. and Fortune, O., "A Quasi-Global Chemical Kinetic Model for the Finite Rate Combustion of Hydrocarbon Fuels," AIAA Preprint No. 69-86. Also GASL TR-681, January 1969.
13. "Analytical Study of Gravity Effects on Laminar Diffusion Flame Jets," GASL Technical Proposal No. 5-1088, Dec. 1970.
14. Skinner, C. D. and Ruhrwein, R. A., "Journal of Physical Chemistry, Vol. 63, p. 1729 (1959).

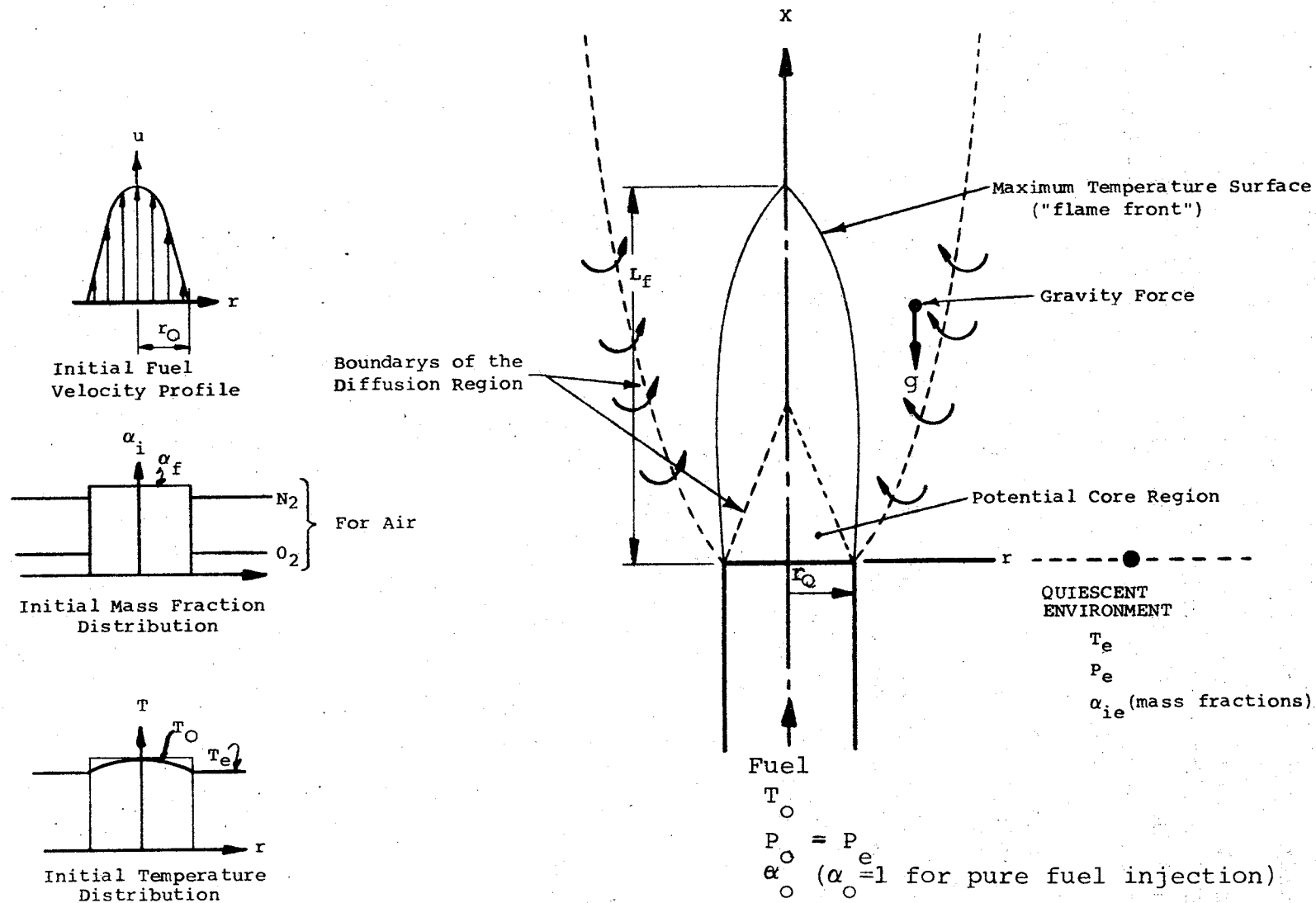


Figure 1. - Schematic of vertical laminar jet.

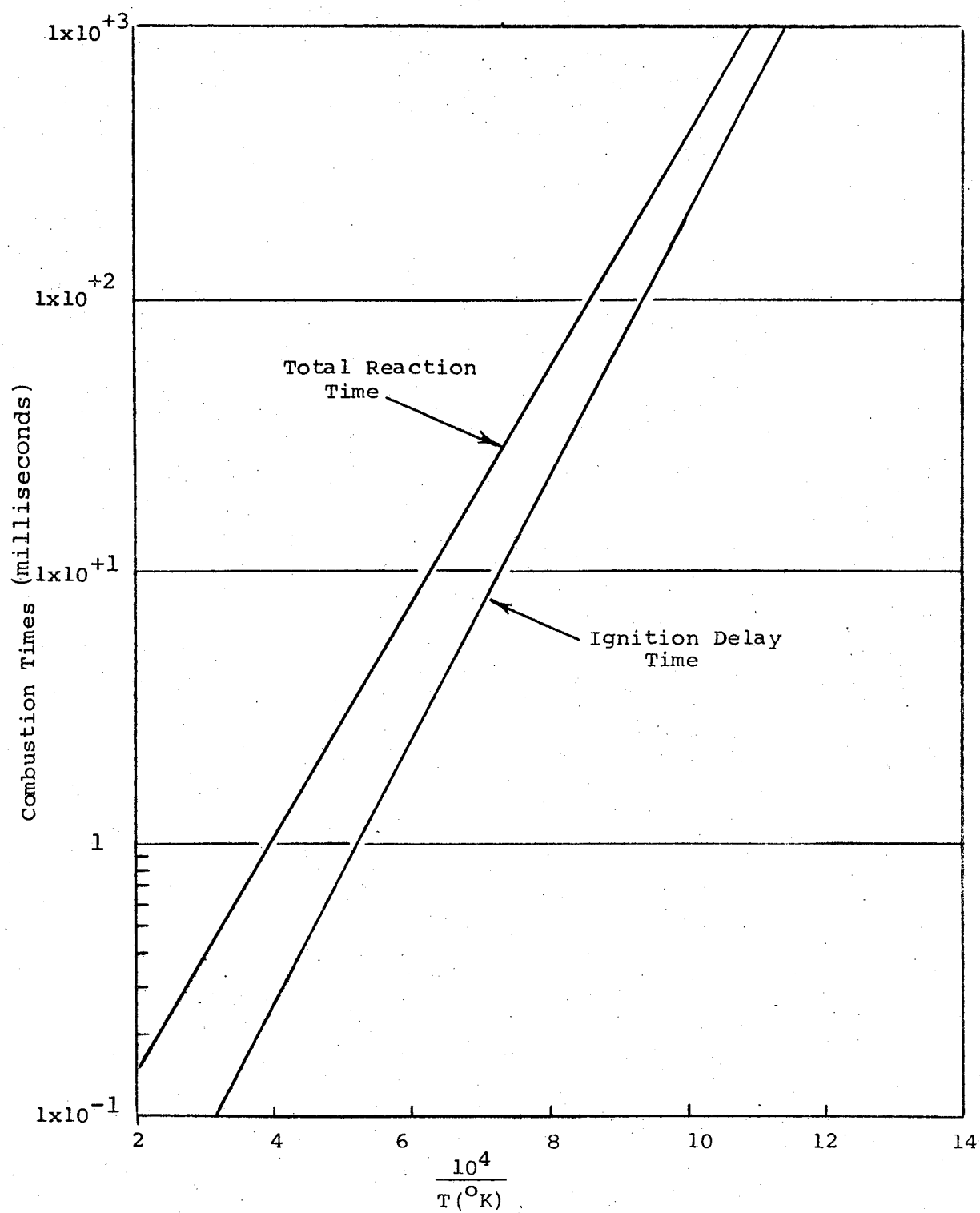


Figure 2. - Chemical combustion times for methane-air mixtures at 1 atm.

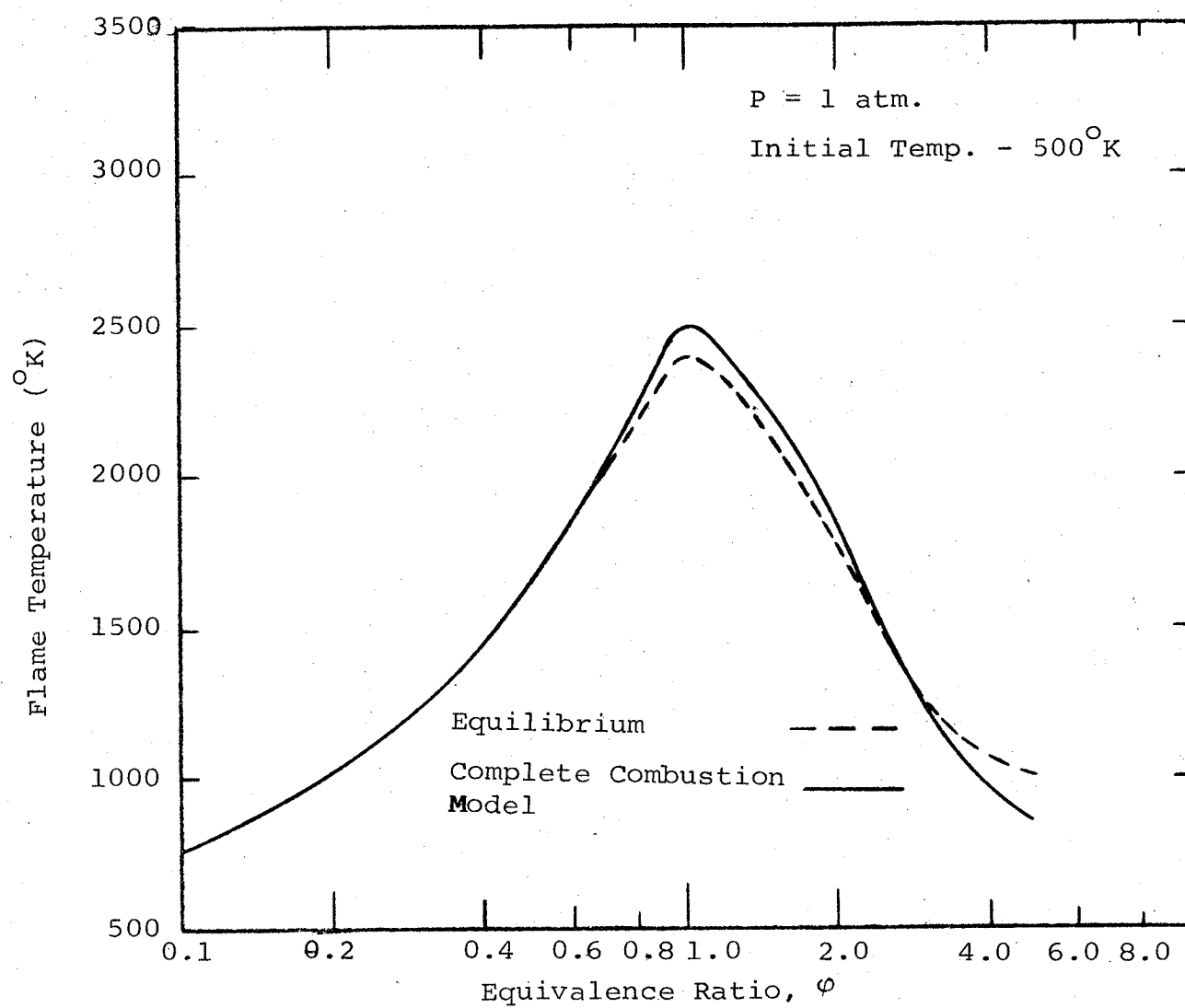


Figure 3. - Comparison of quasi-complete combustion model with equilibrium chemistry for a propane-air system.

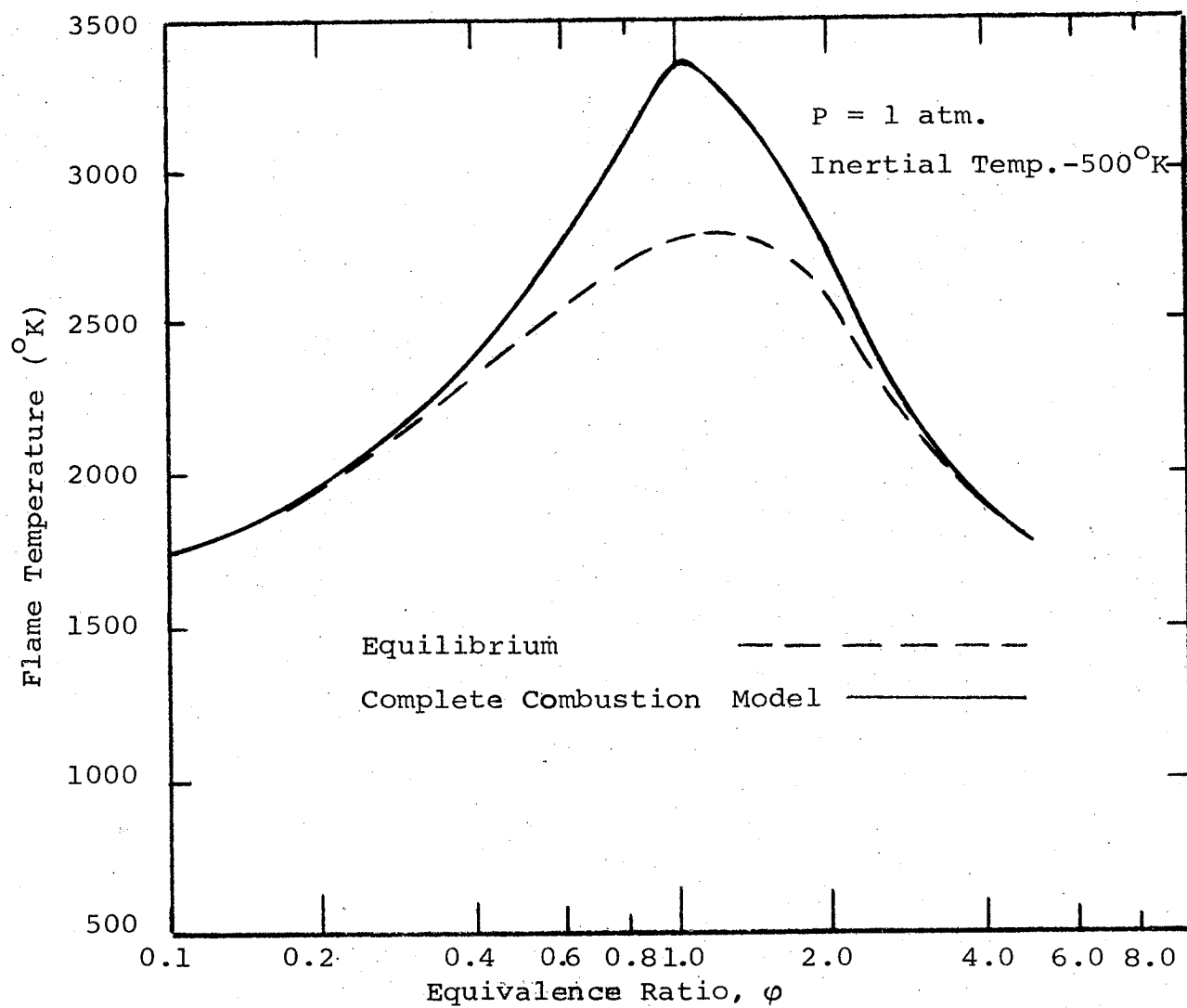


Figure 4. - Comparison of quasi-complete combustion models with equilibrium chemistry for a propane-air system.

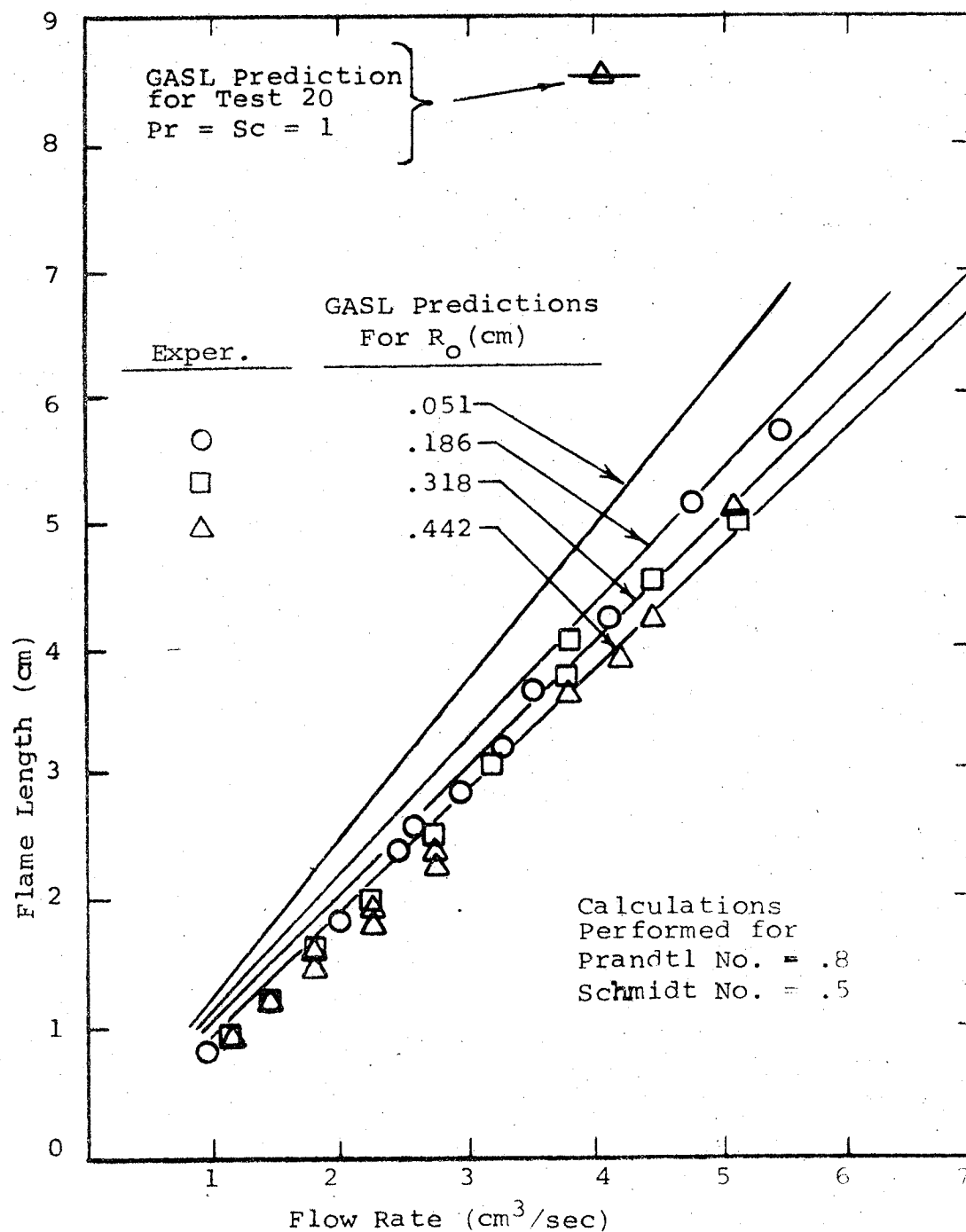


Figure 5. - Comparison of experimental normal gravity flame lengths of Cochran and Masica (Figure 5 - NASA TN D-5872) with GASL prediction.

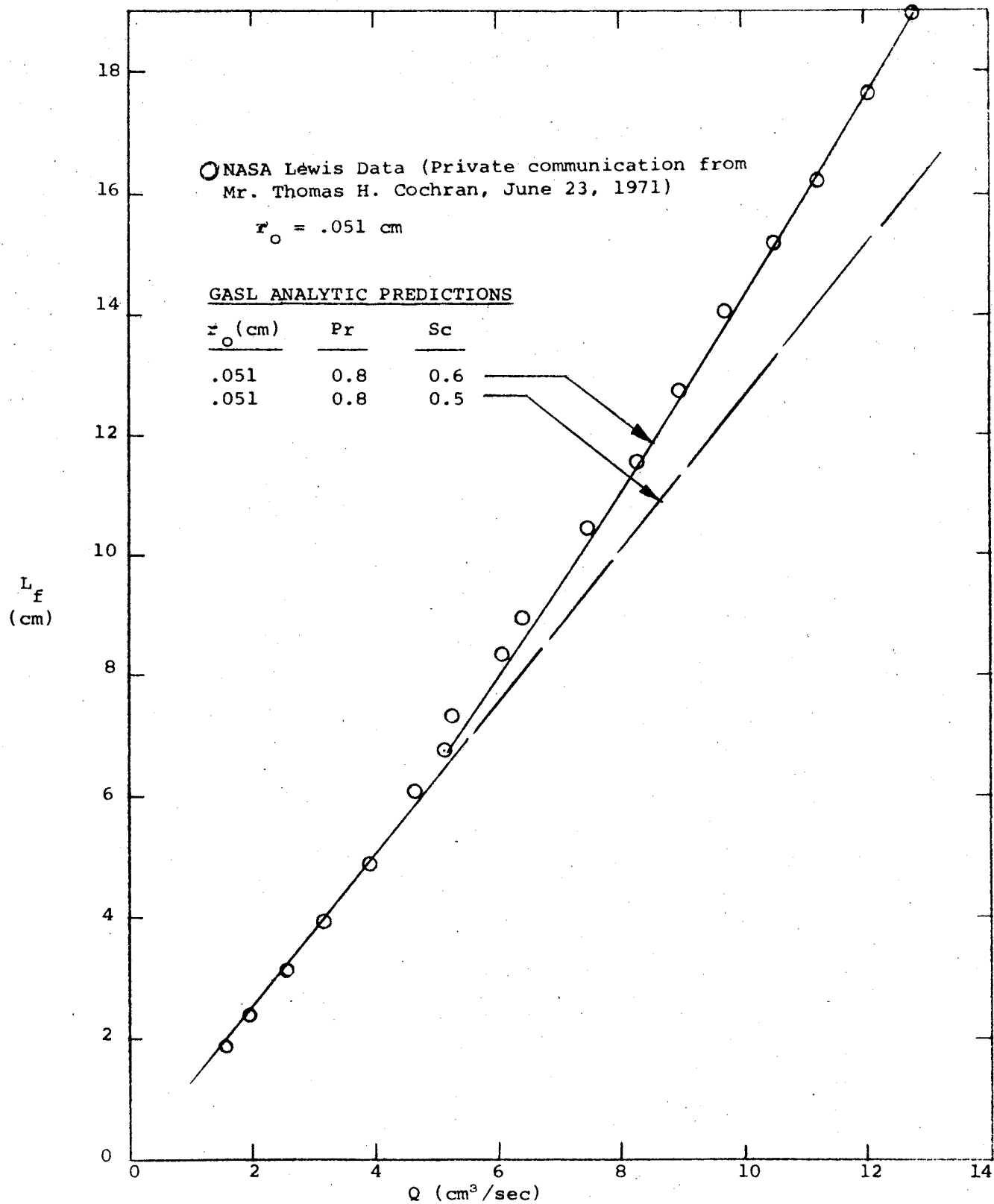


Figure 6. - Influence of Schmidt number upon analytical prediction of normal gravity flame lengths.

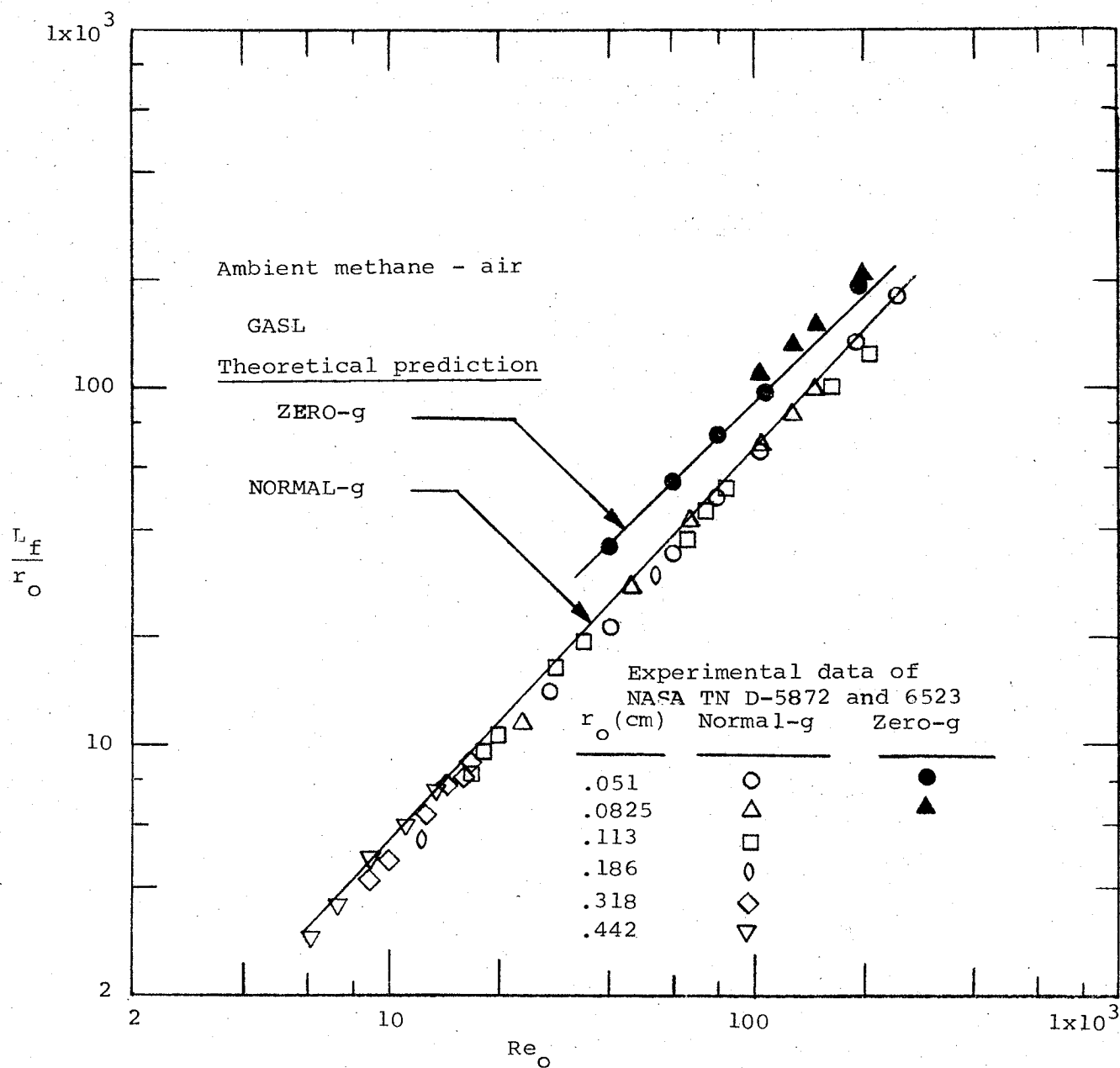


Figure 7. - Comparison of theoretical and experimental flame lengths for both normal and zero gravity.

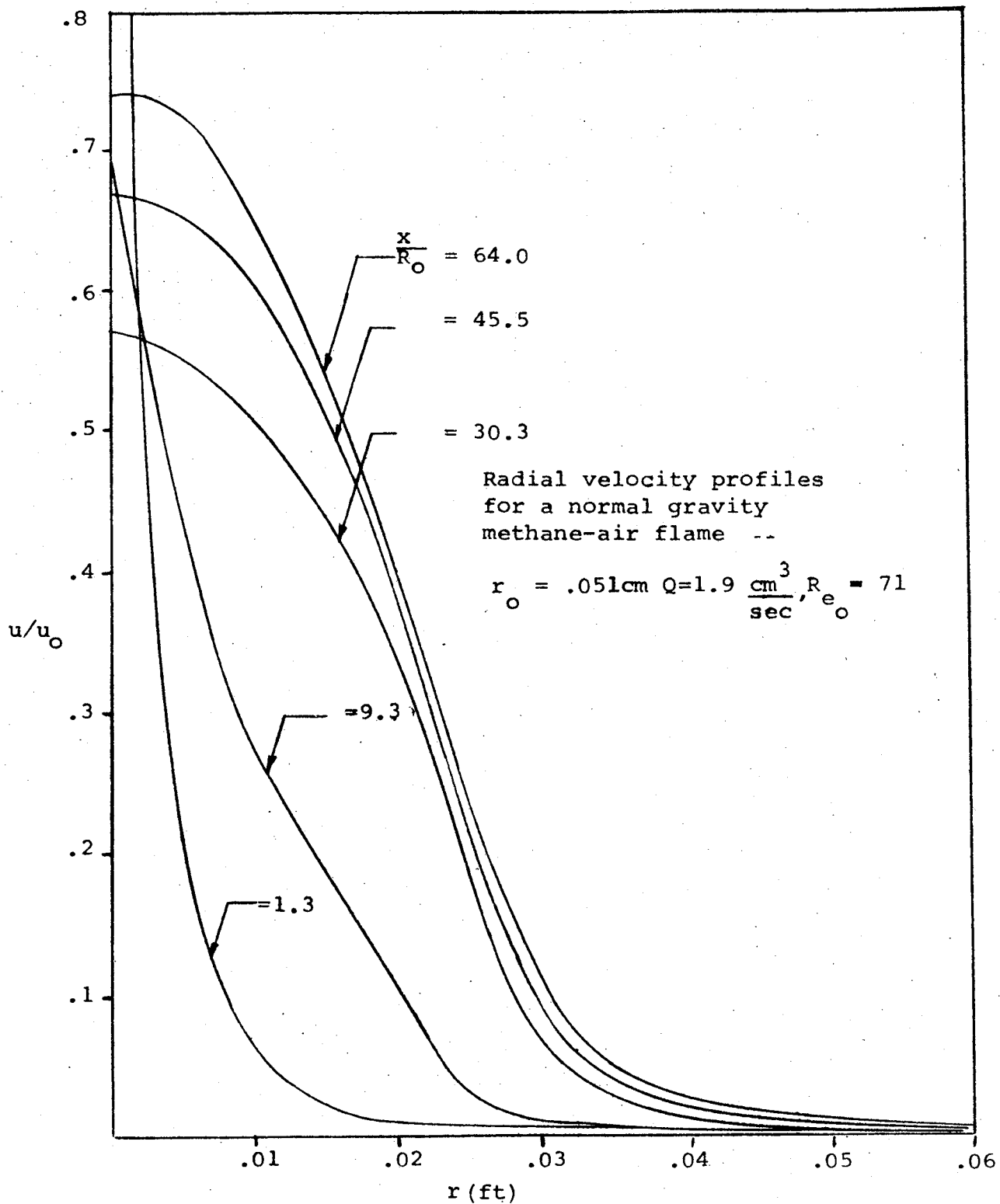


Figure 8. - GASL prediction - velocity profiles for normal gravity.

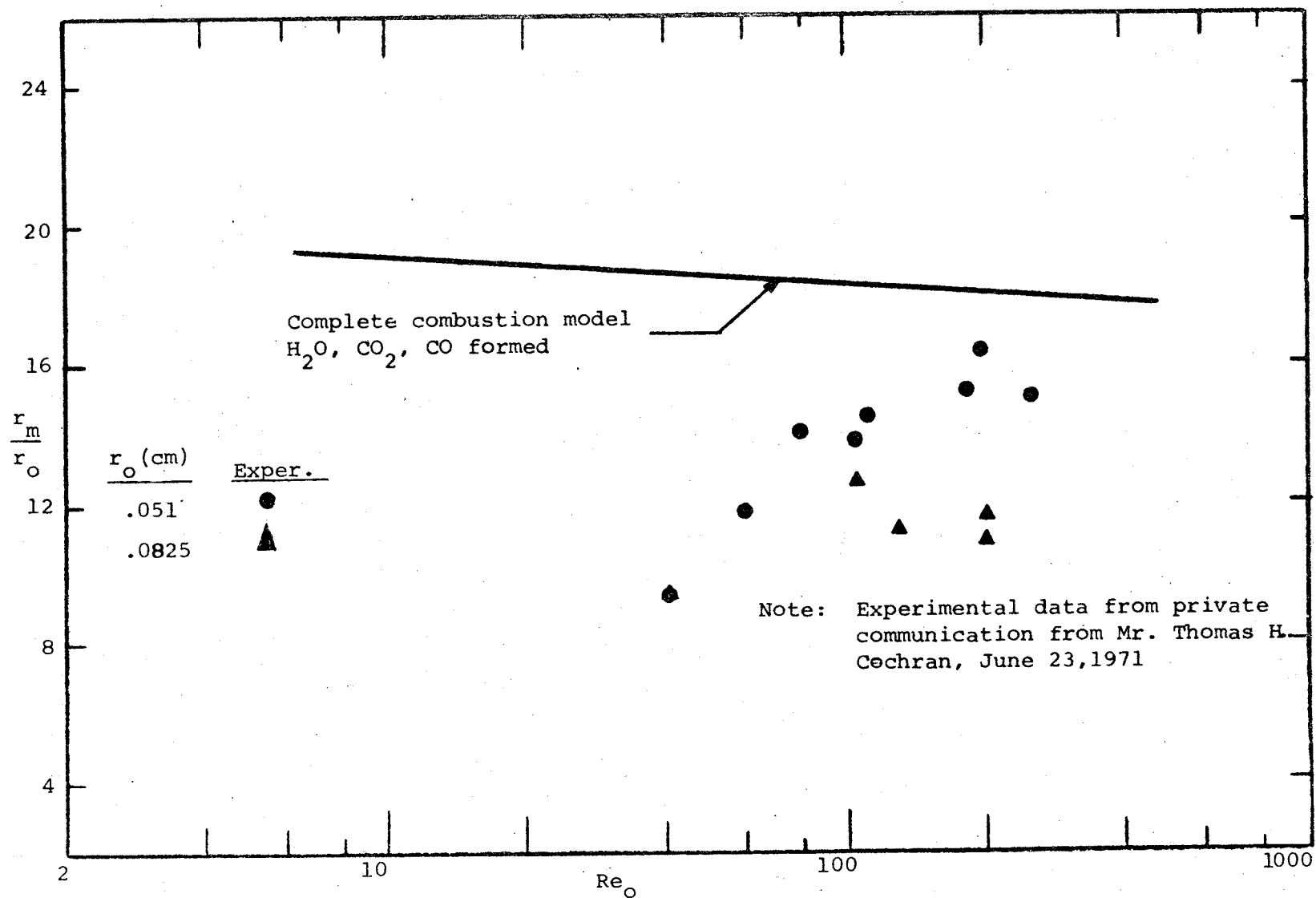


Figure 9. - Comparison of theoretical model with experimental zero-gravity flame width in ambient methane-air flames as a function of fuel Reynolds number.

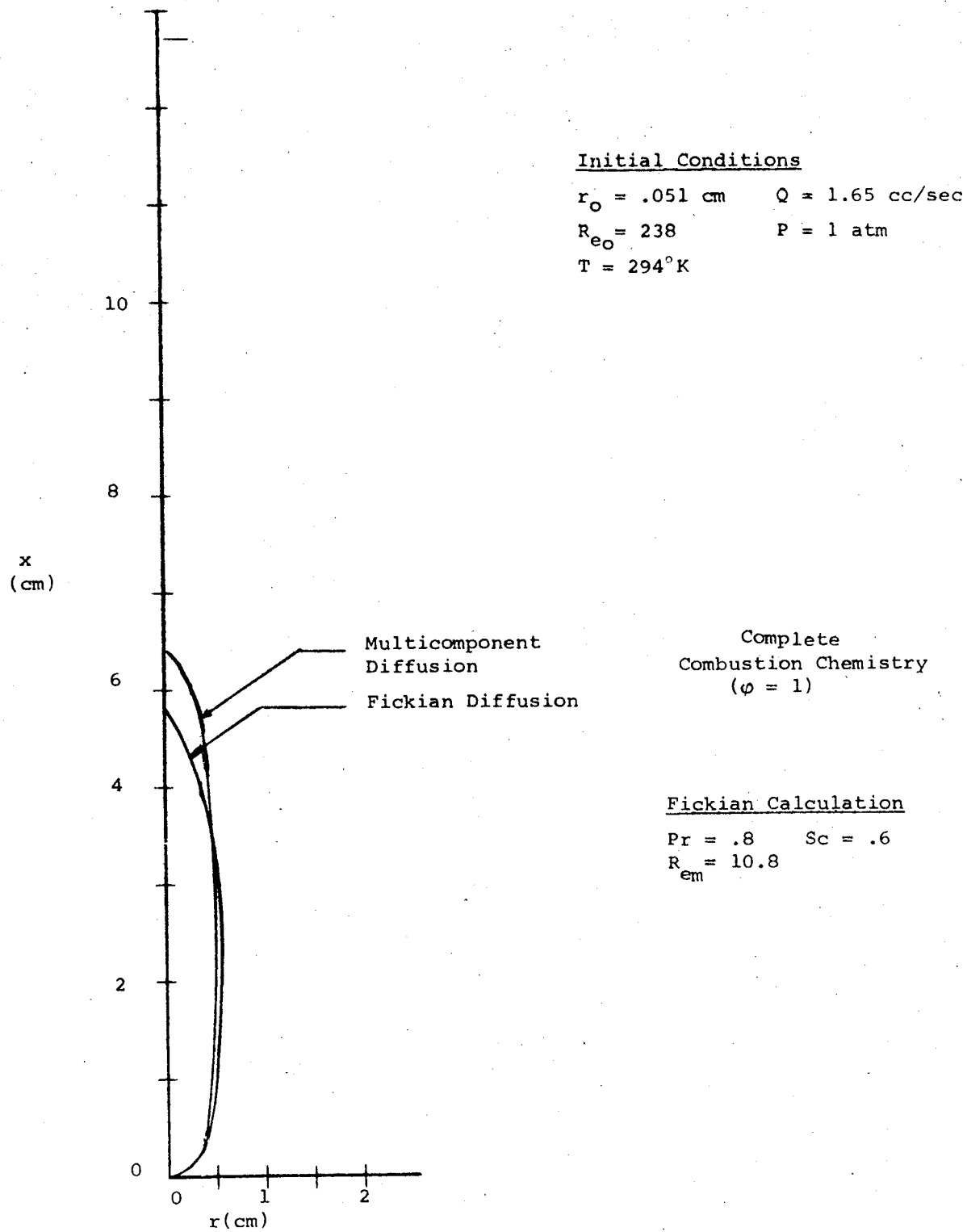


Figure 10. - Propylene/Air - Max. Q - normal gravity flame shapes.

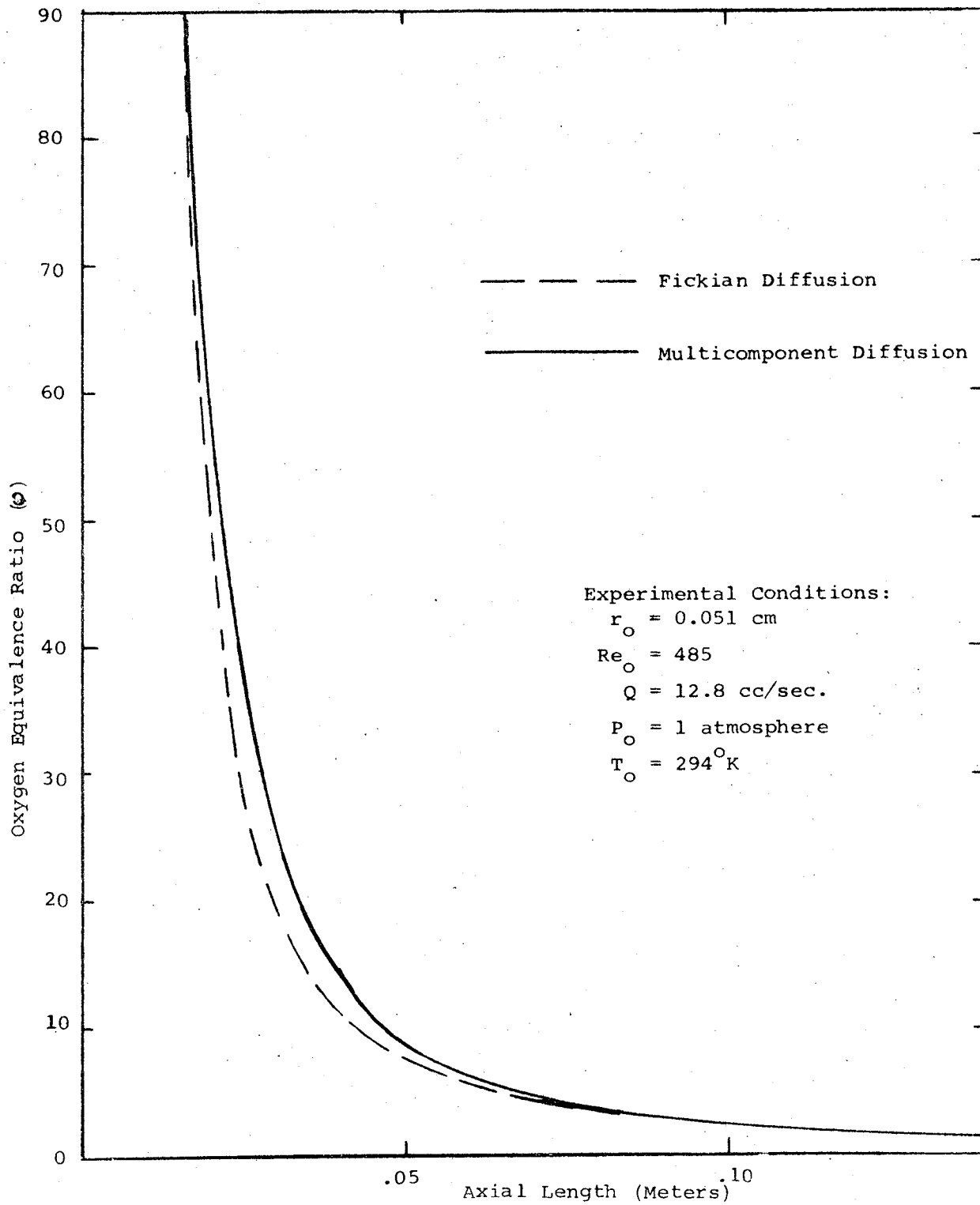


Figure 11. - Normal gravity methane/air flame axial ϕ distribution.

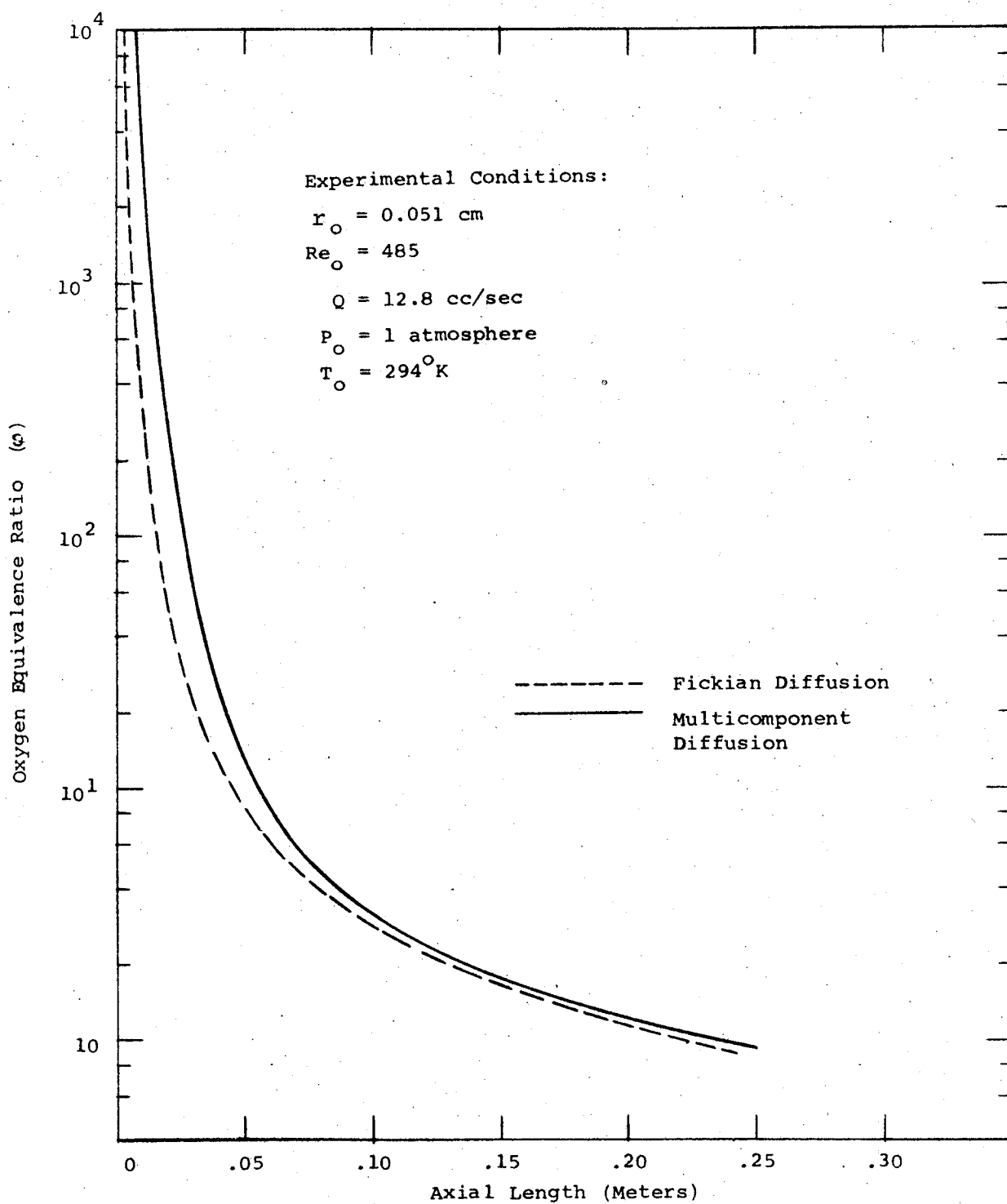


Figure 12. - Zero gravity methane/air flame axial ϕ distribution.

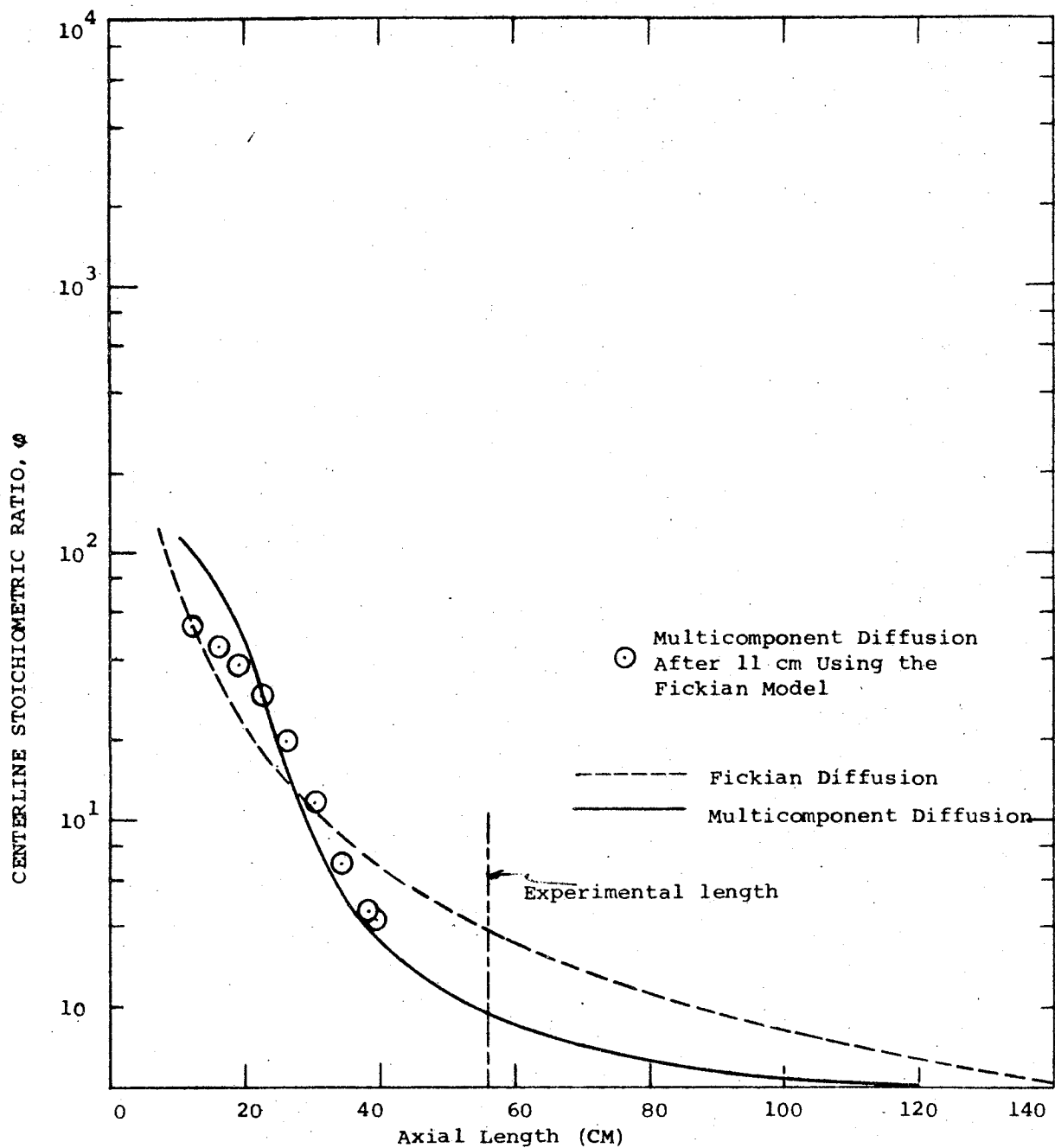


Figure 13. - Laminar H_2 -Air: Hawthorne, Ref. 9. $\bar{u}_O = 1830$ cm/sec; $d = 0.635$ cm; $Re_O = 575$. Complete combustion chemistry axial ϕ distribution.

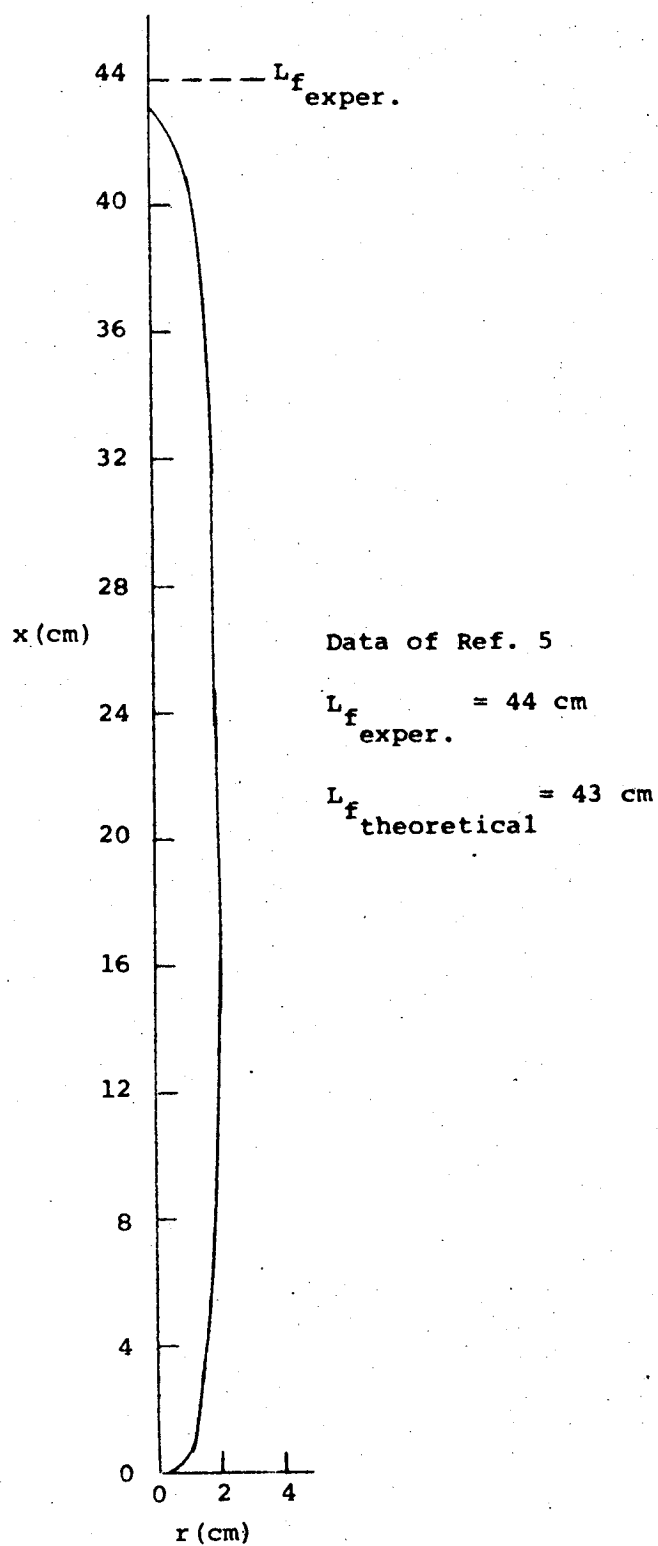


Figure 14. - Theoretical flame shape prediction for an ambient turbulent hydrogen-air normal-g flame.

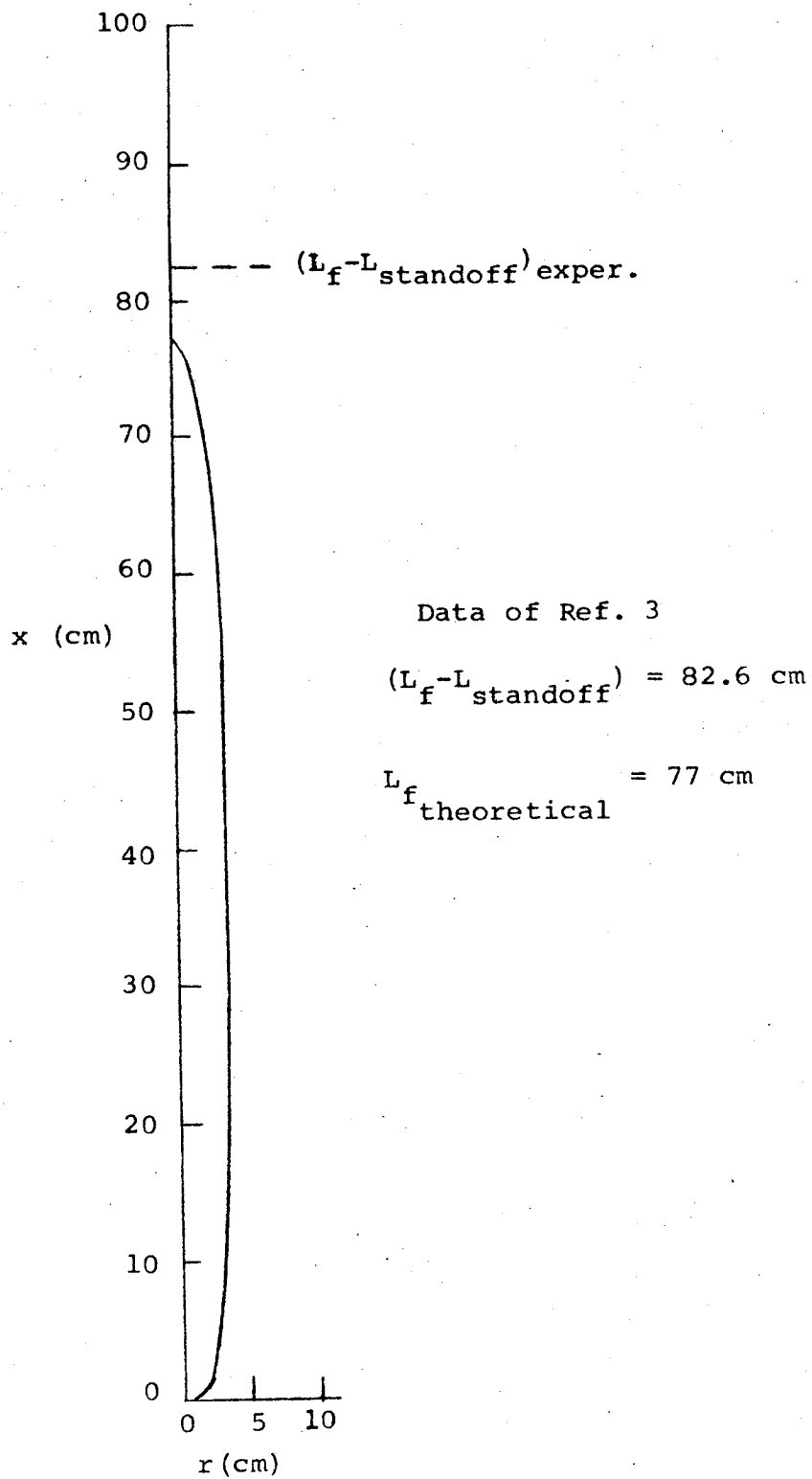


Figure 15. - Theoretical flame shape prediction for an ambient turbulent propane-air normal-g flame.

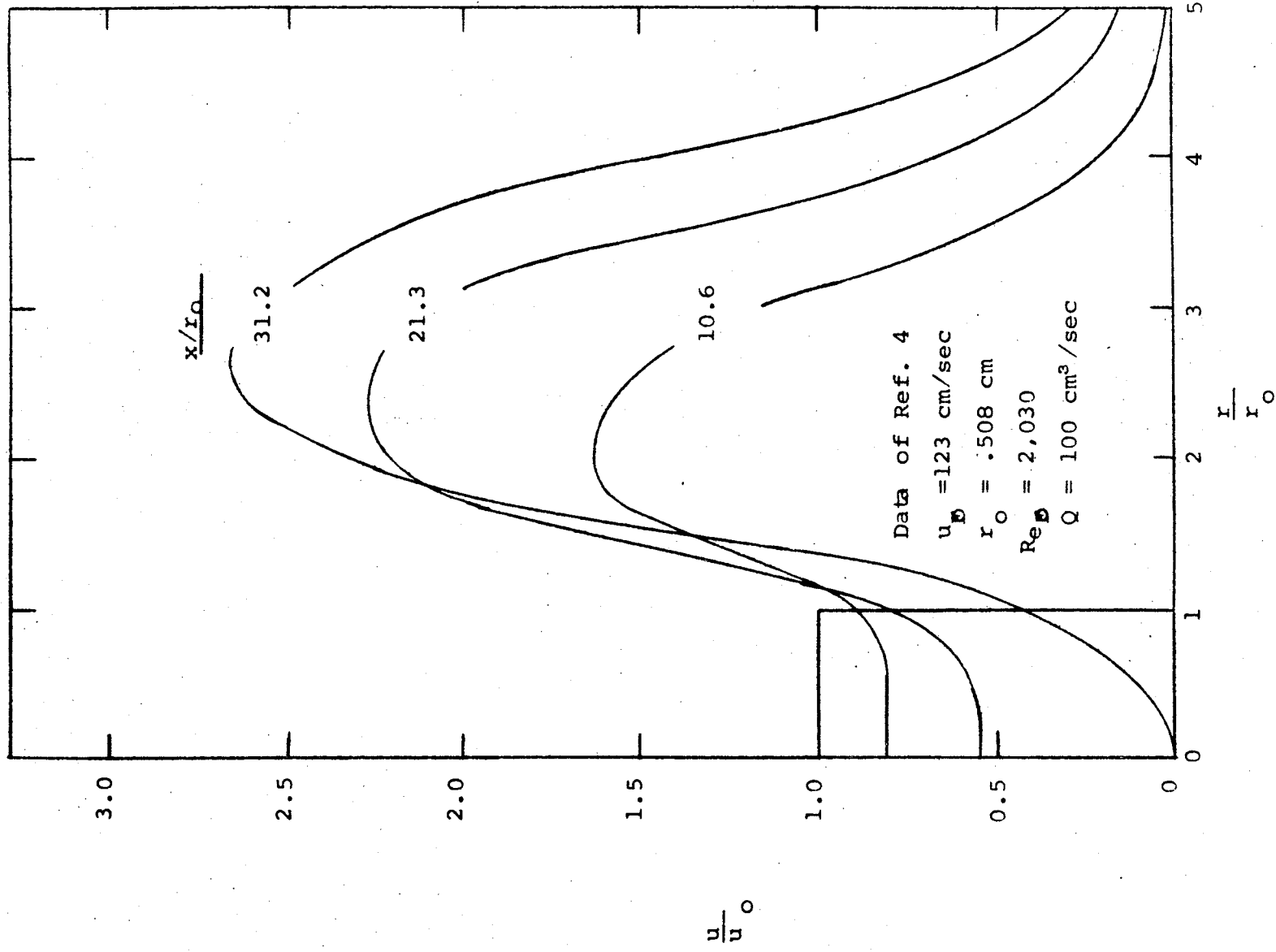


Figure 16. - Onset of recirculation in a normal-g ambient butane-air flame.

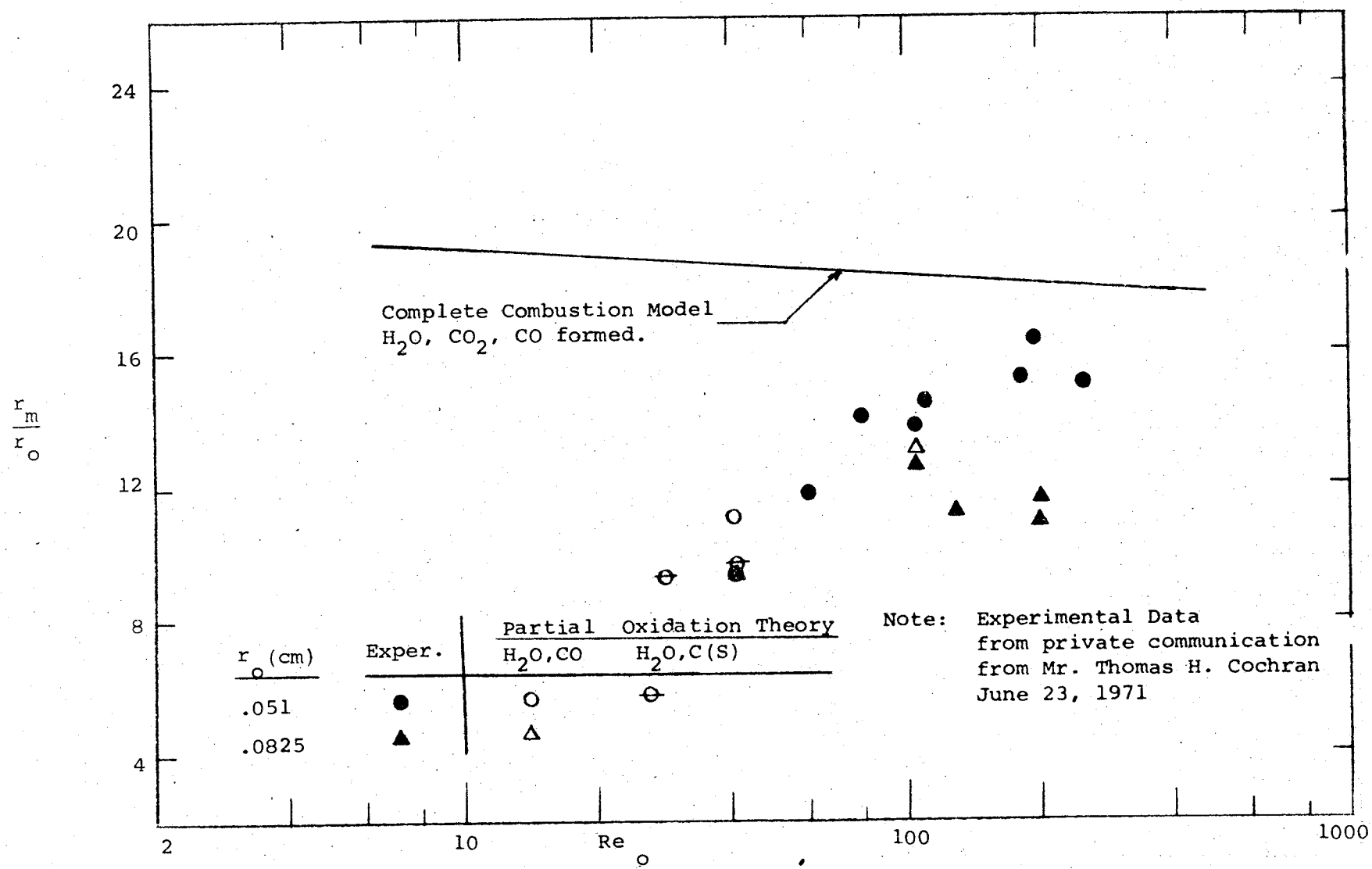


Figure 17. - Comparison of theoretical model with experimental zero-gravity flame widths in ambient methane-air flames as a function of fuel Reynolds number.

(Private communication from Mr. Thomas Cochran,
dated June 23, 1971)

Test 7 - Ambient Methane/Air

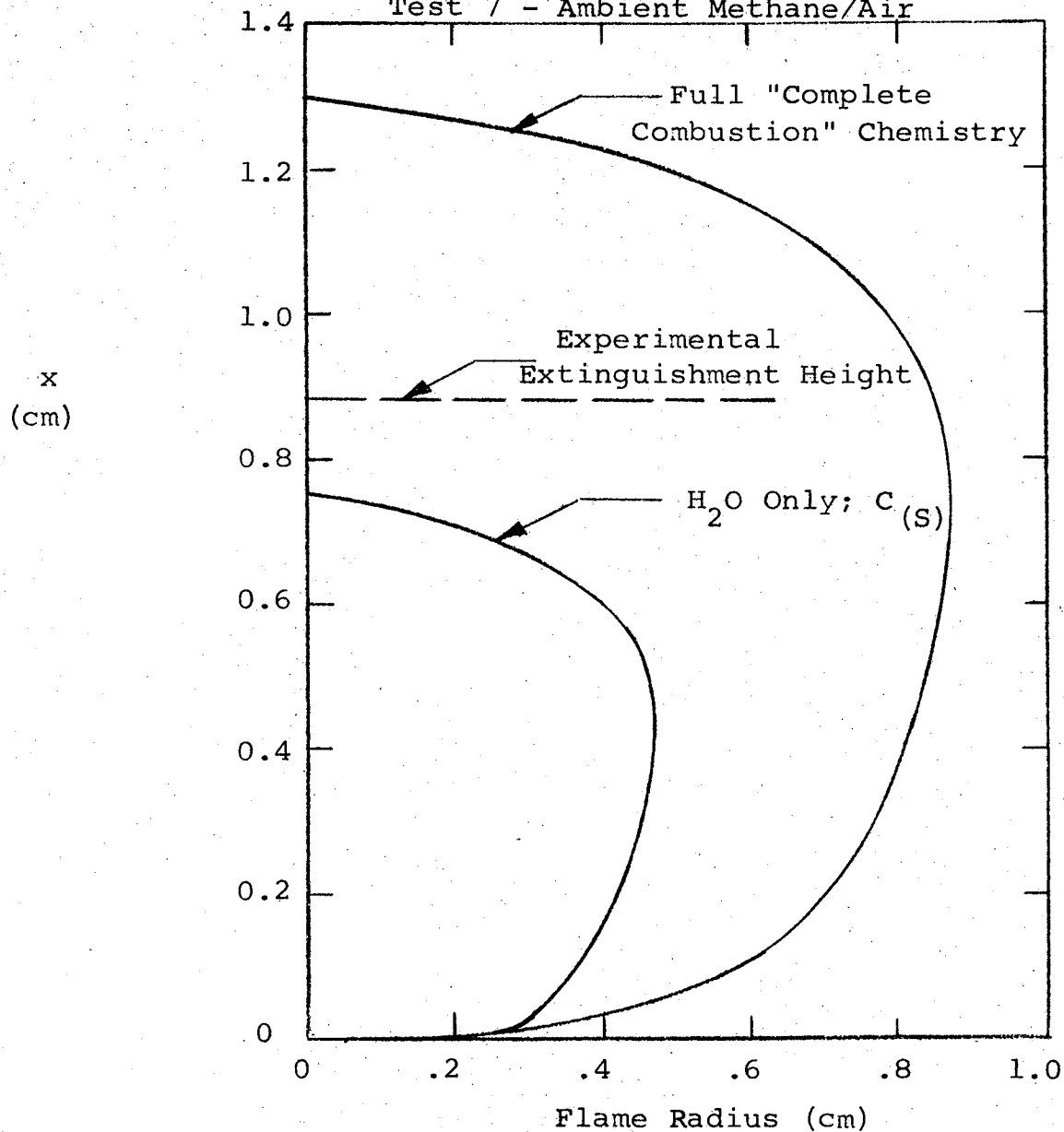


Figure 18. - Effect of chemistry model upon analytical prediction of an extinguished zero gravity flame.

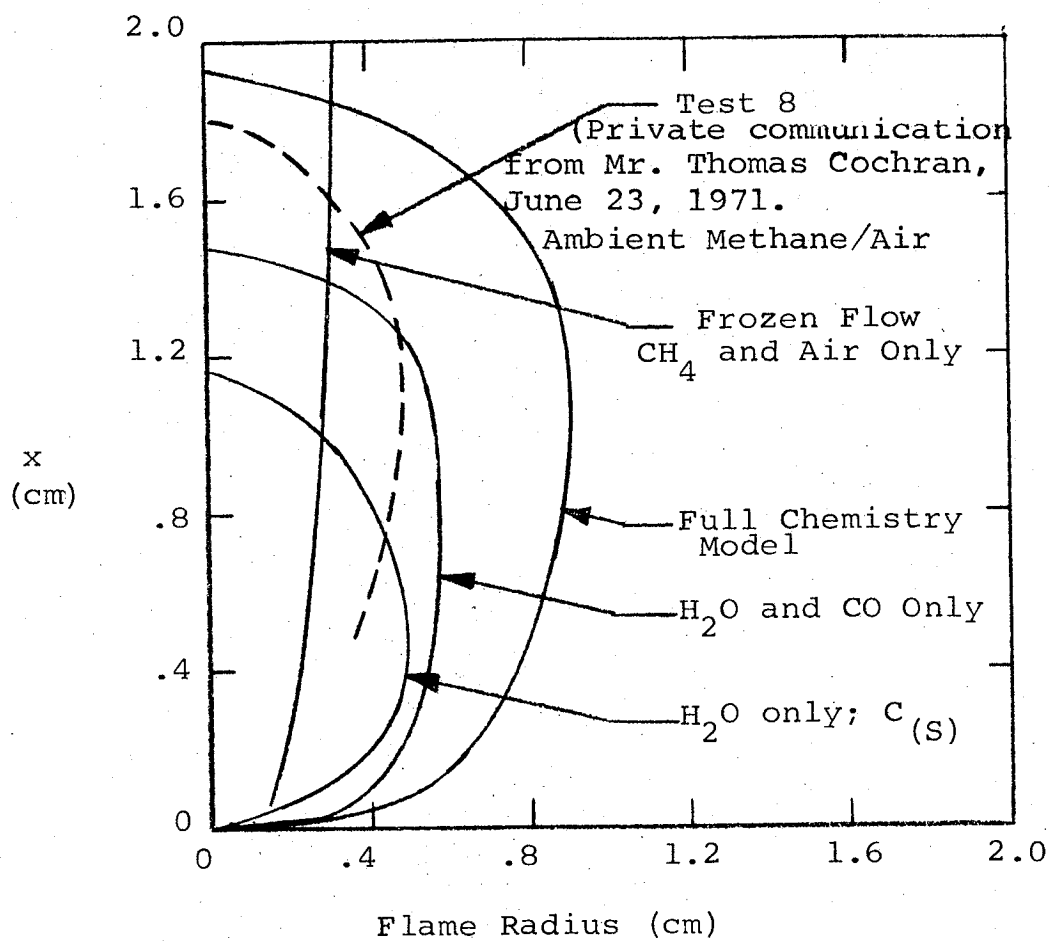


Figure 19. - Effect of chemistry model upon analytical prediction of a steady state zero gravity flame.

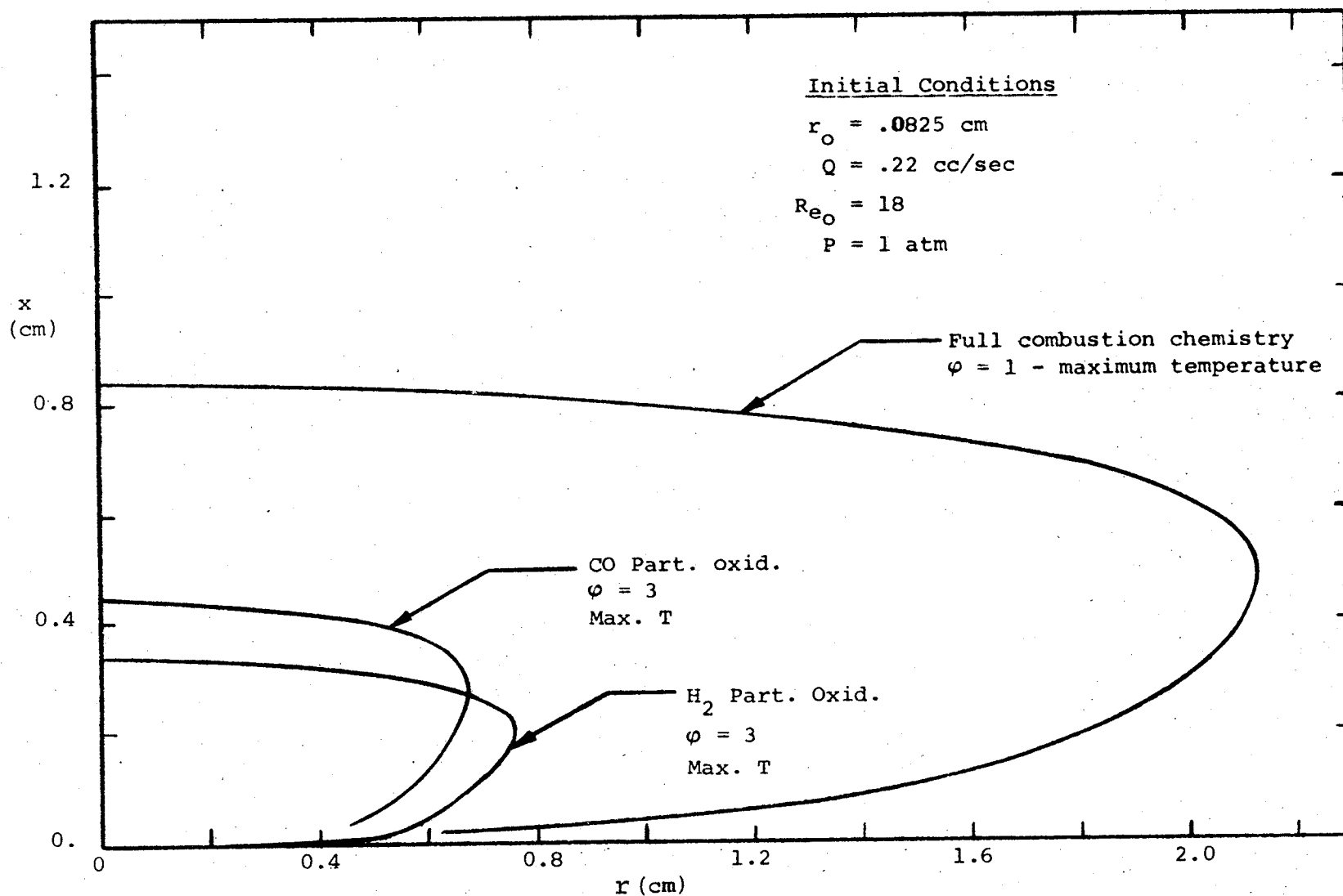


Figure 20. - Propylene/Air - min. Q - zero gravity flame shapes.

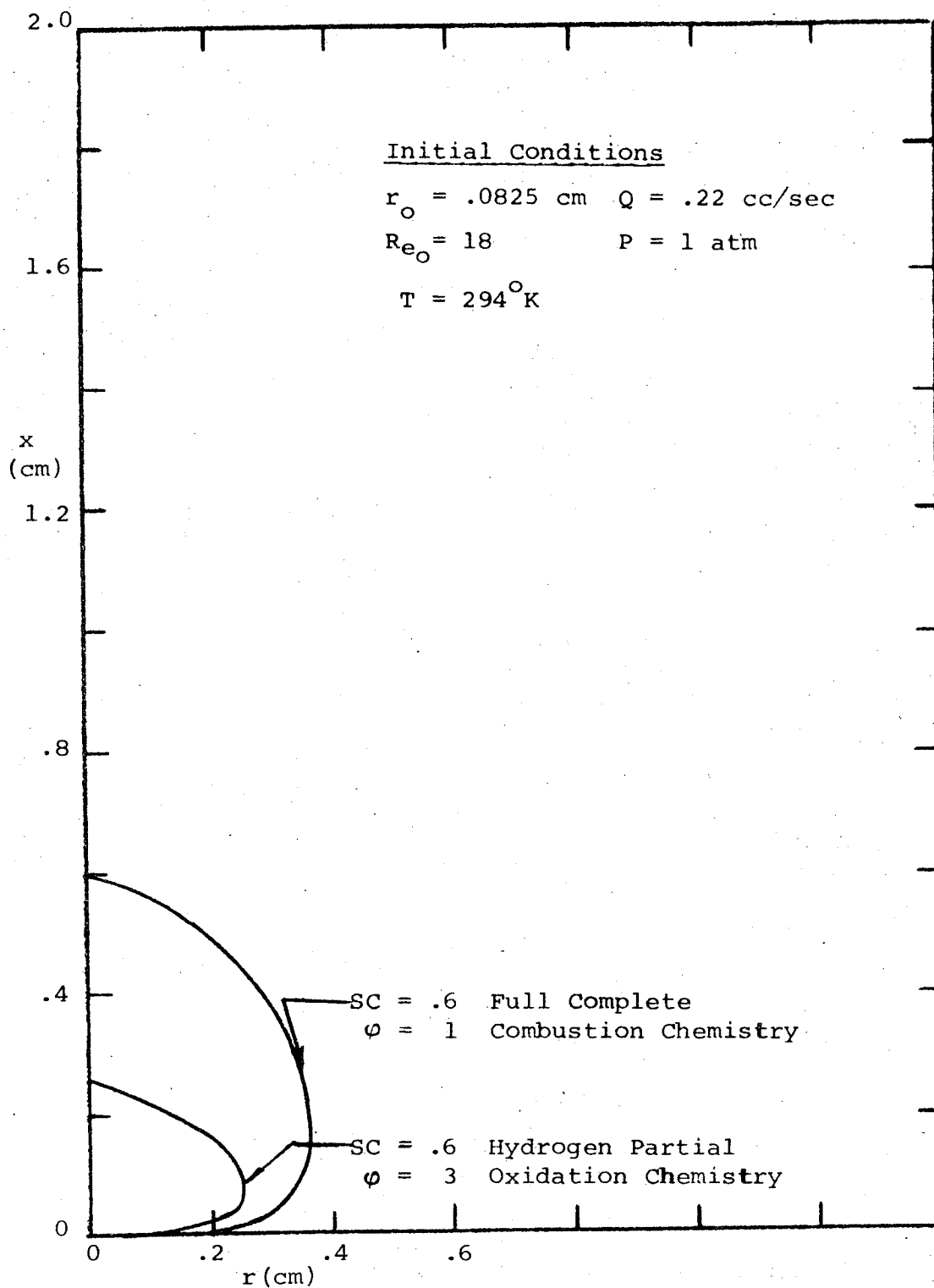


Figure 21. - Propylene/Air - min. Q - normal gravity flame shapes.

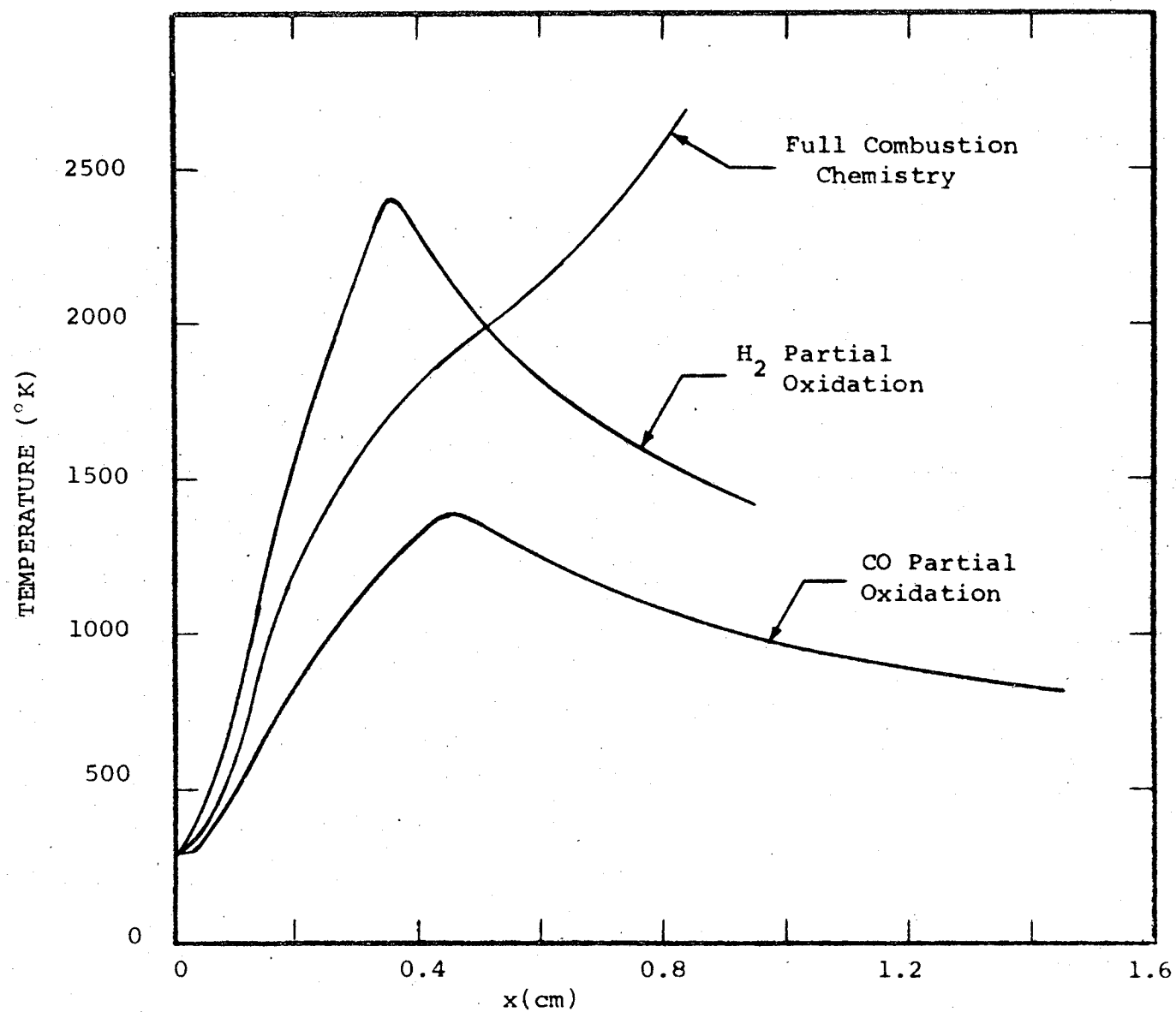


Figure 22. - Propylene/Air - min. Q - zero gravity centerline temperature histories.

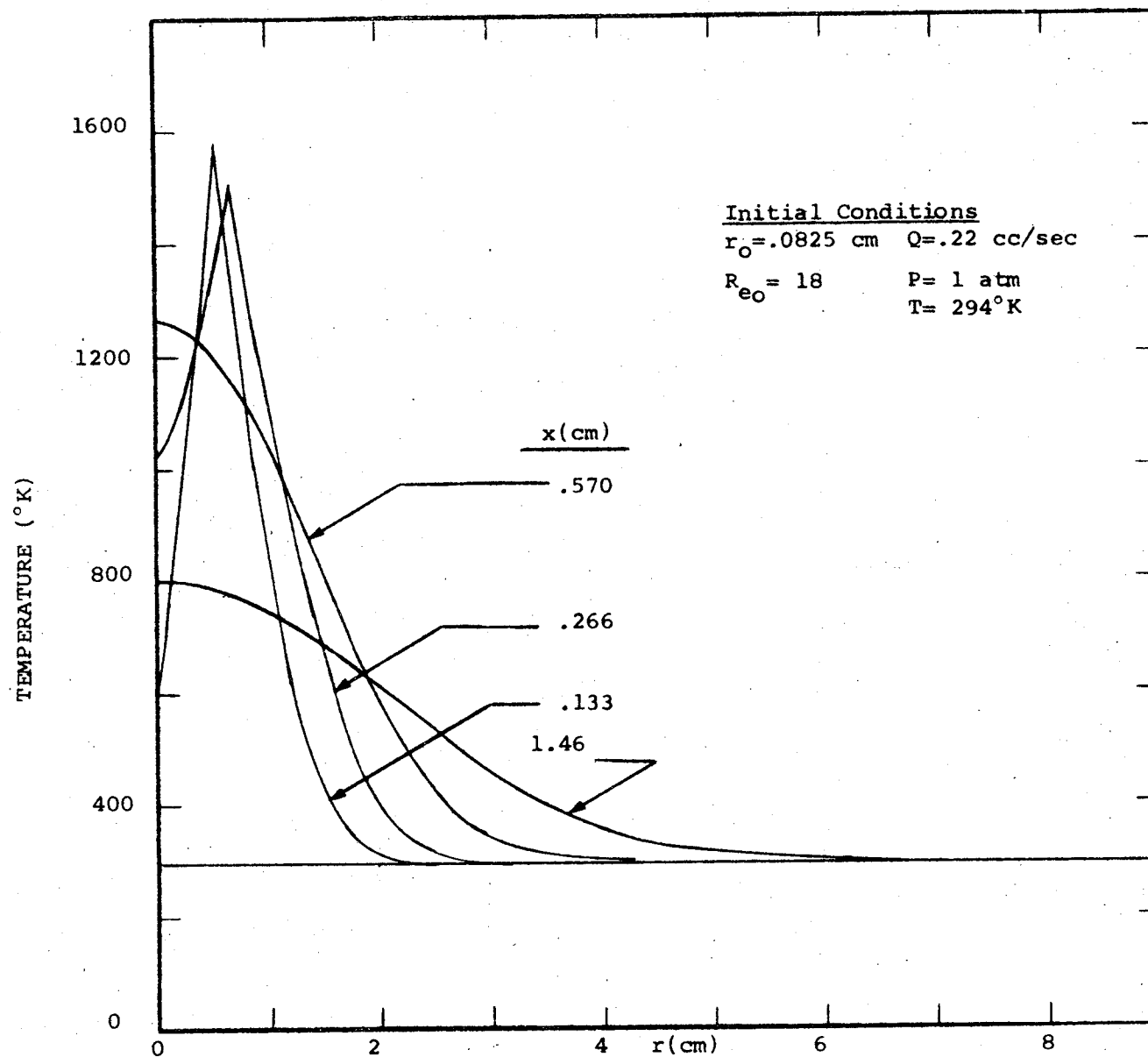


Figure 23. - Propylene/Air - min. Q - zero gravity radial temperature profiles for the CO partial oxidation chemistry model.

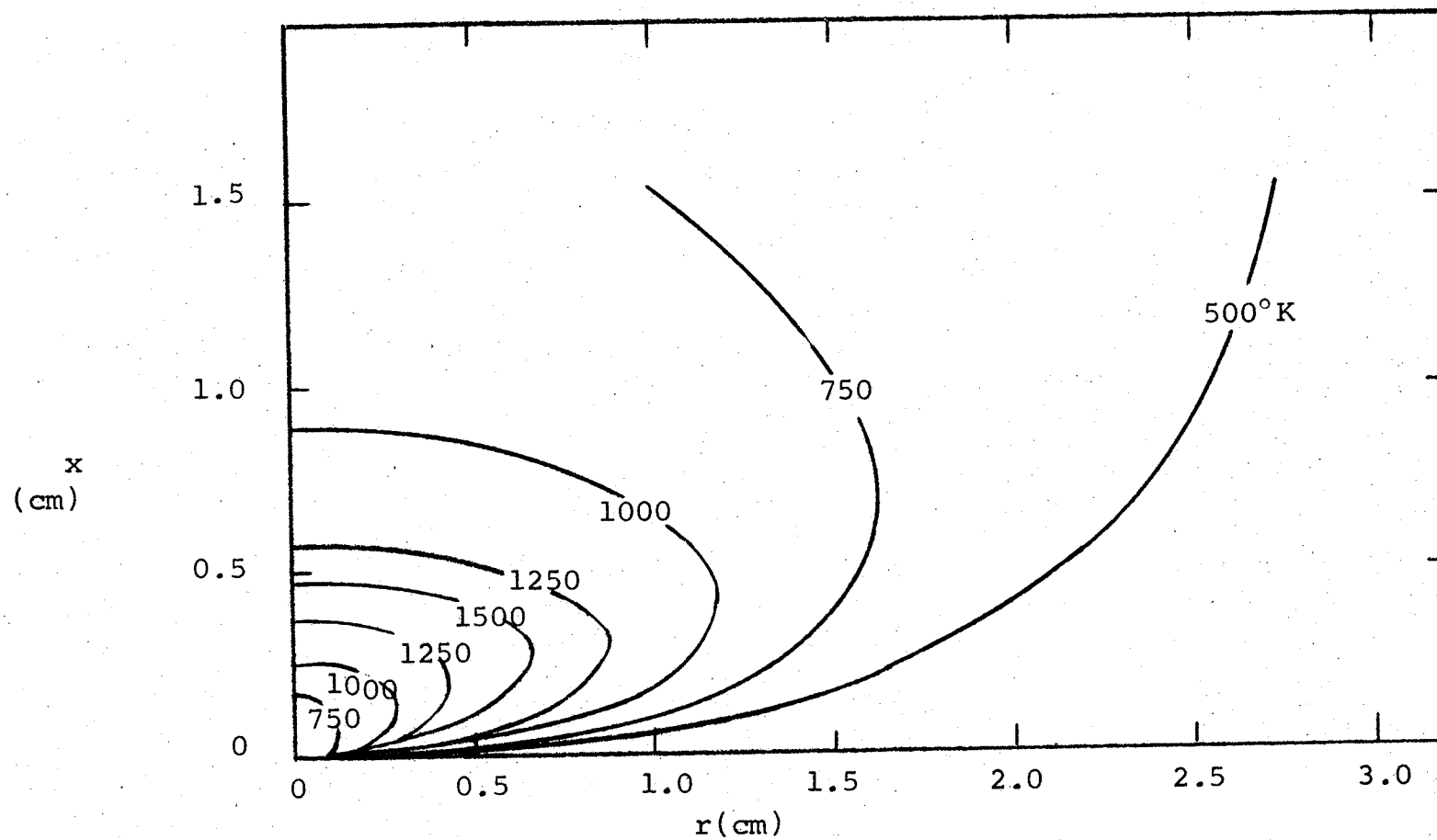


Figure 24. - Propylene/air - min. Q - zero gravity CO partial oxidation chemistry model isotherm map.

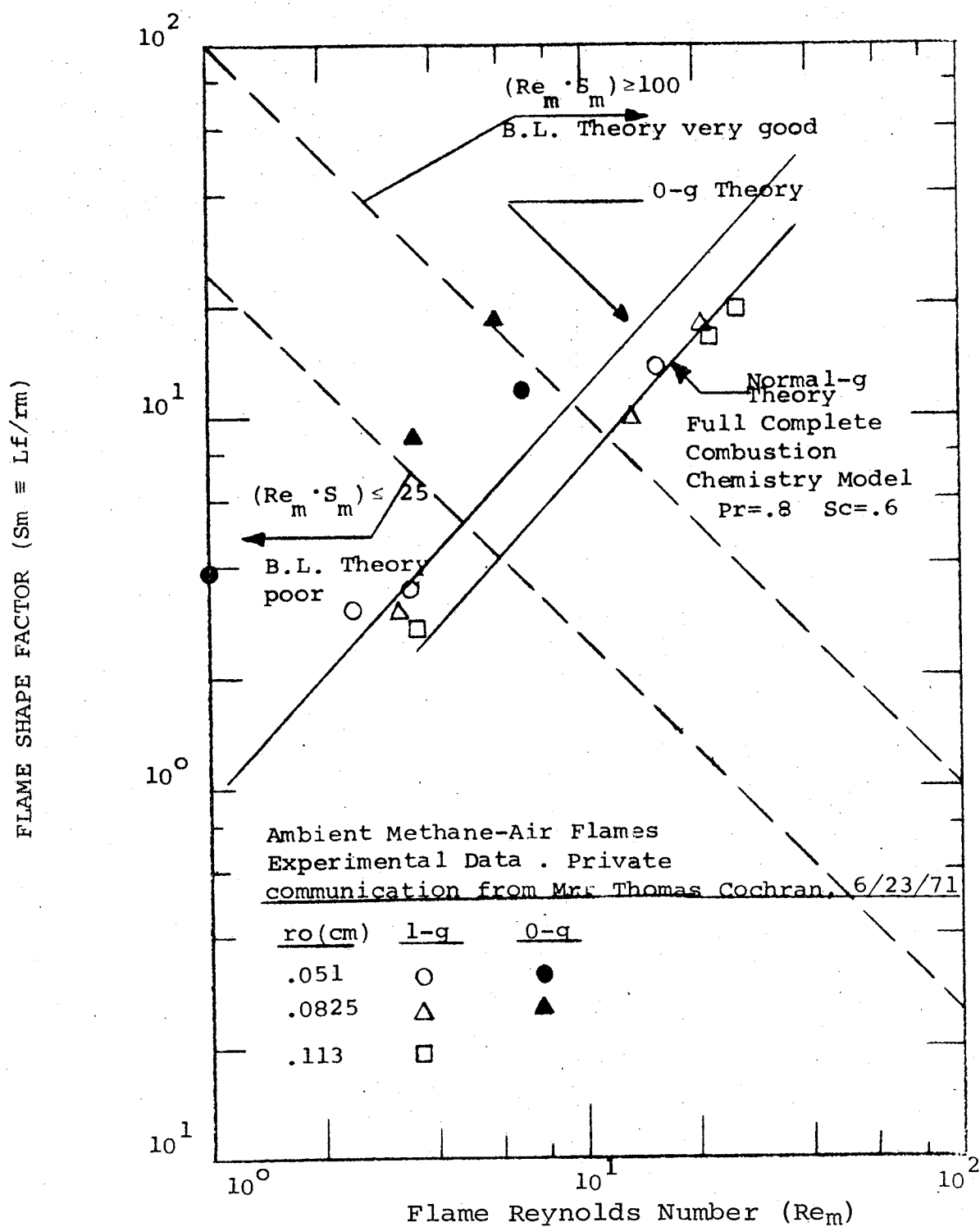


Figure 25. - Comparison of experimental and theoretical flame shape factors as a function of the characteristic flame Reynolds number for normal and zero gravity methane-air flames.

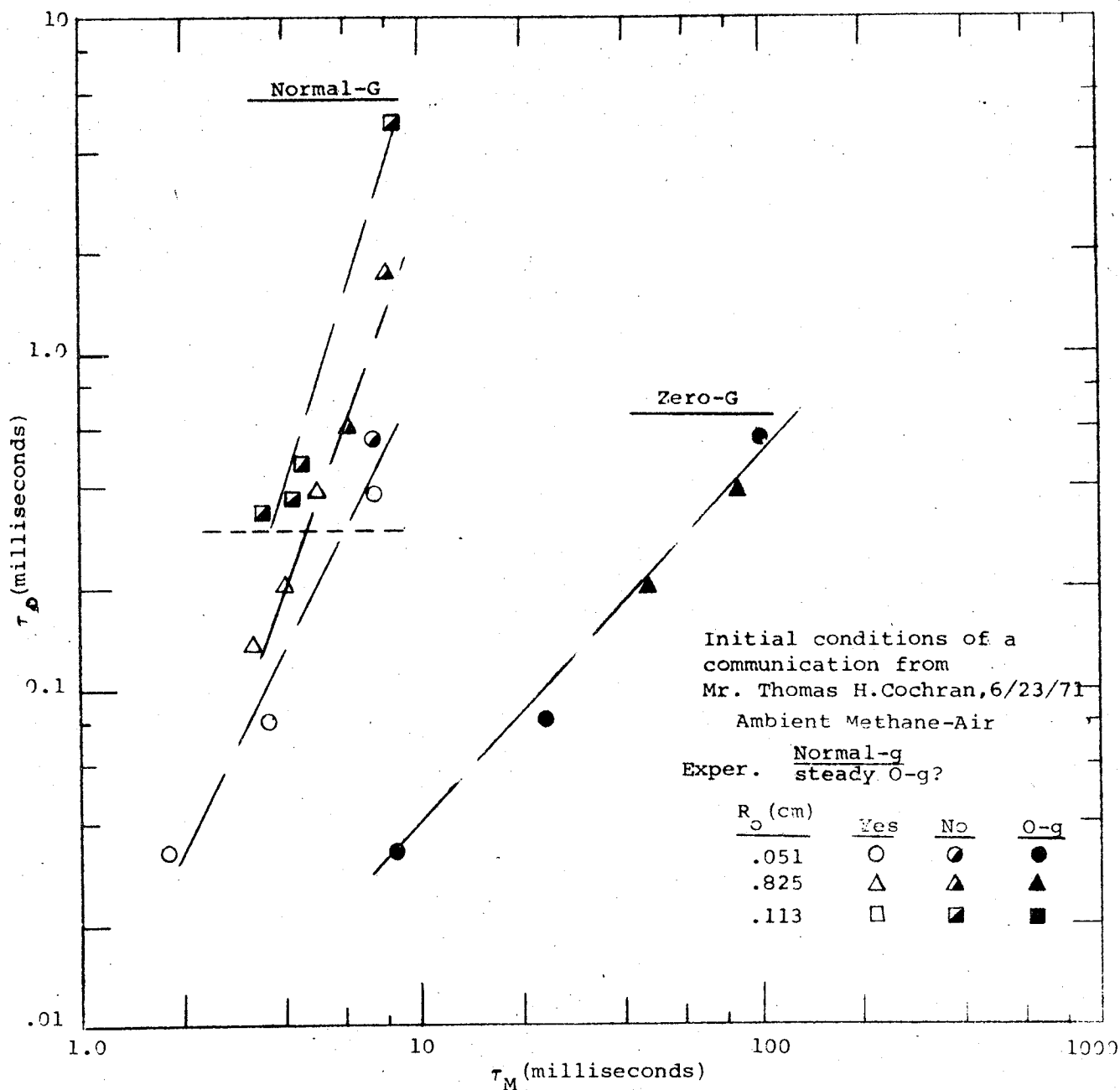


Figure 26. - Theoretical relation between flame and fuel residence times for laminar methane-air flames.

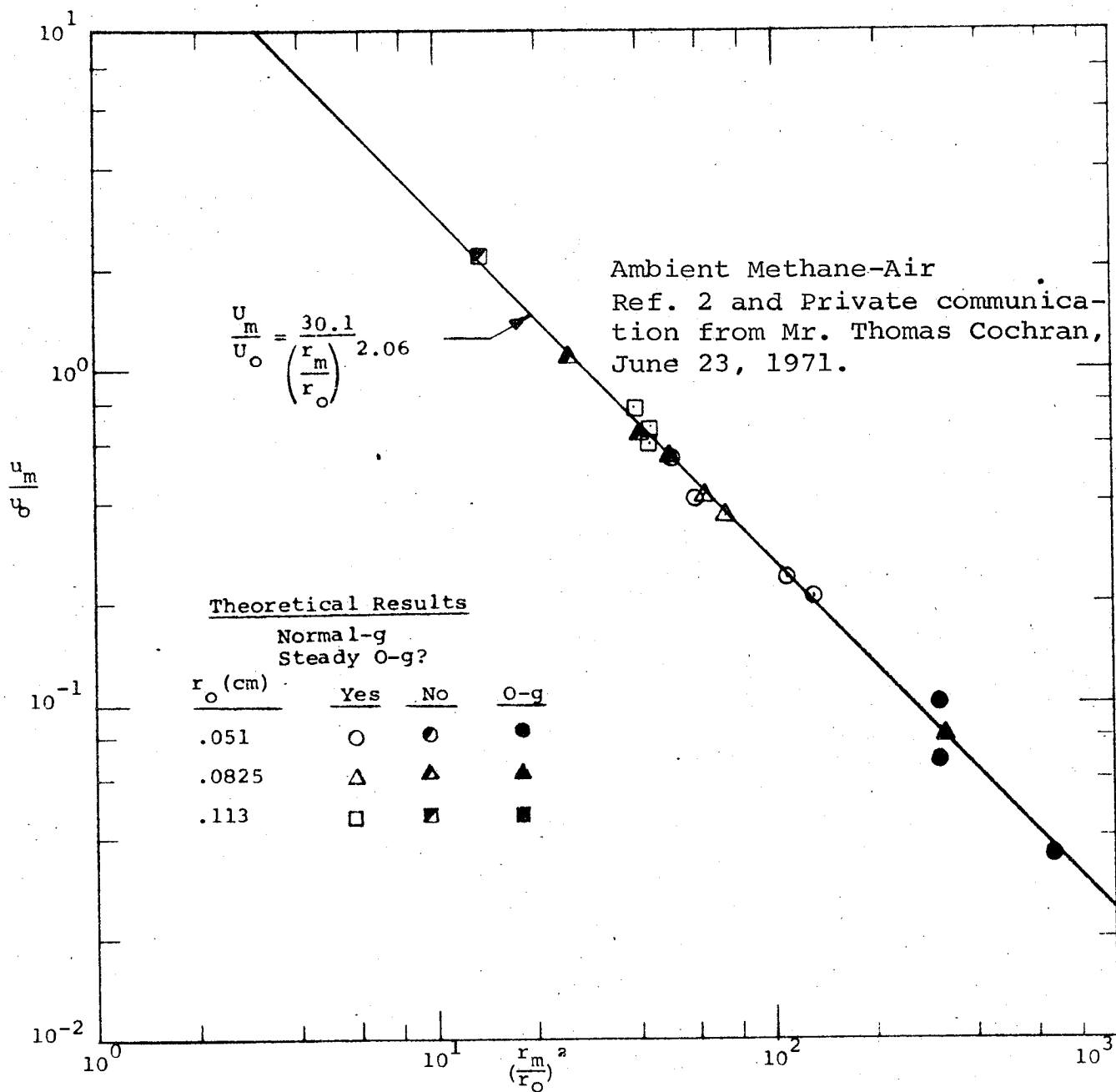


Figure 27. $-u_m/u_o$ as a function of r_m/r_o for laminar methane-air-flames.

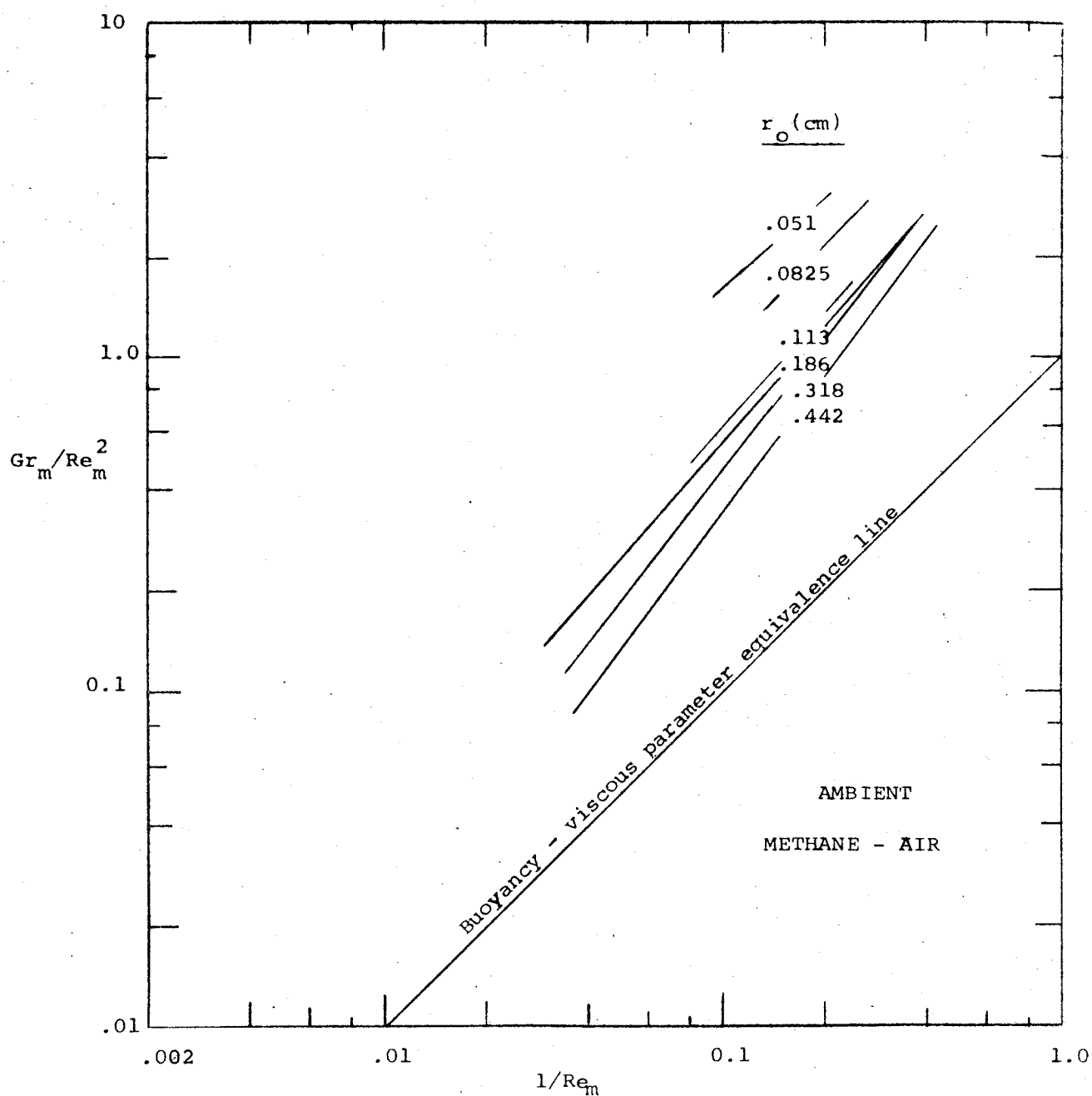


Figure 28. - Buoyancy-inertia parameter versus viscous-inertia parameter as evaluated at the maximum radius flame edge in the theoretical normal gravity methane-air flames.

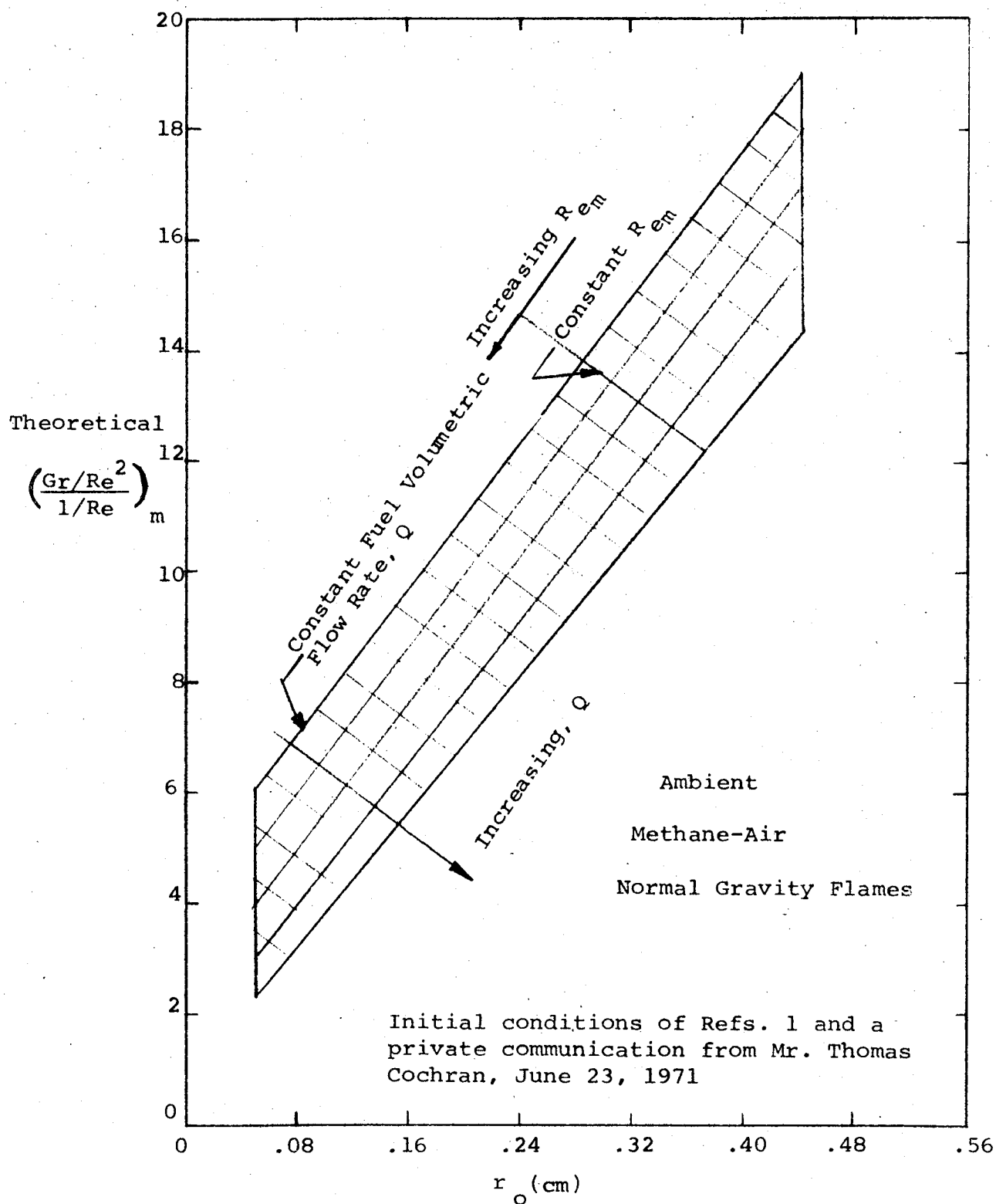


Figure 29. - Ratio of buoyancy and viscous parameters evaluated at maximum flame radius versus initial fuel radius.

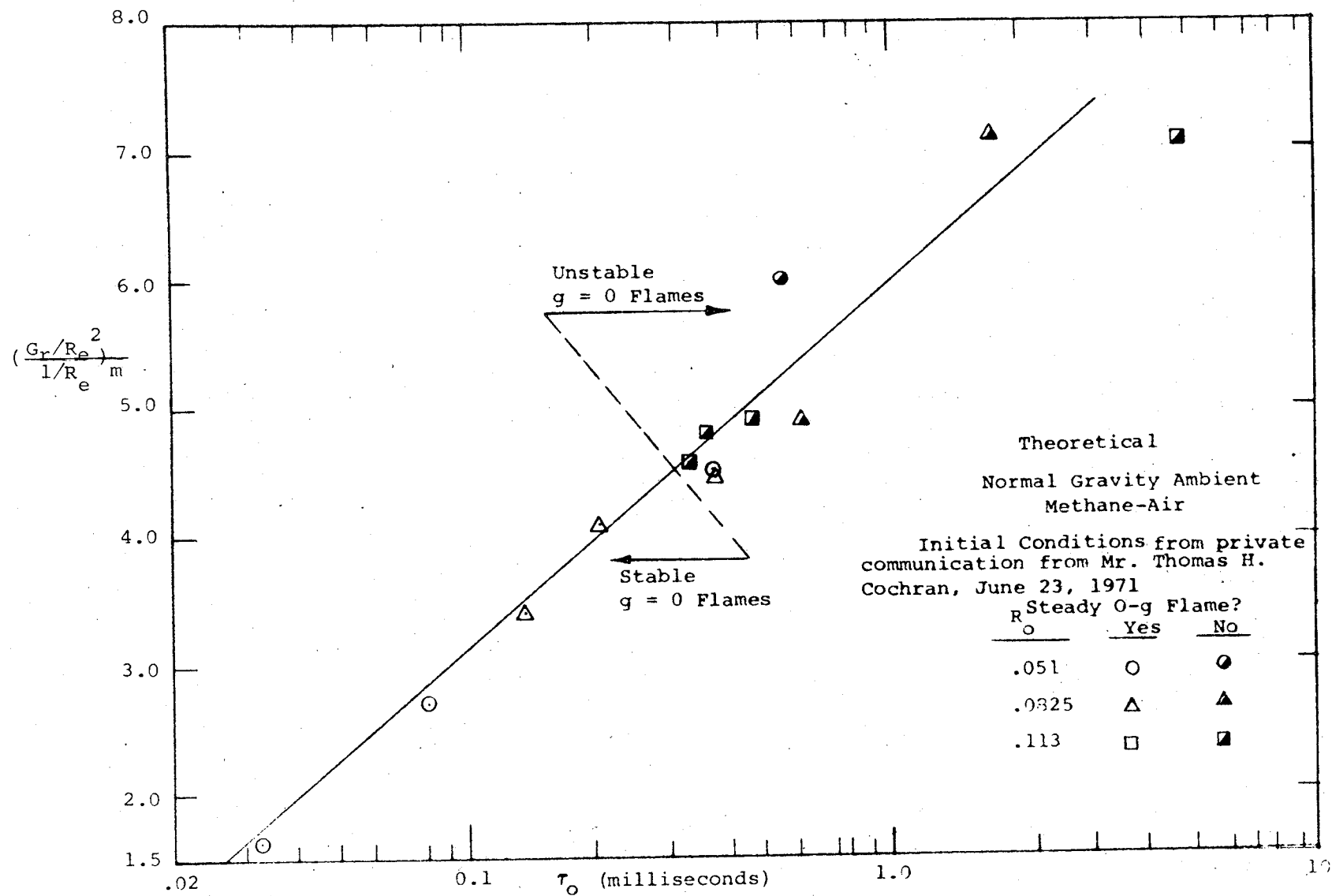


Figure 30. - Stability criterion for 0-g methane-air flames as a function of $(Gr/Re)_m$ and τ_0 for the GASL theoretical model.

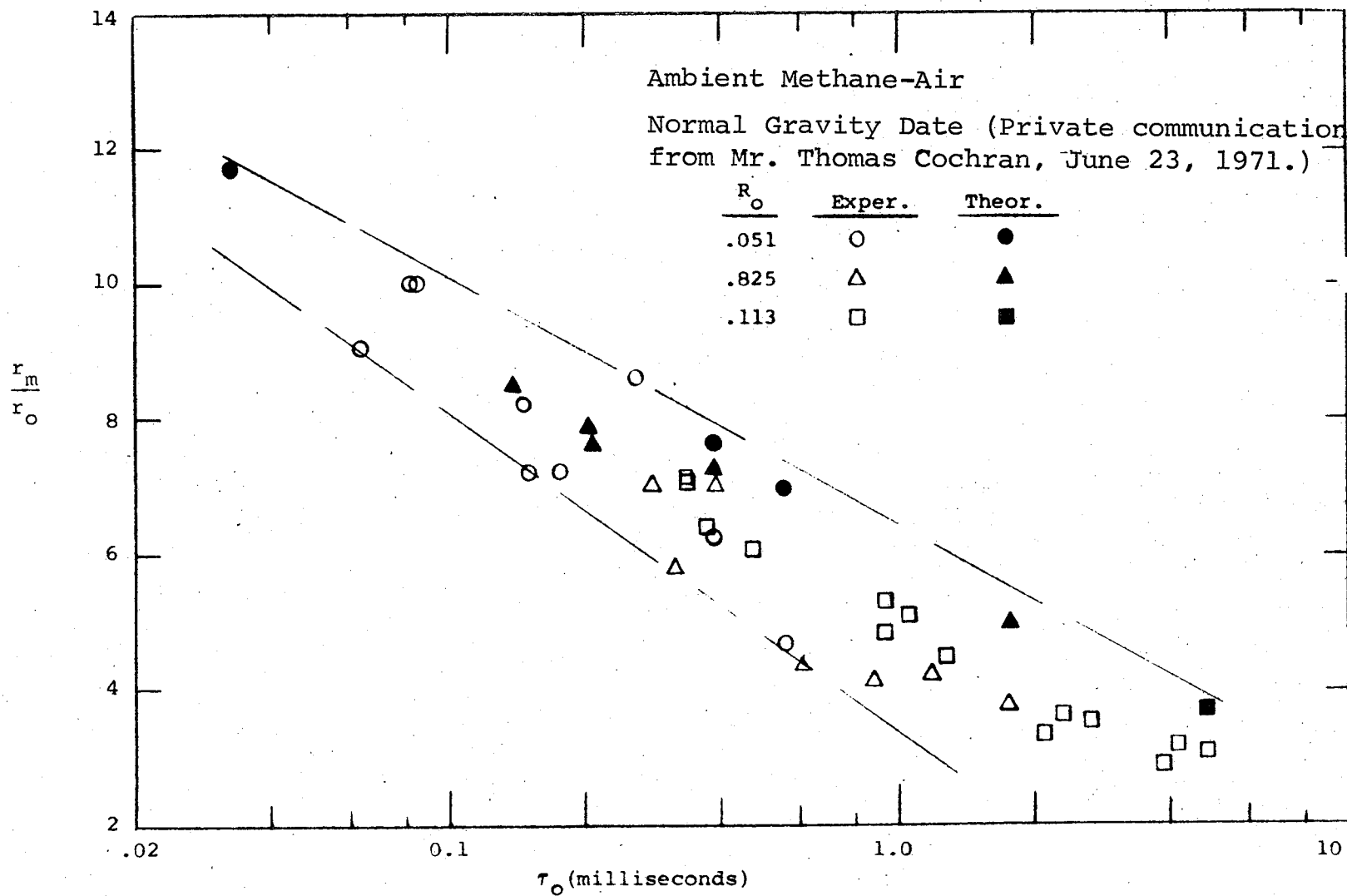


Figure 31. - r_m/r_o as a function of τ_o in normal gravity methane-air flames.

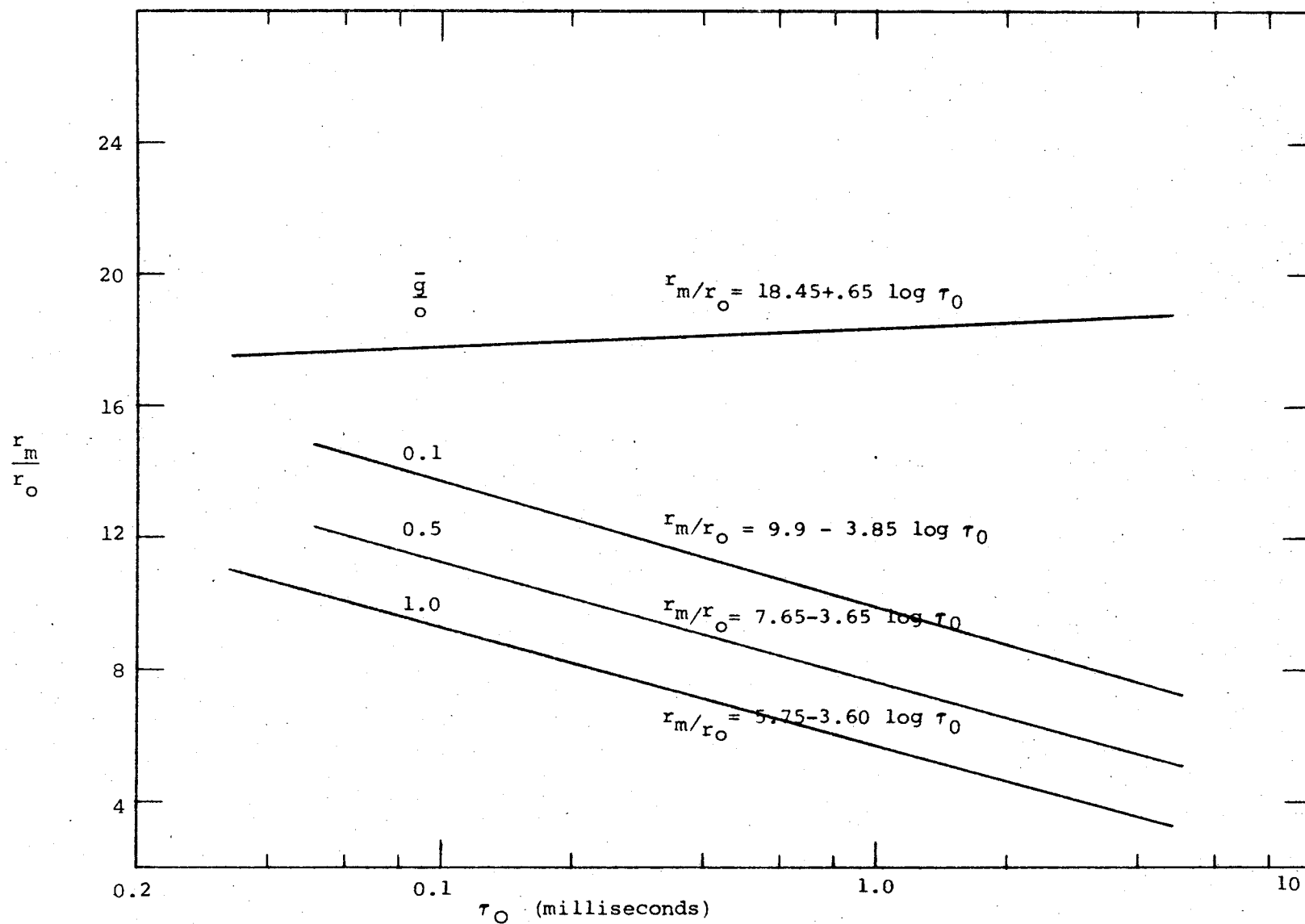


Figure 32. - Theoretical predictions of r_m/r_o as a function of τ_o and gravity level for laminar methane-air diffusion flames.

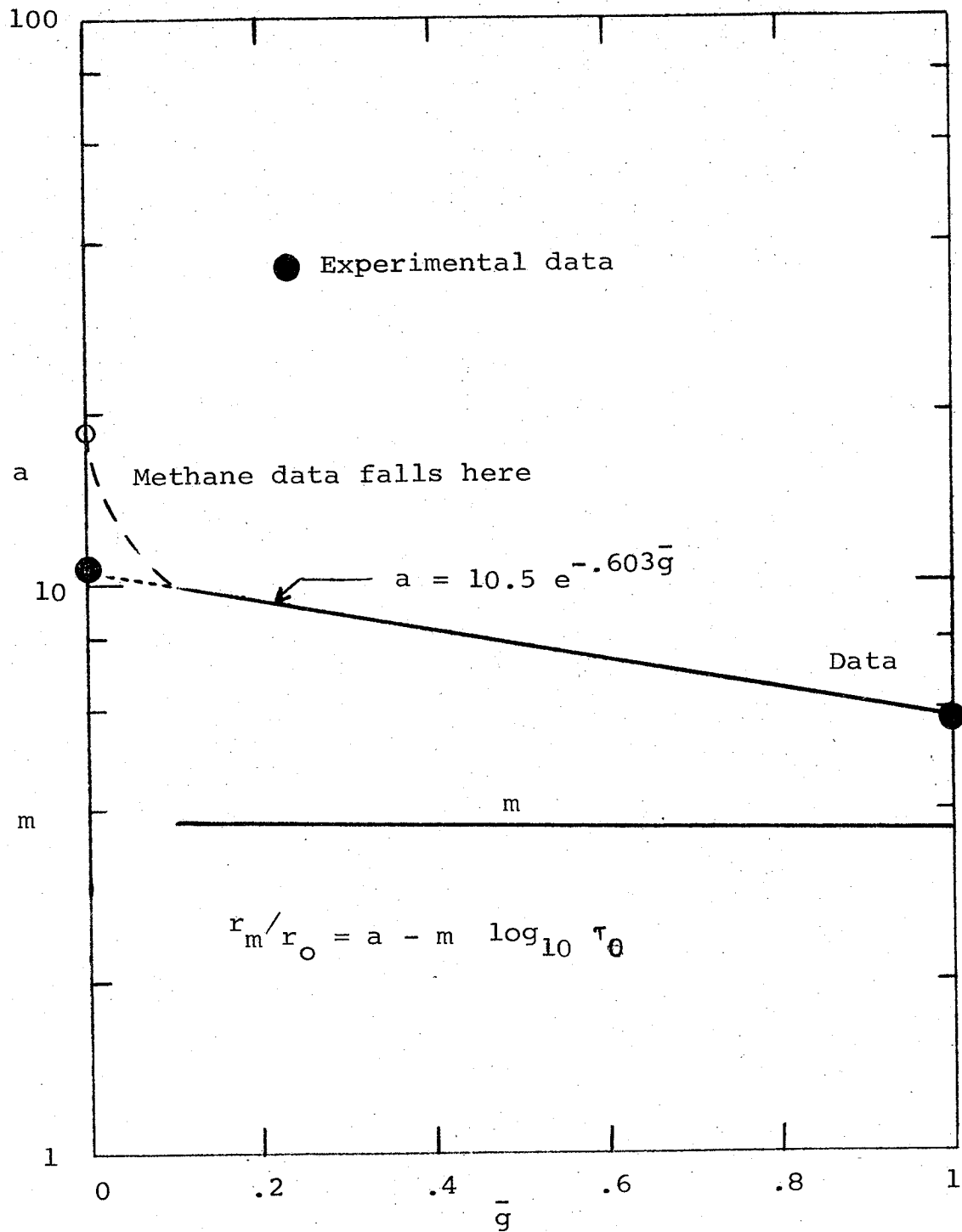


Figure 33. - The influence of gravity level upon the theoretical relation between r_m/r_o and τ_0 .

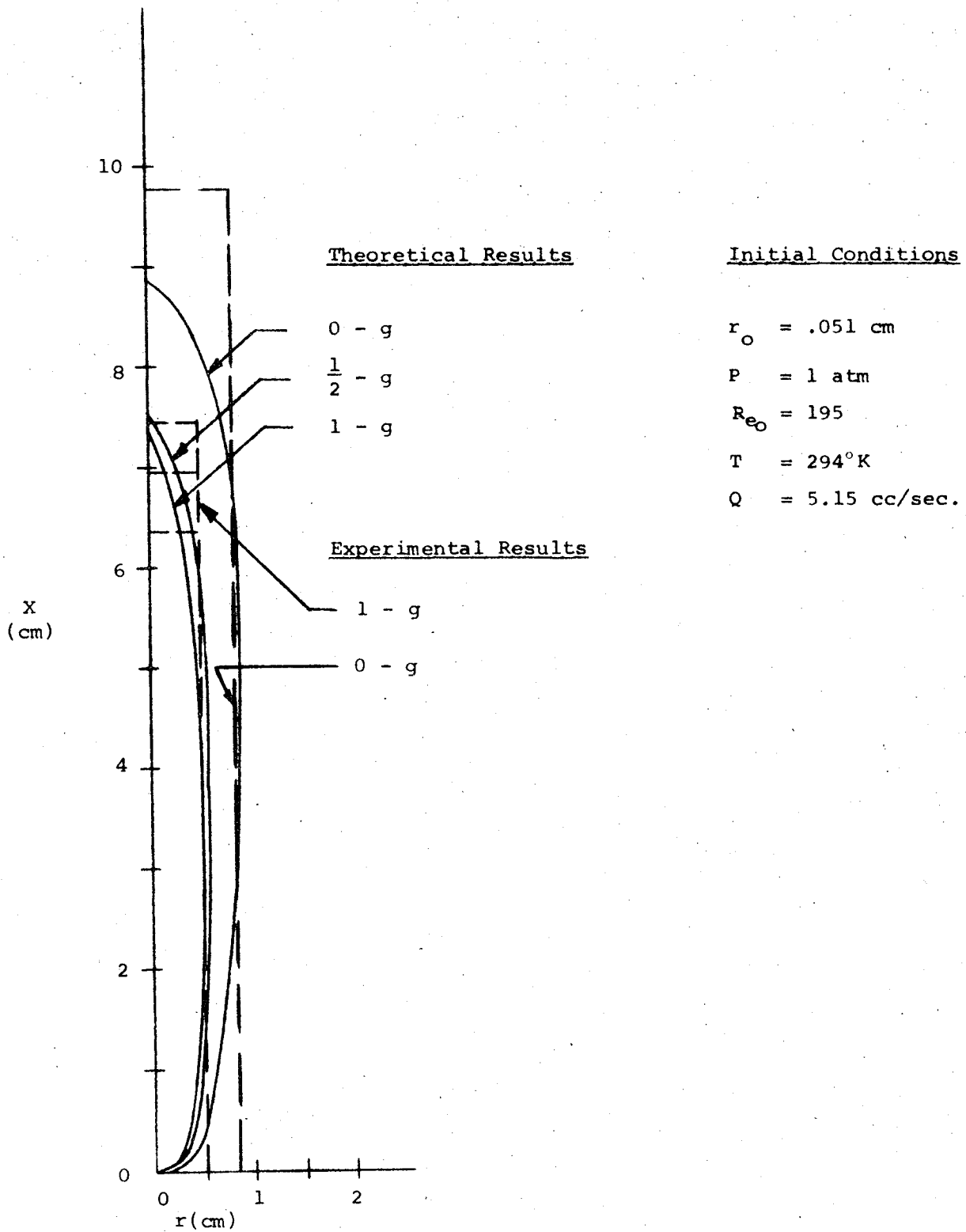
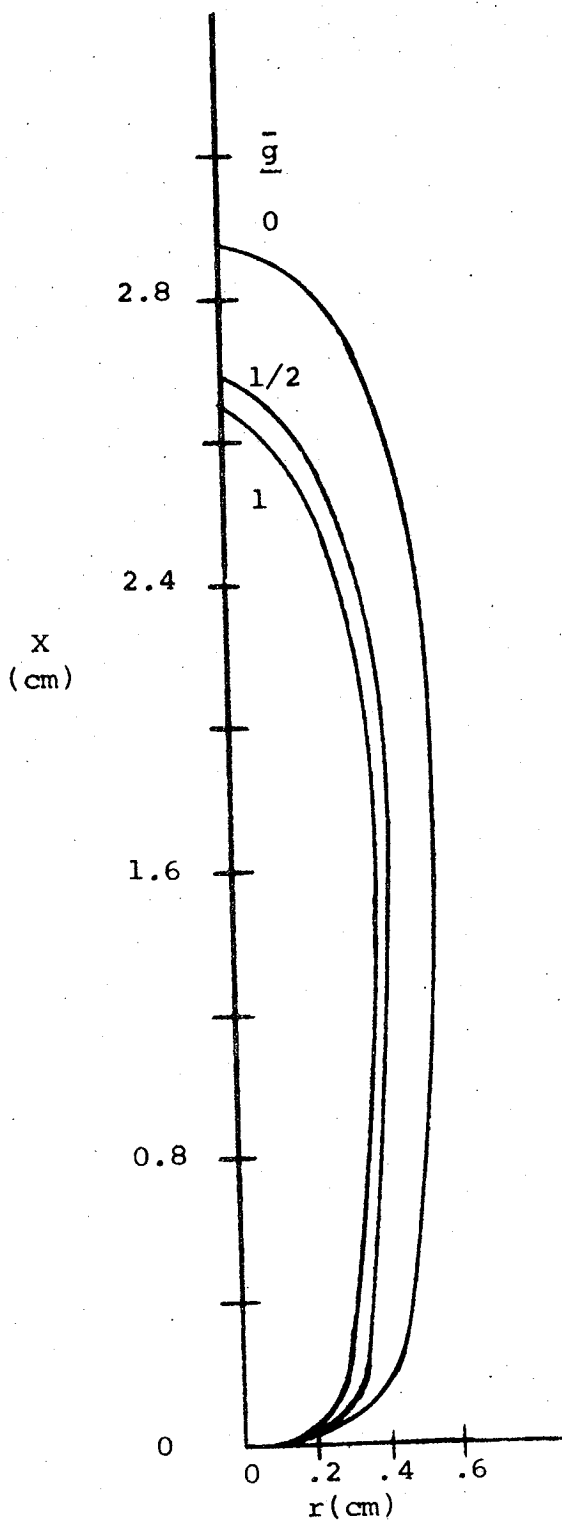


Figure 34. - Methane-air evaluation case-effect of gravity upon theoretical flame shape.



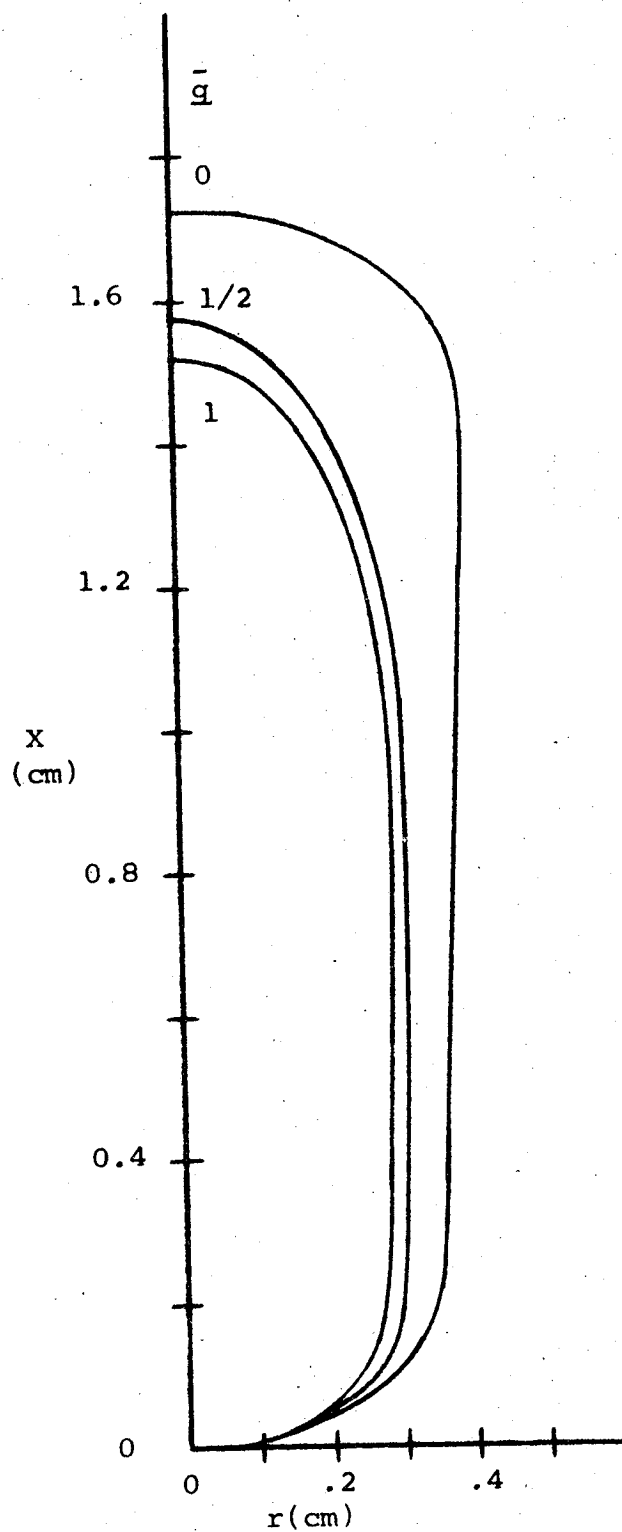
Initial Conditions

$$r_o = .051 \text{ cm} \quad P = 1 \text{ atm}$$

$$Re_o = 195 \quad T = 294^\circ \text{K}$$

$$Q = 5.15 \text{ cc/sec.}$$

Figure 35. - Methane-50% oxygen evaluation case-effect of gravity upon theoretical flame shape.



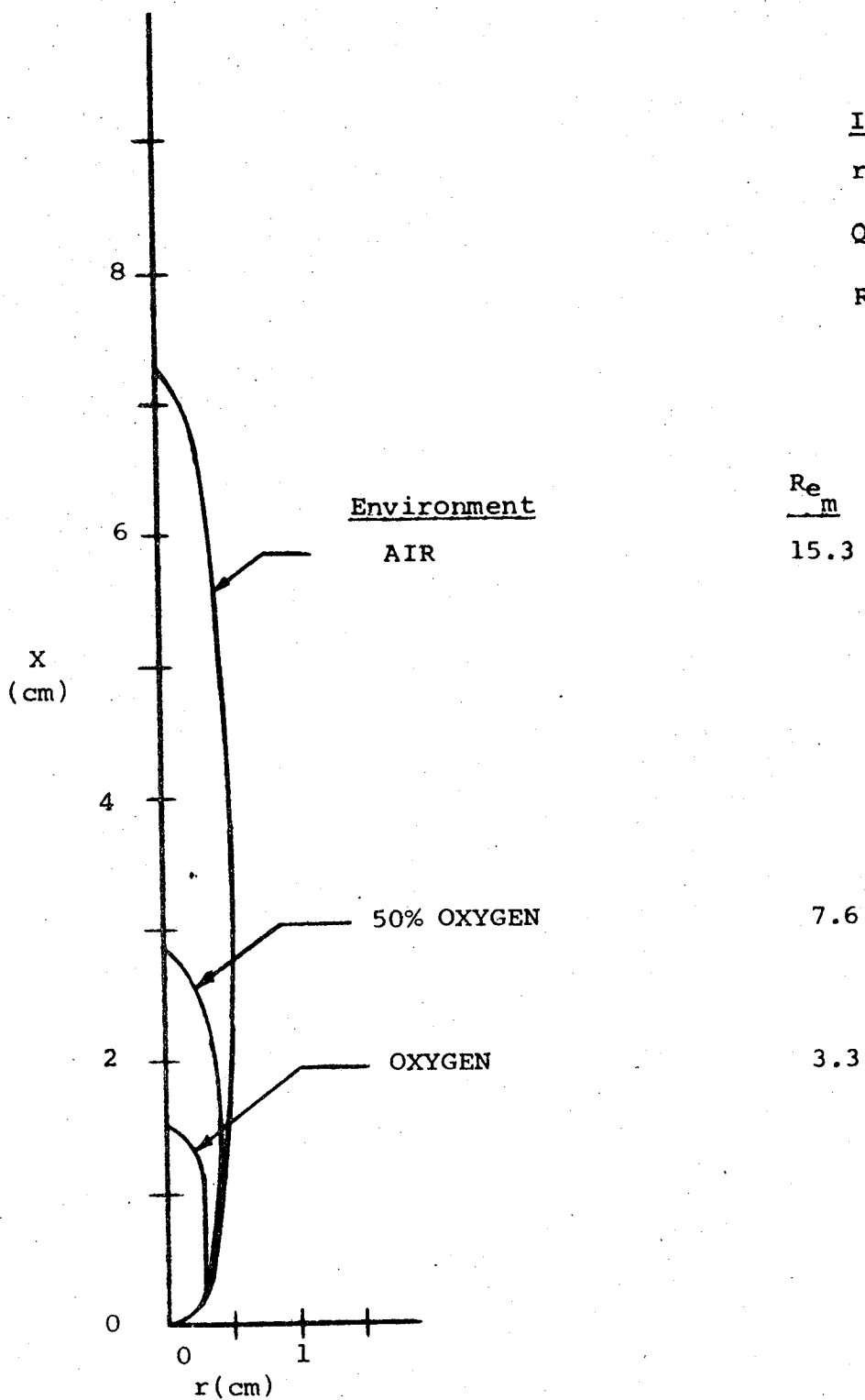
Initial Conditions

$$r_o = .051 \text{ cm} \quad P = 1 \text{ atm}$$

$$Re_o = 195 \quad T = 294^\circ \text{K}$$

$$Q = 5.15 \text{ cc/sec.}$$

Figure 36. - Methane-oxygen evaluation case-effect of gravity upon theoretical flame shape.



Initial Conditions

$r_o = .051$ cm $P = 1$ atm

$Q = 5.15$ cc/sec $T = 294^\circ K$

$Re_o = 195$

Re_m

15.3

7.6

3.3

Figure 37. - Normal gravity methane flame evaluation cases - effect of environment upon theoretical flame shape.

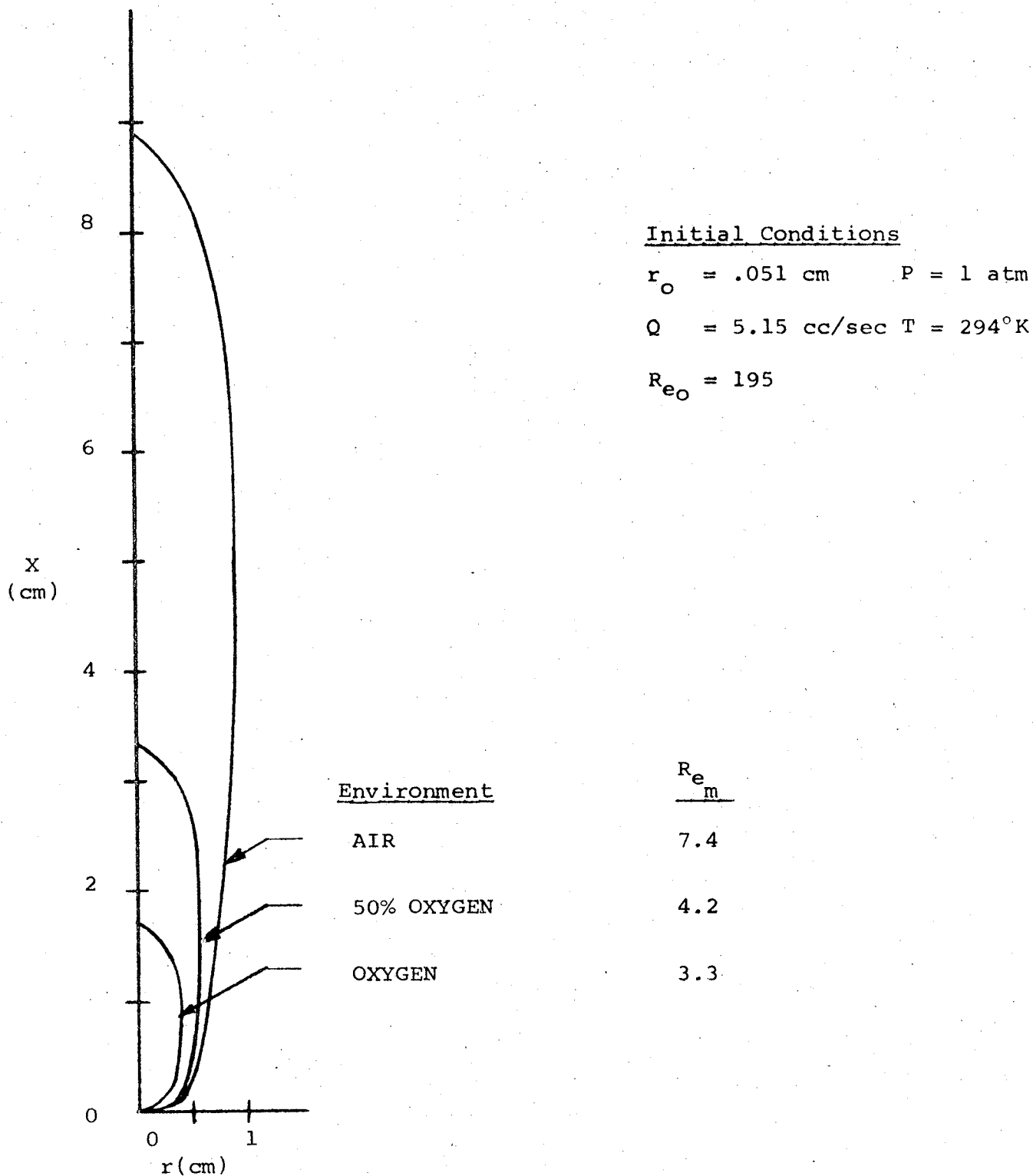


Figure 38. - Zero gravity methane flame evaluation cases - effect of environment upon theoretical flame shape.

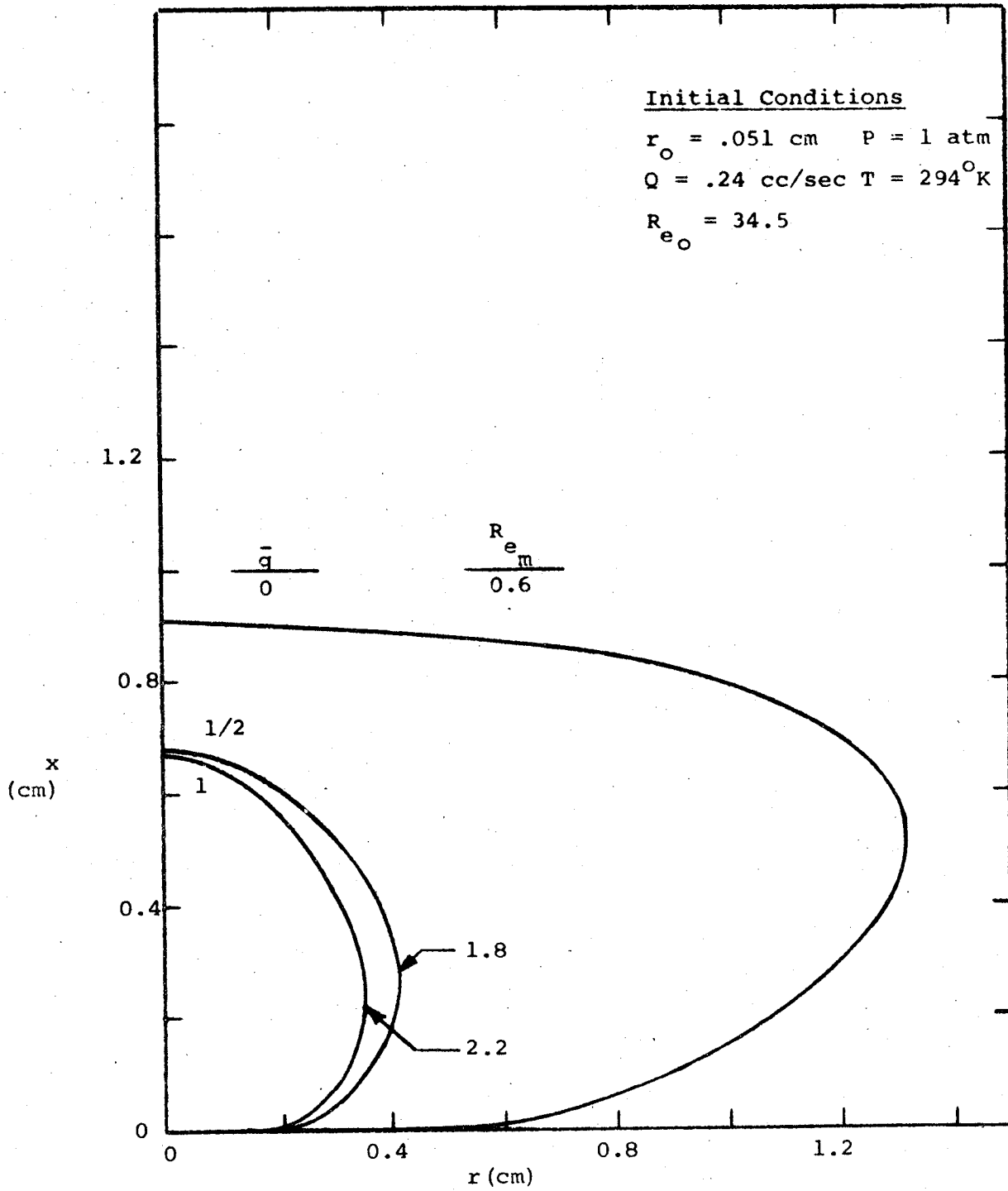


Figure 39. - Propylene-air evaluation case-effect of gravity upon theoretical flame shape.

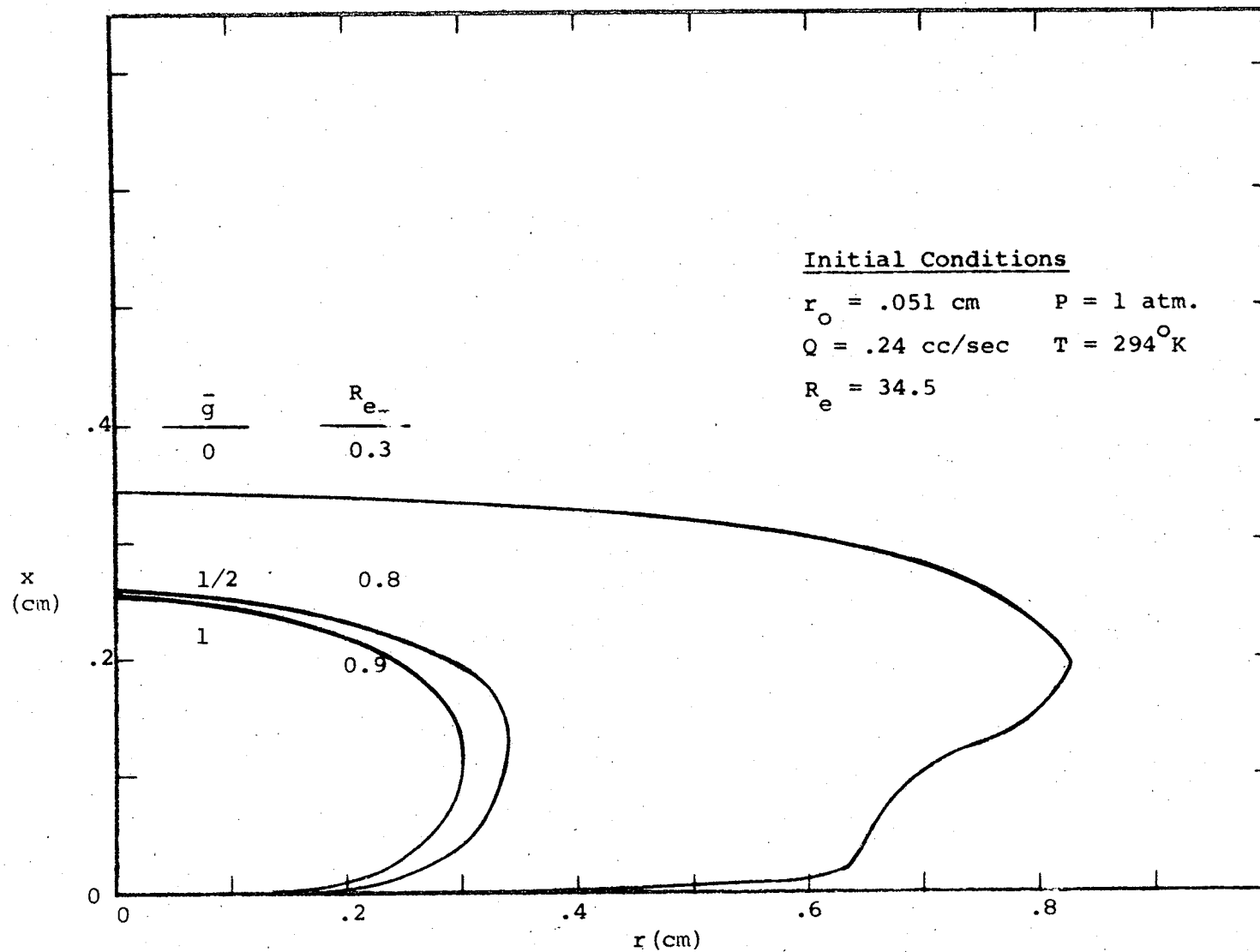


Figure 40. - Propylene-50% oxygen evaluation case-effect of gravity upon theoretical flame shape.

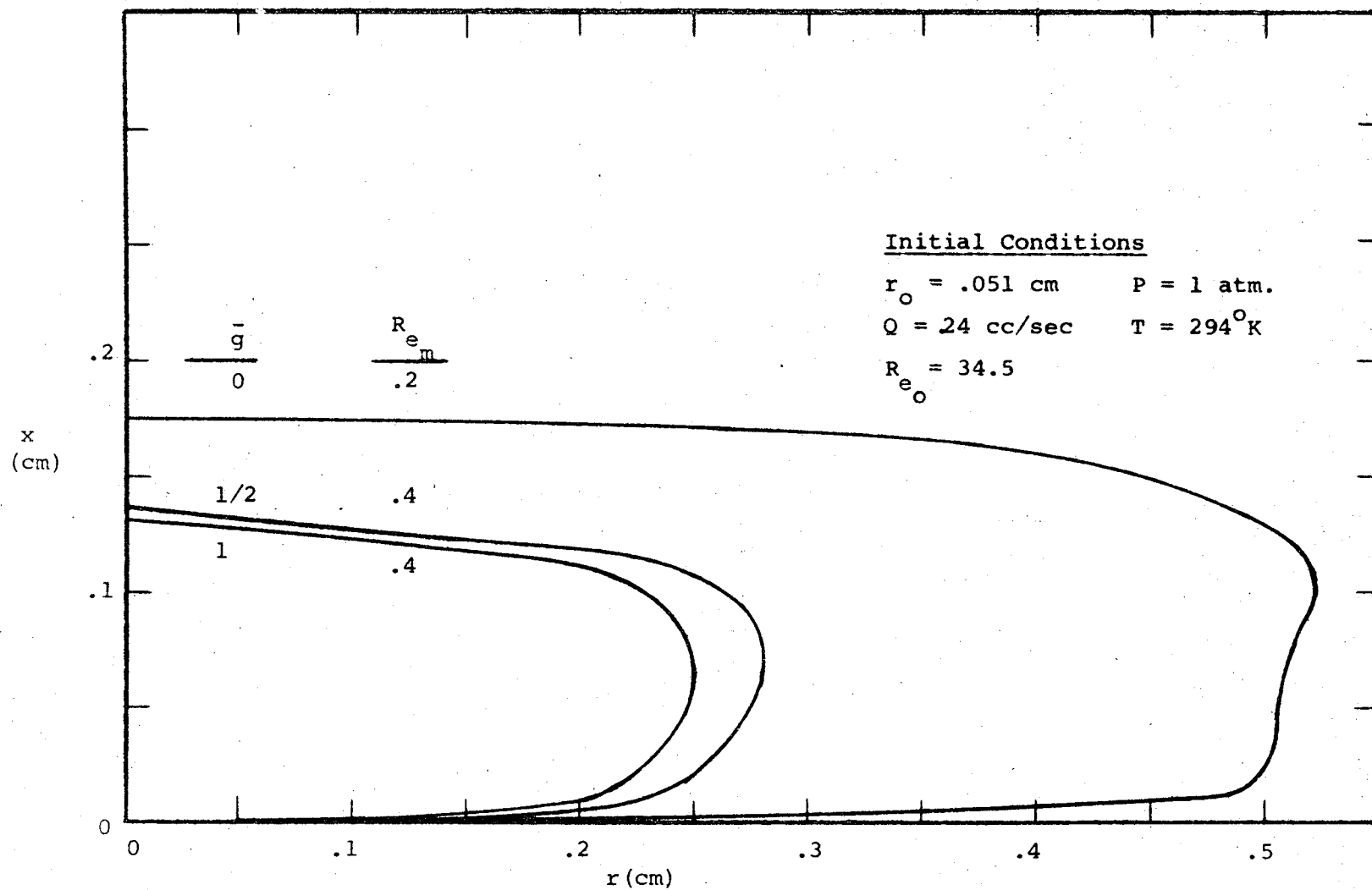


Figure 41. - Propylene-oxygen evaluation case-effect of gravity upon theoretical flame shape.

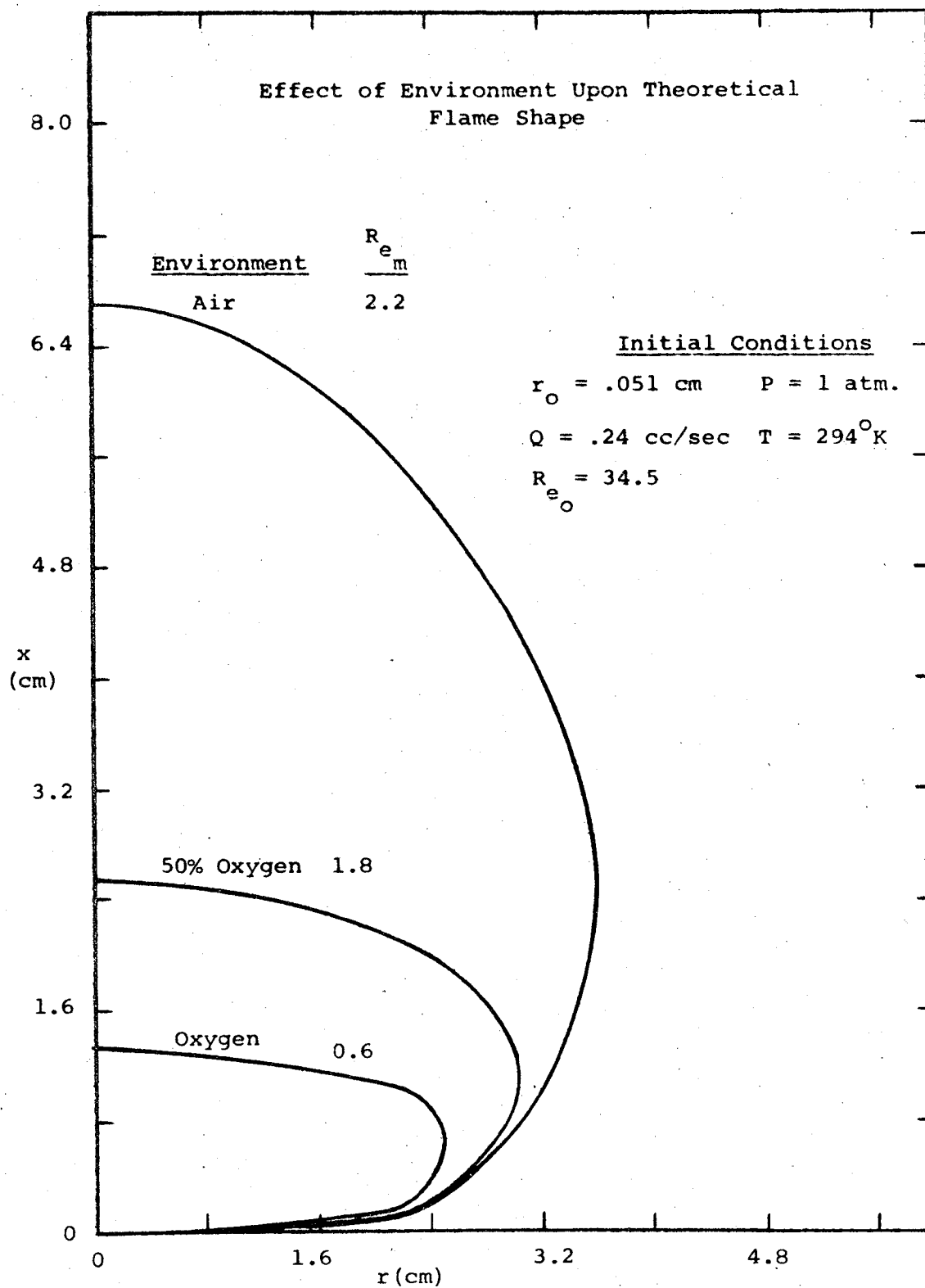


Figure 42. - Normal gravity propylene flame evaluation case.

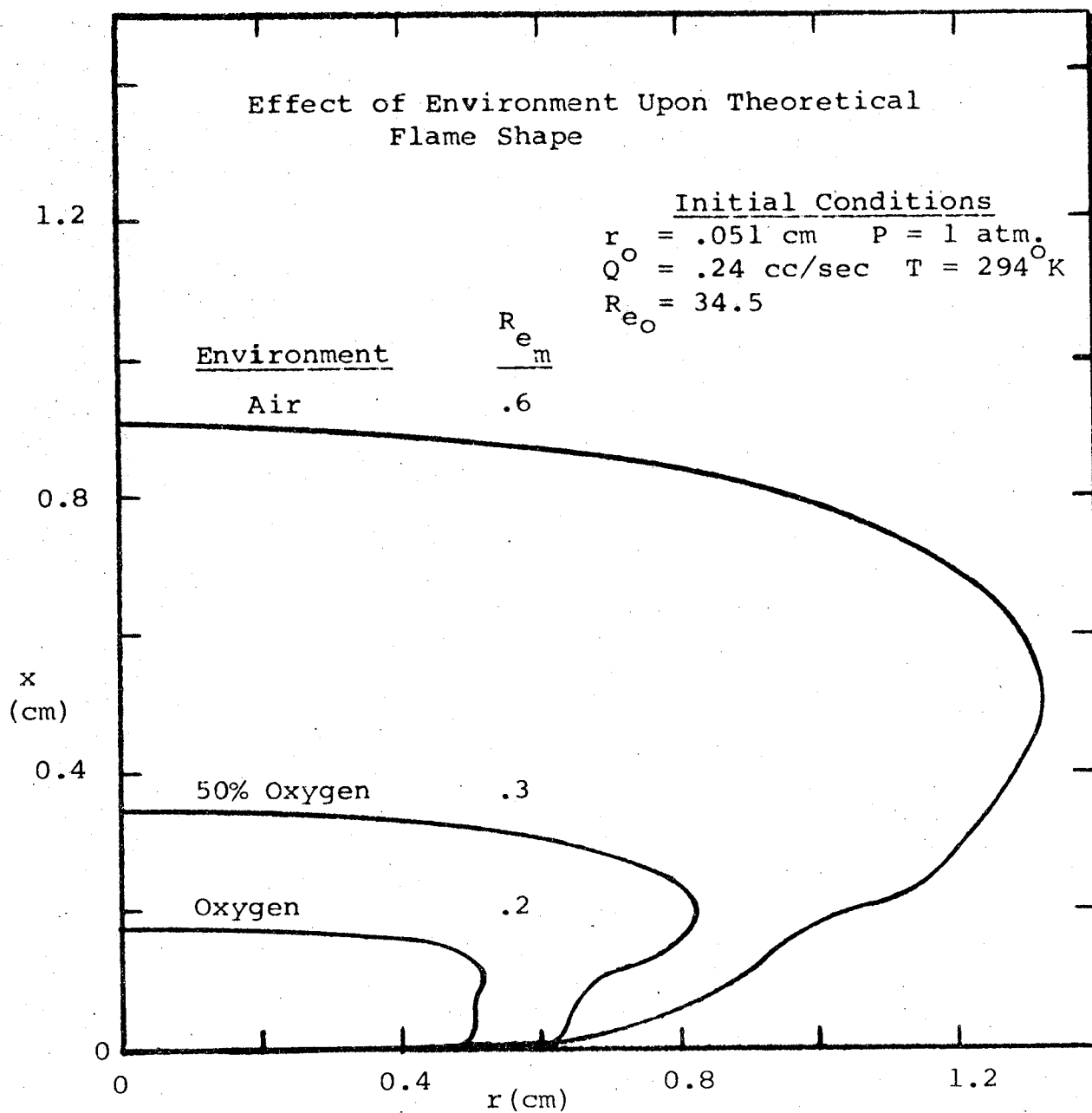


Figure 43. - Zero gravity propylene flame evaluation case.

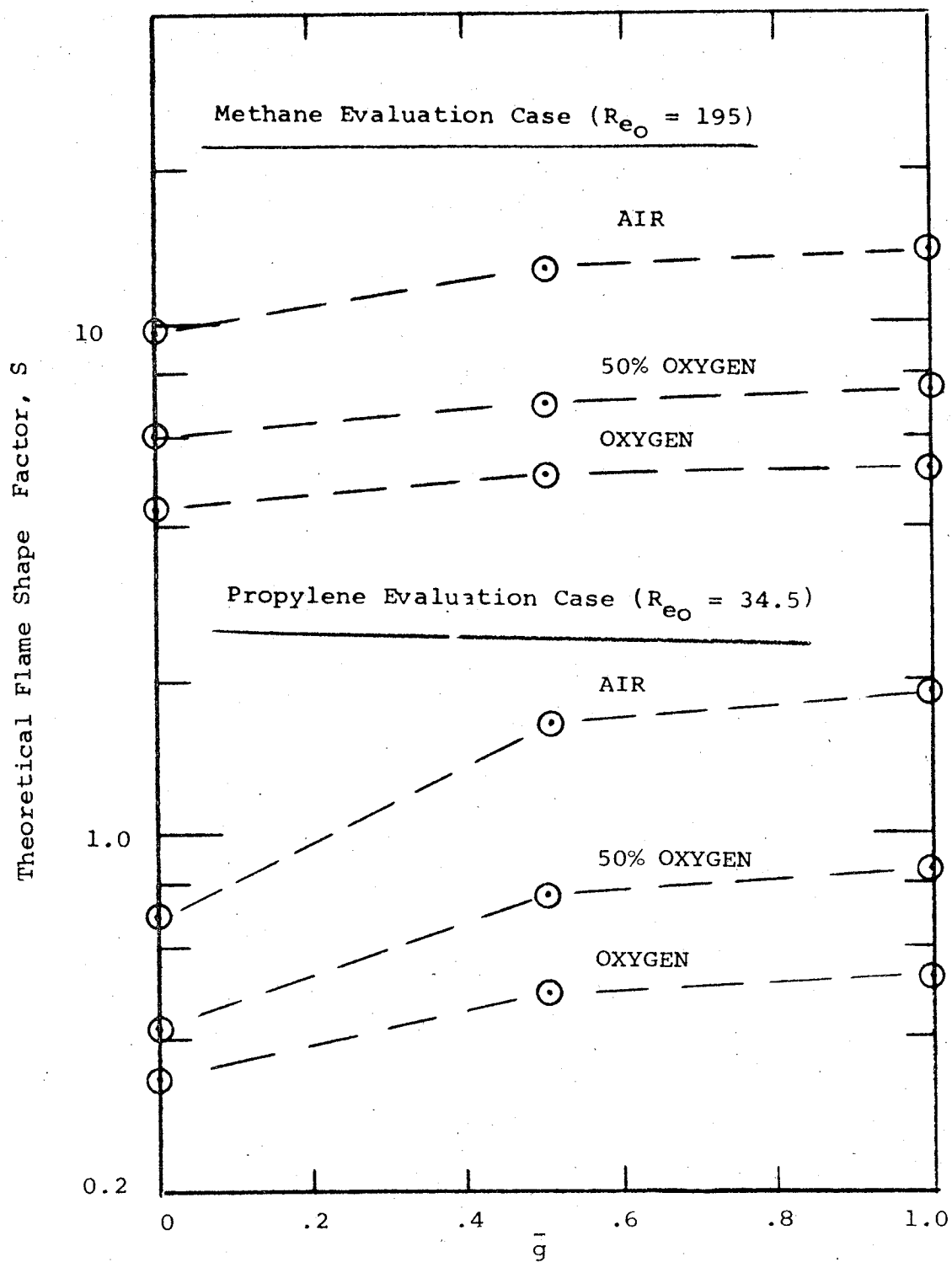


Figure 44. - Effect of fuel and environment composition upon flame shape.

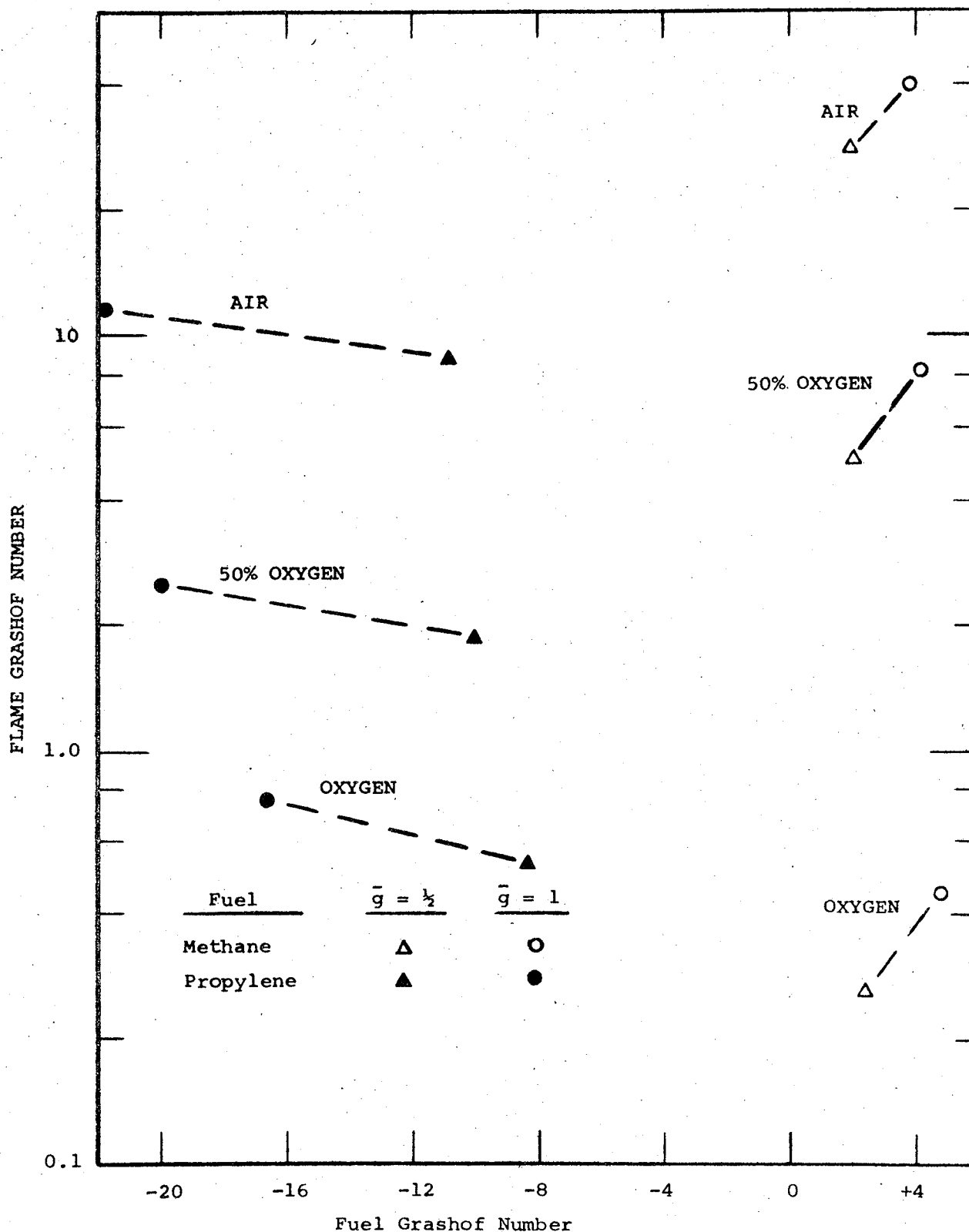


Figure 45. - Comparison of fuel Grashof number vs theoretical flame Grashof number.

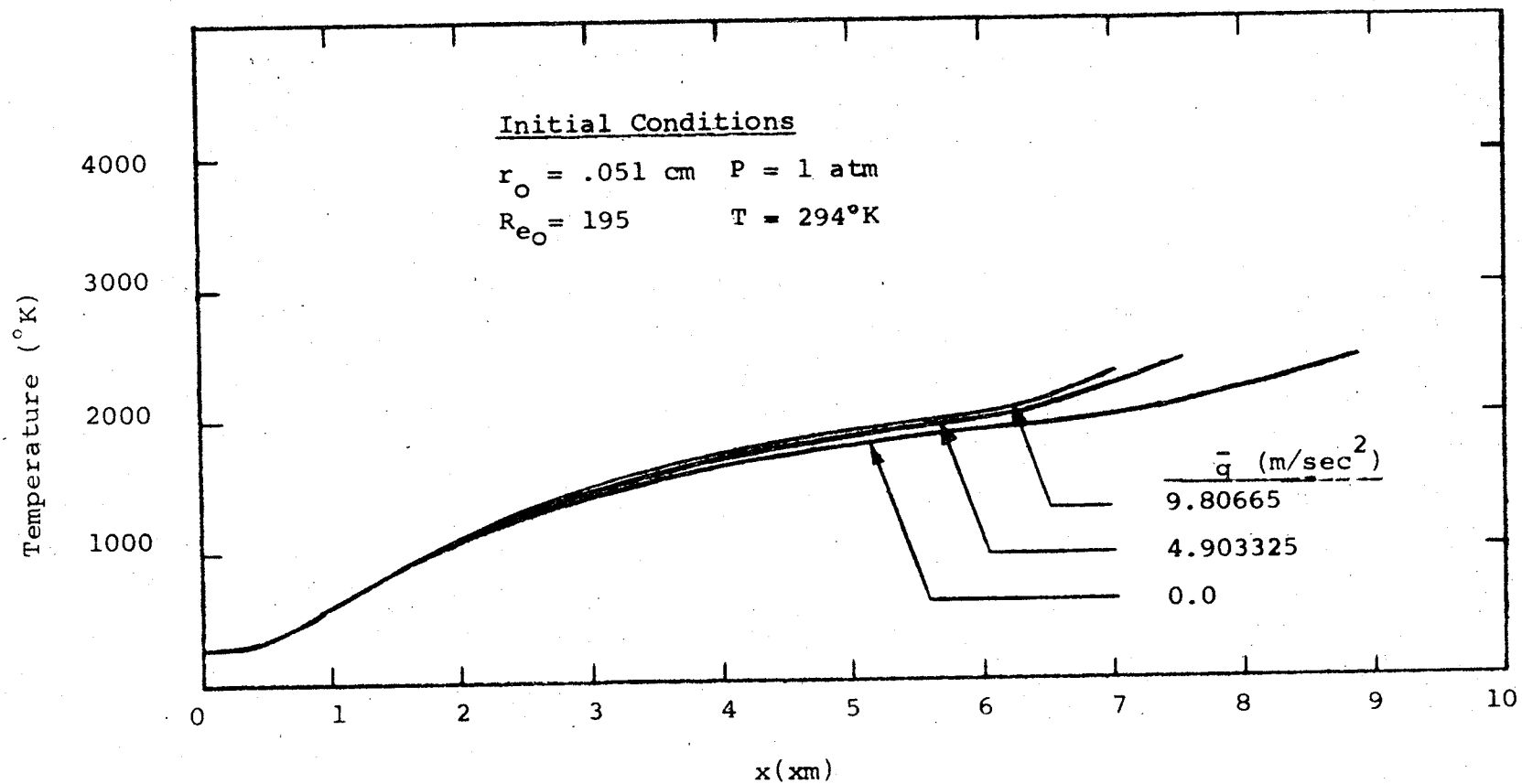


Figure 46. - Centerline temperature as a function of gravity level for methane in an air environment.

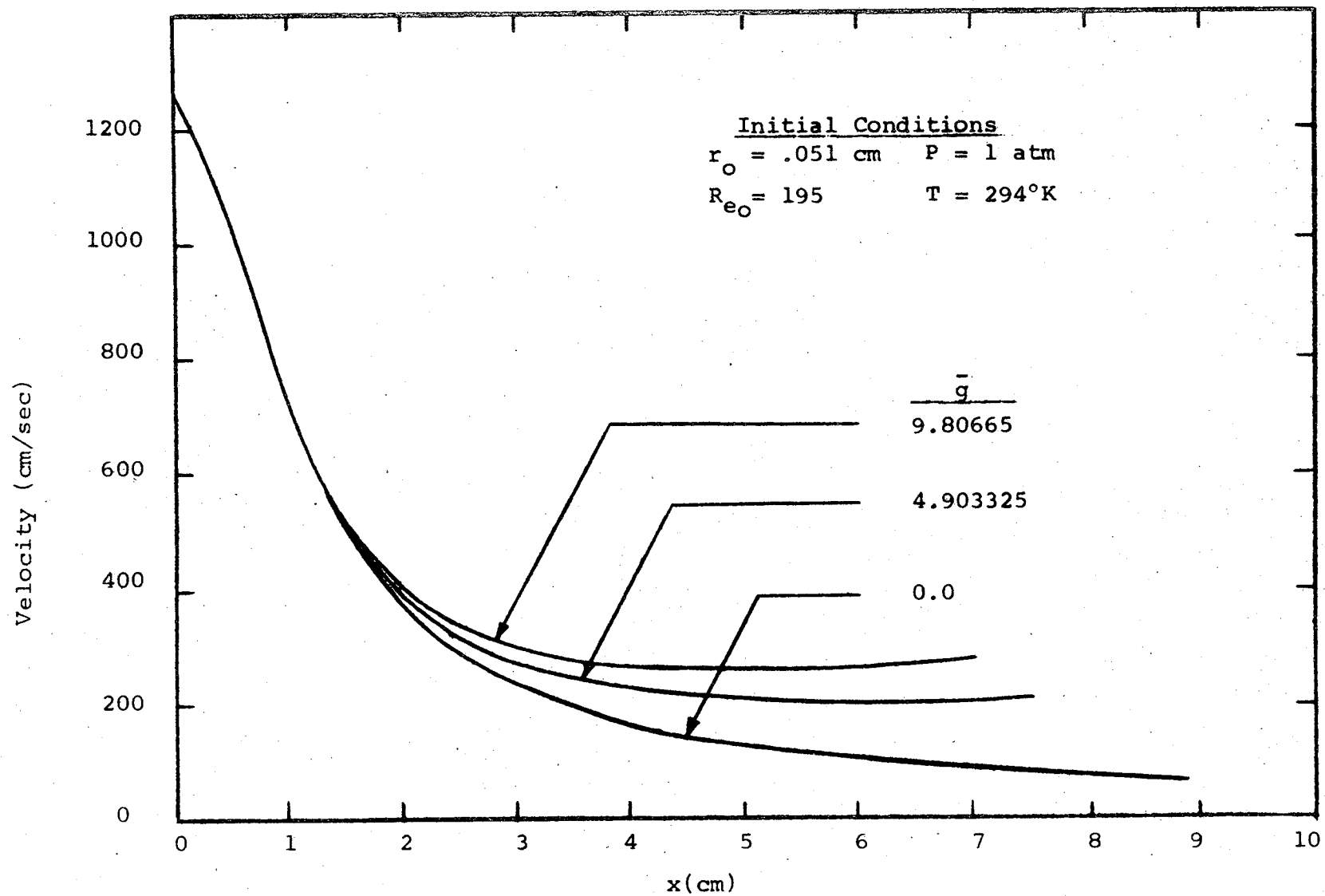


Figure 47. - Centerline velocity as a function of gravity level for methane in an air environment.

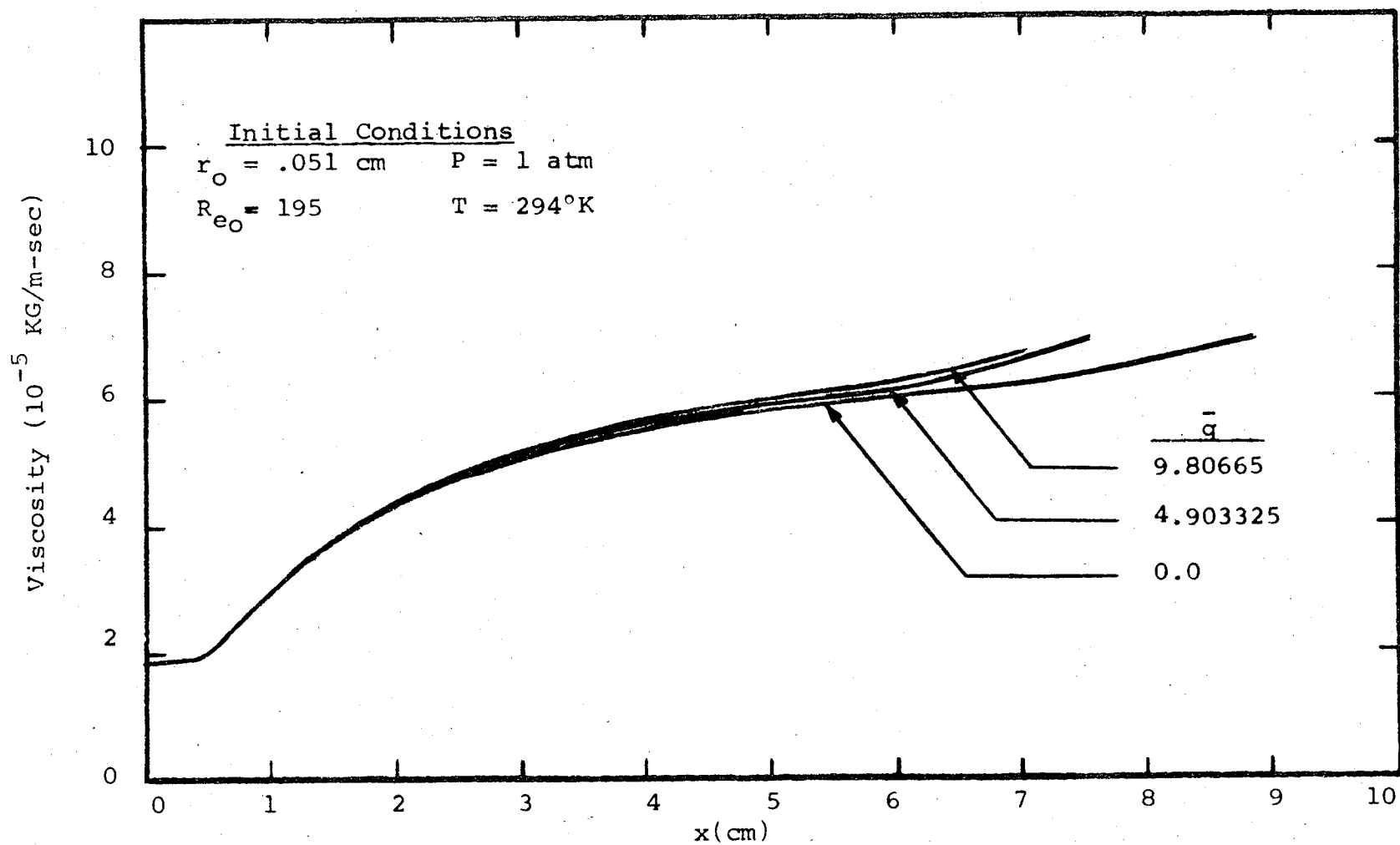


Figure 48. - Centerline viscosity as a function of gravity level for methane in an air environment.

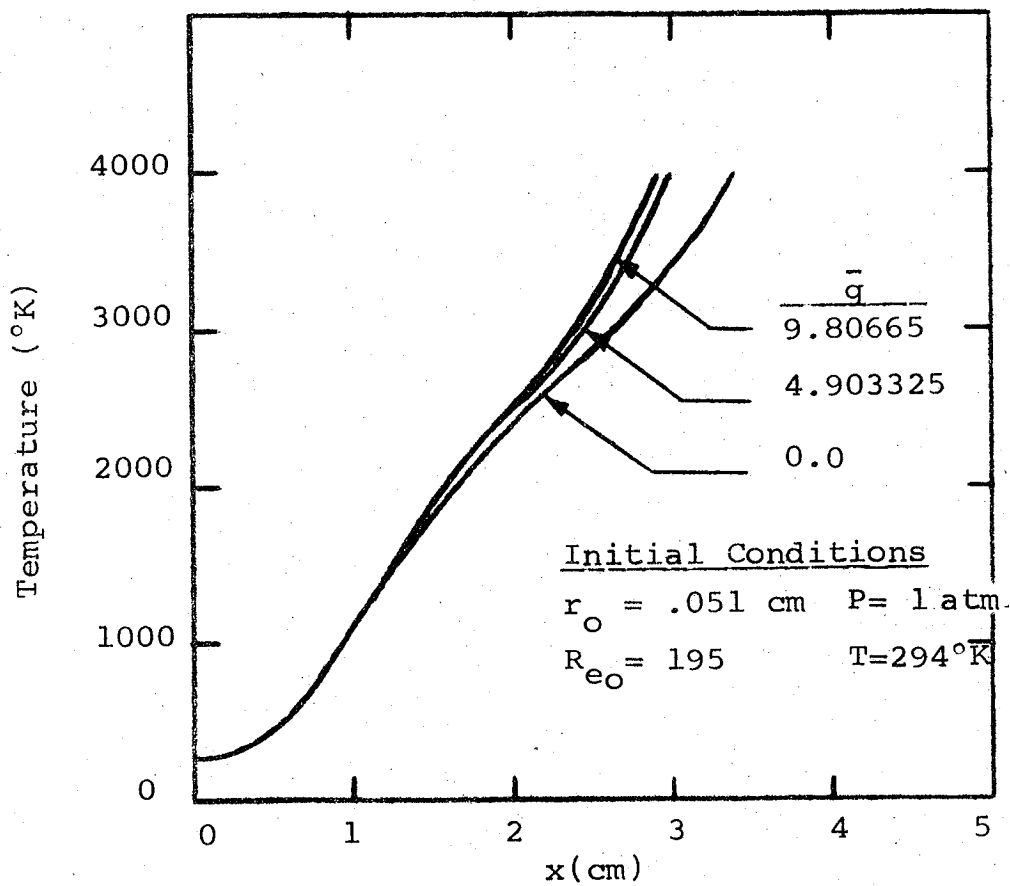


Figure 49. - Centerline temperature as a function of gravity level for methane in a 50% oxygen-50% nitrogen environment.

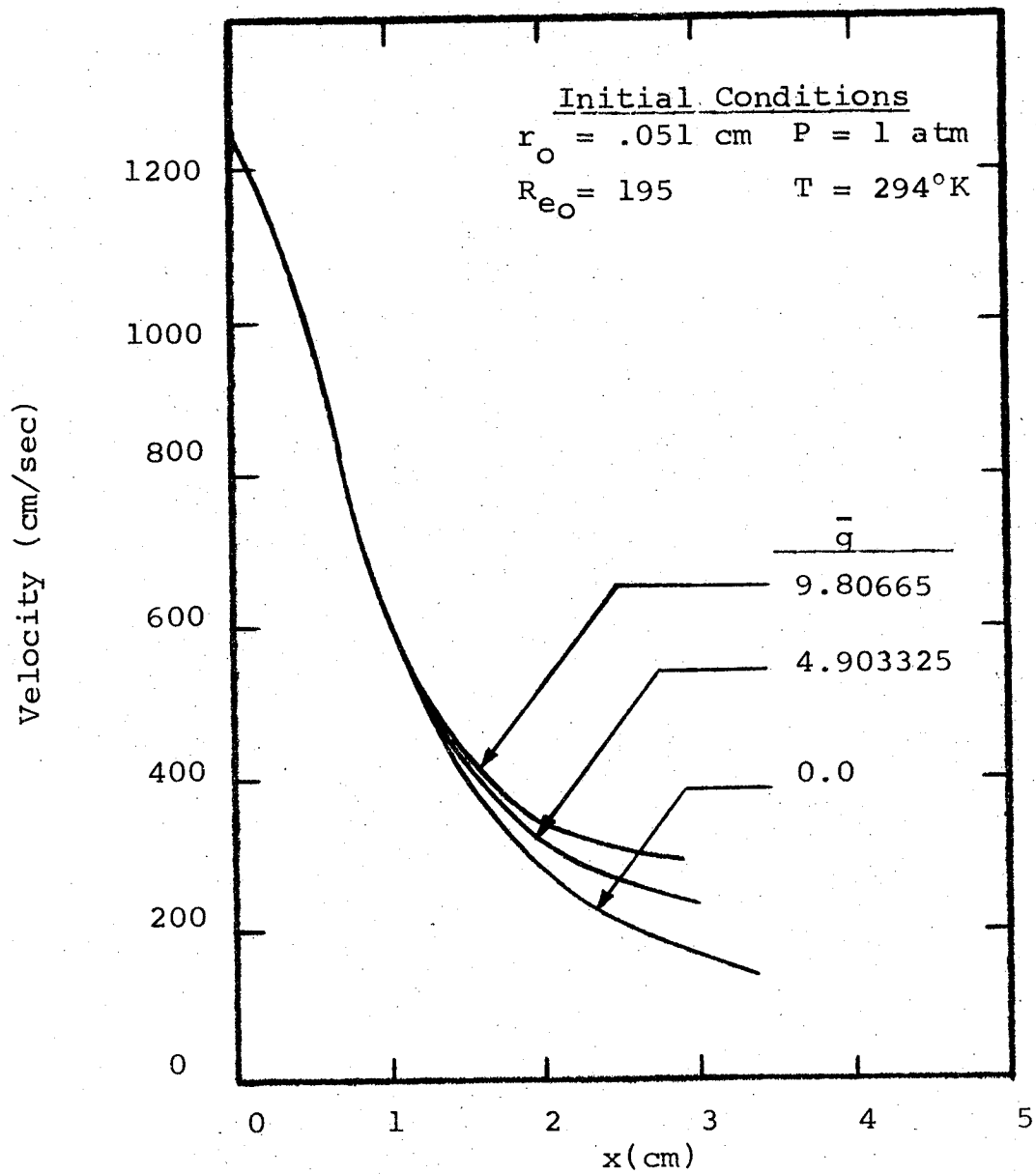


Figure 50. - Centerline velocity as a function of gravity level for methane in a 50% oxygen-50% nitrogen environment.

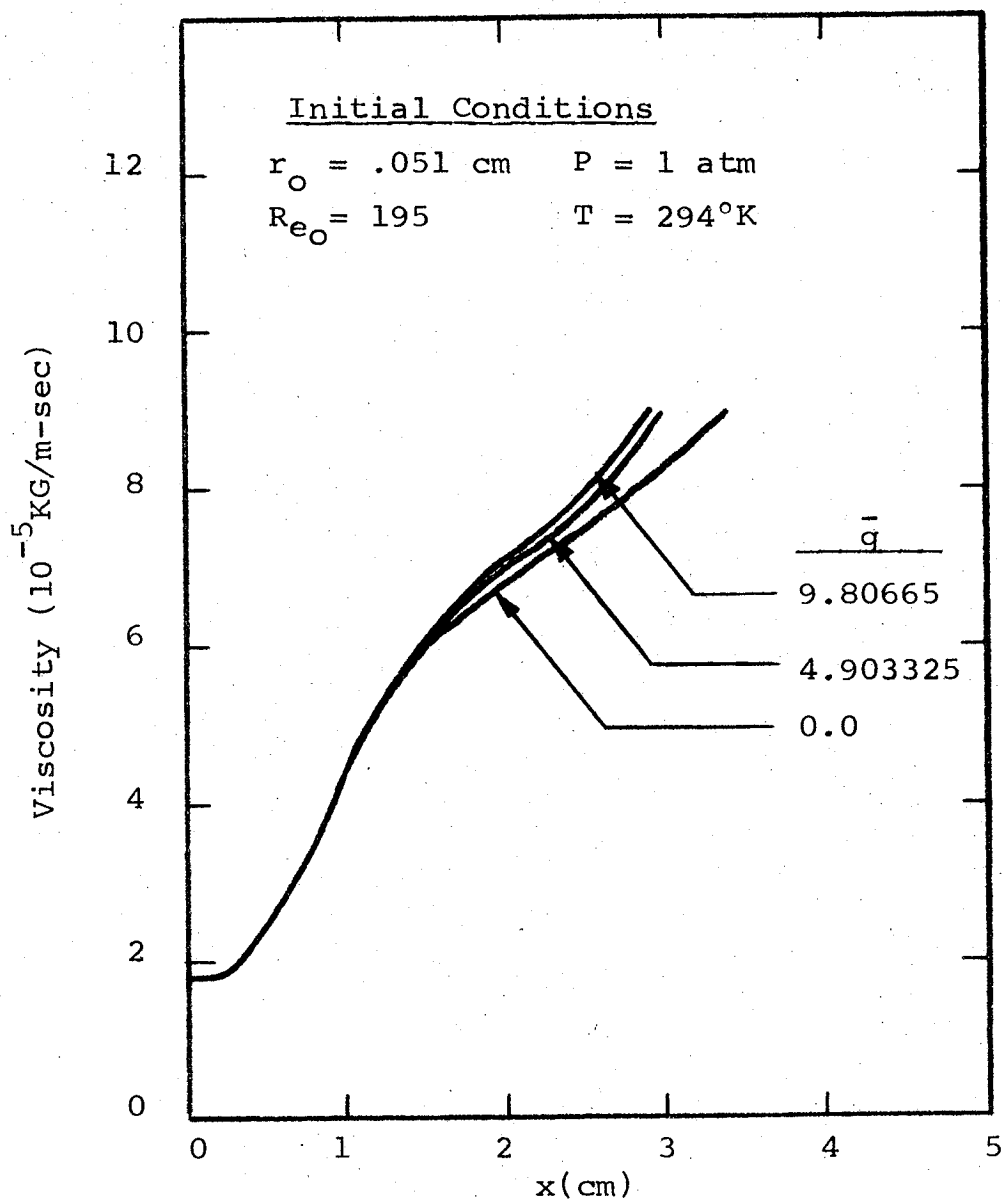


Figure 51. - Centerline viscosity as a function of gravity level for methane in a 50% oxygen-50% nitrogen environment.

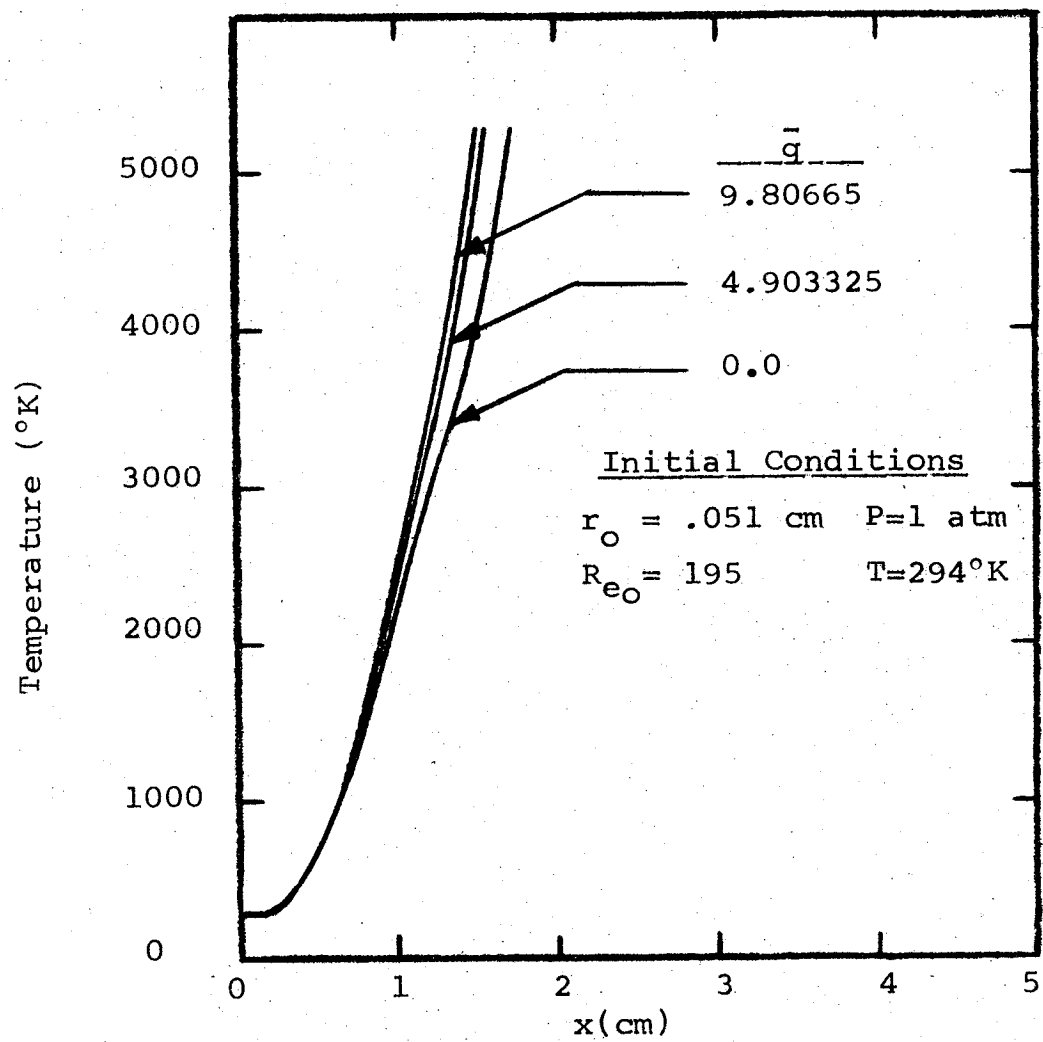


Figure 52. - Centerline temperature as a function of gravity level for methane in an oxygen environment.

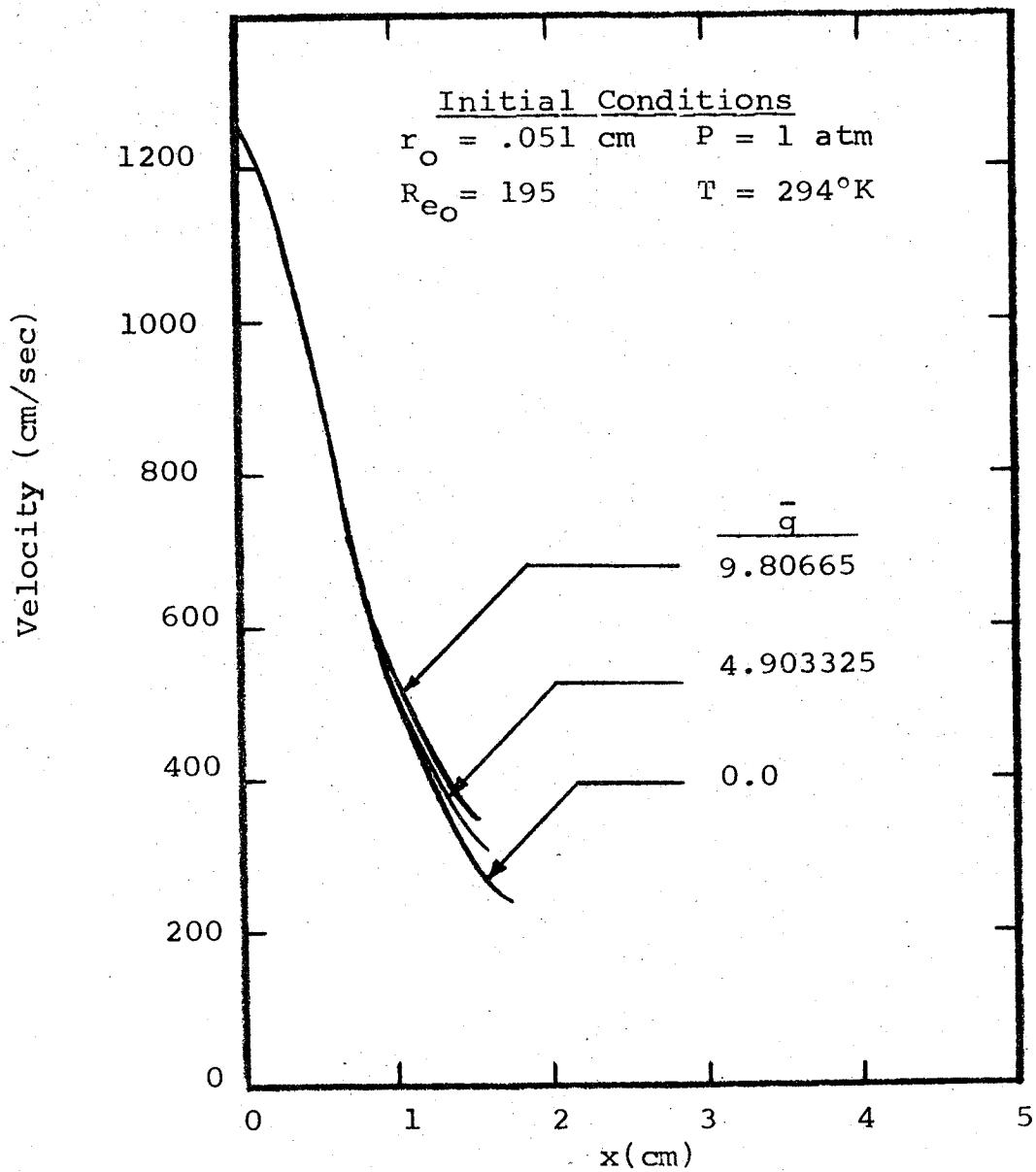


Figure 53. - Centerline velocity as a function of gravity level for methane in an oxygen environment.

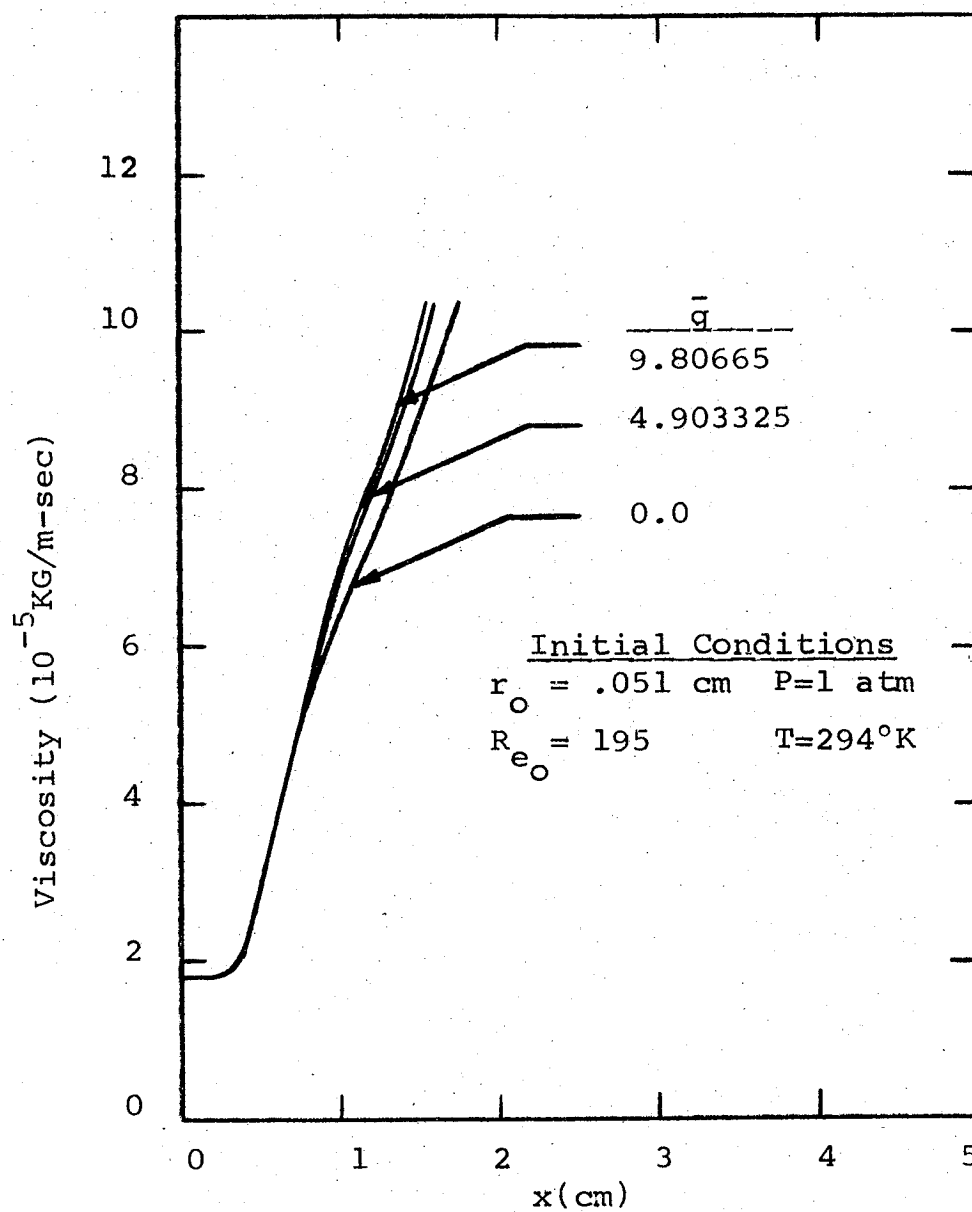


Figure 54. - Centerline viscosity as a function of gravity level for methane in an oxygen environment.

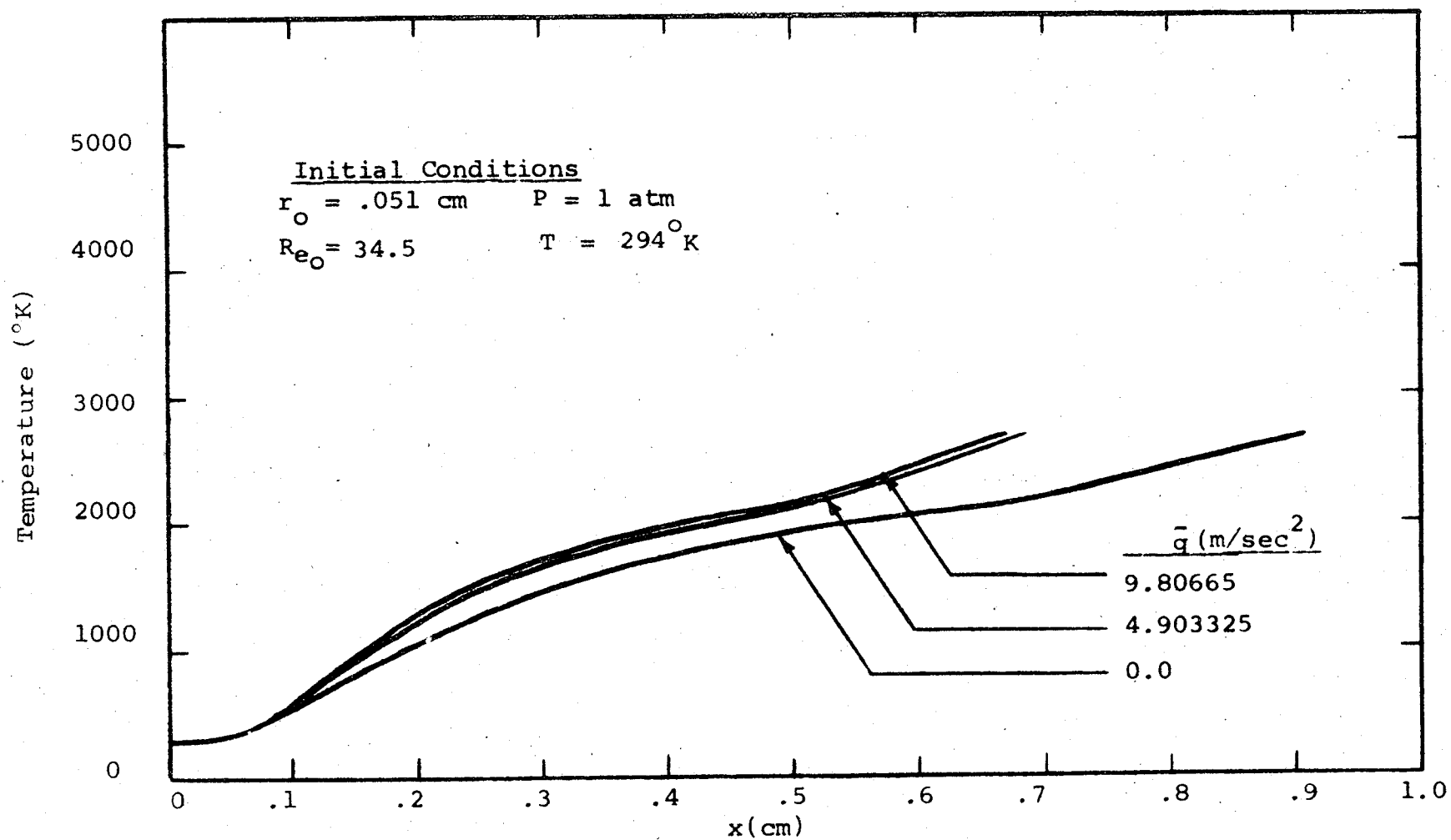


Figure 55. - Centerline temperature as a function of gravity level for propylene in an air environment.

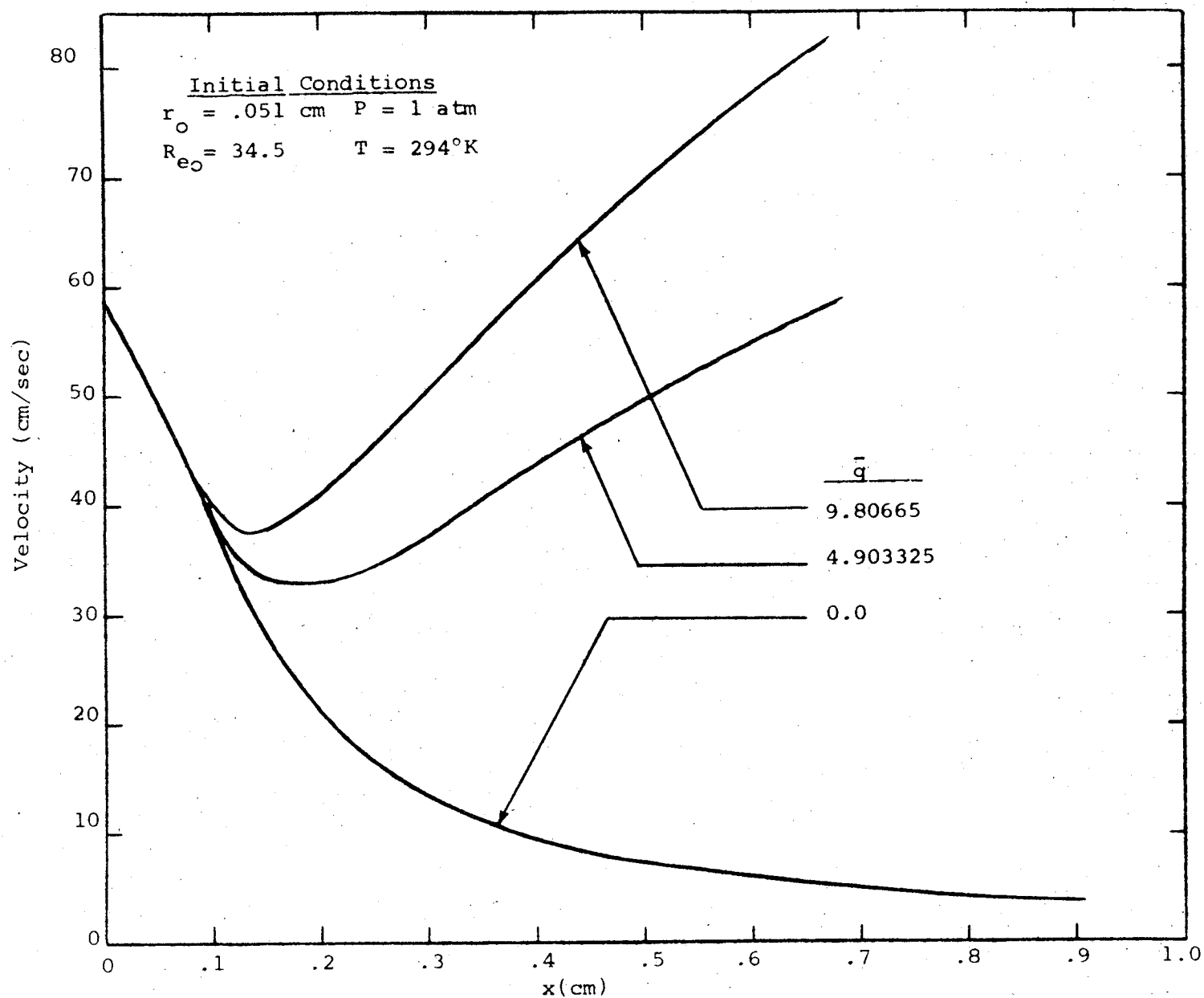


Figure 56. - Centerline velocity as a function of gravity level for propylene in an air environment.

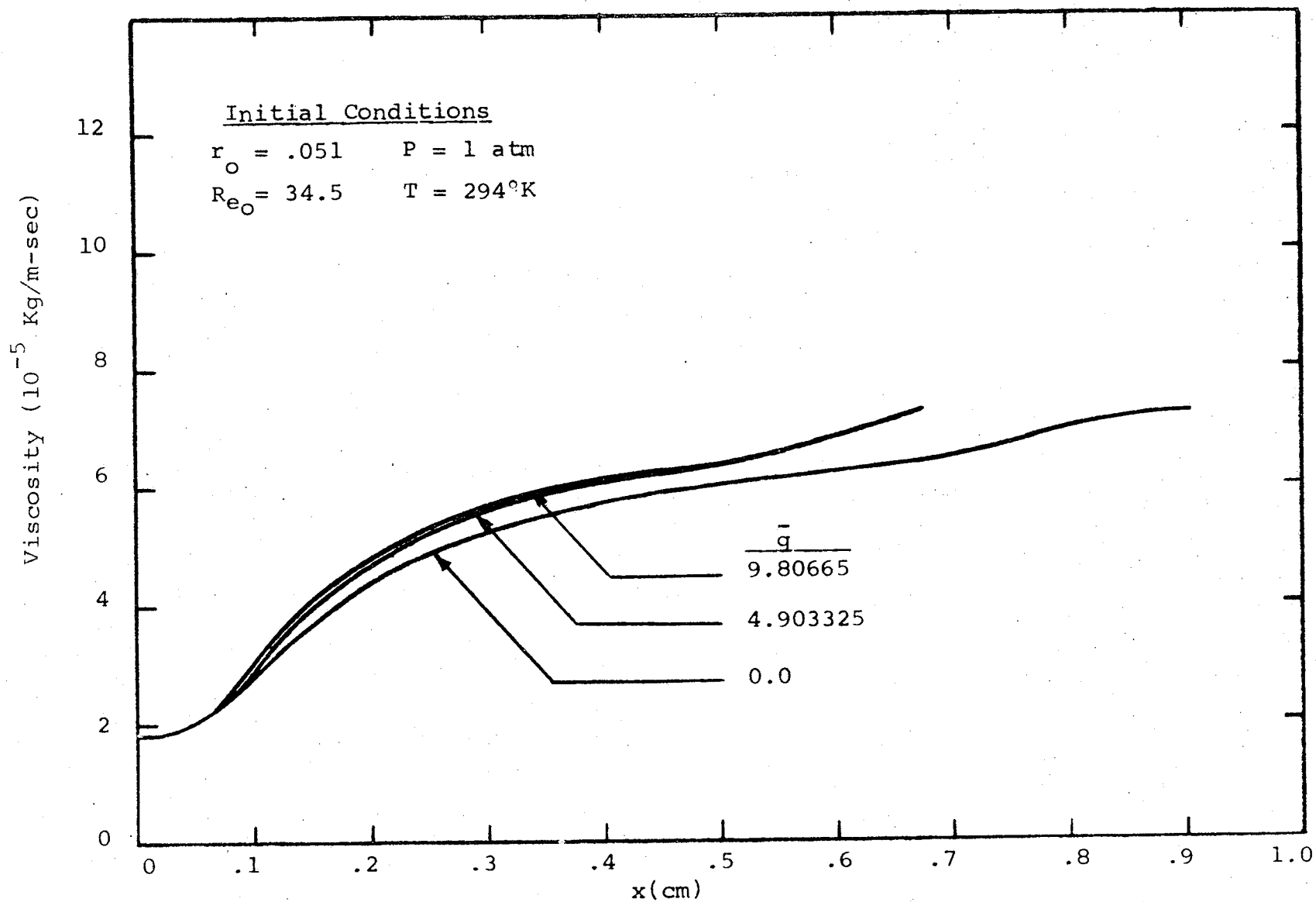


Figure 57. - Centerline viscosity as a function of gravity level for propylene in an air environment.

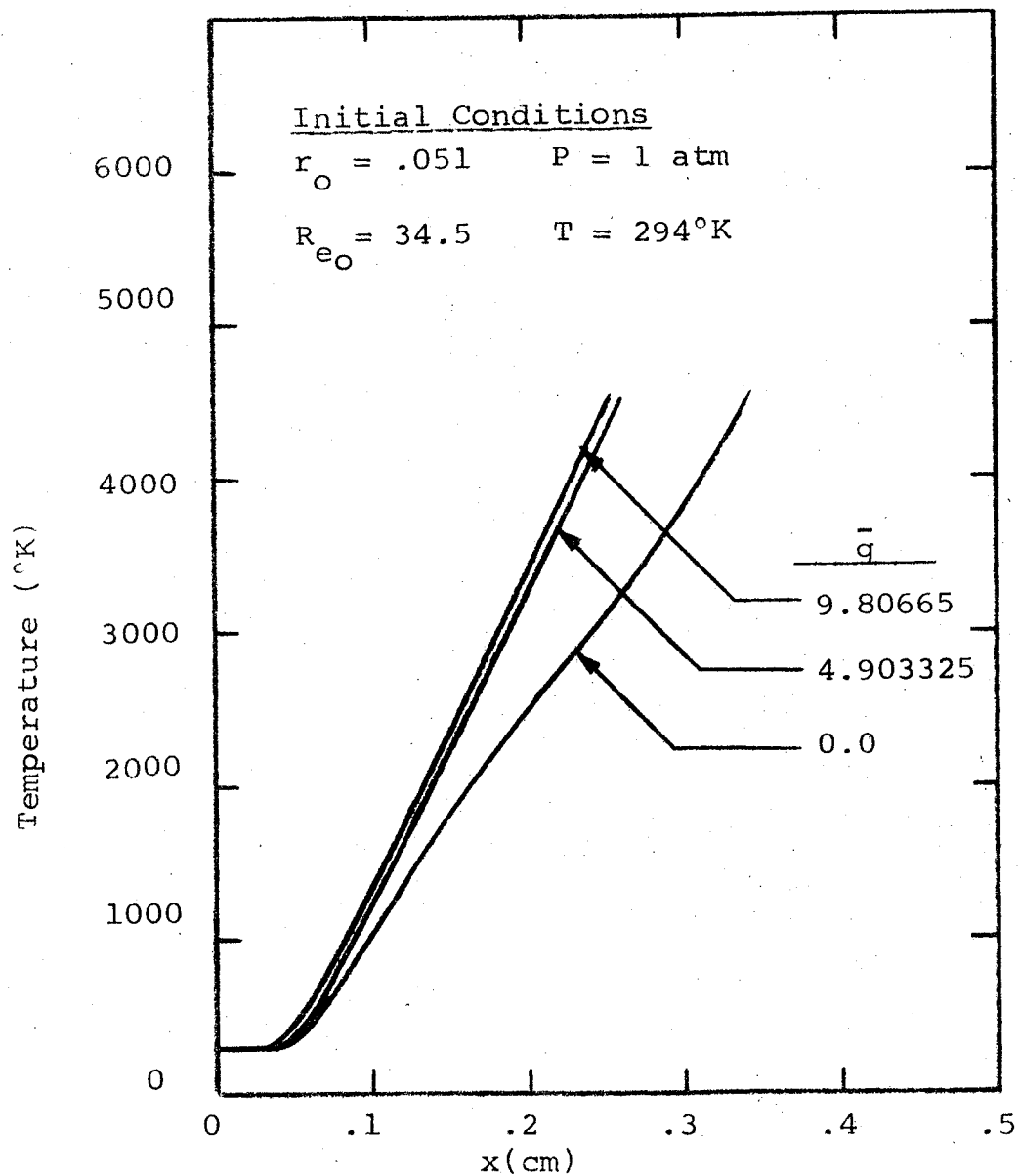


Figure 58. - Centerline temperature as a function of gravity level for propylene in a 50% oxygen-50% nitrogen environment

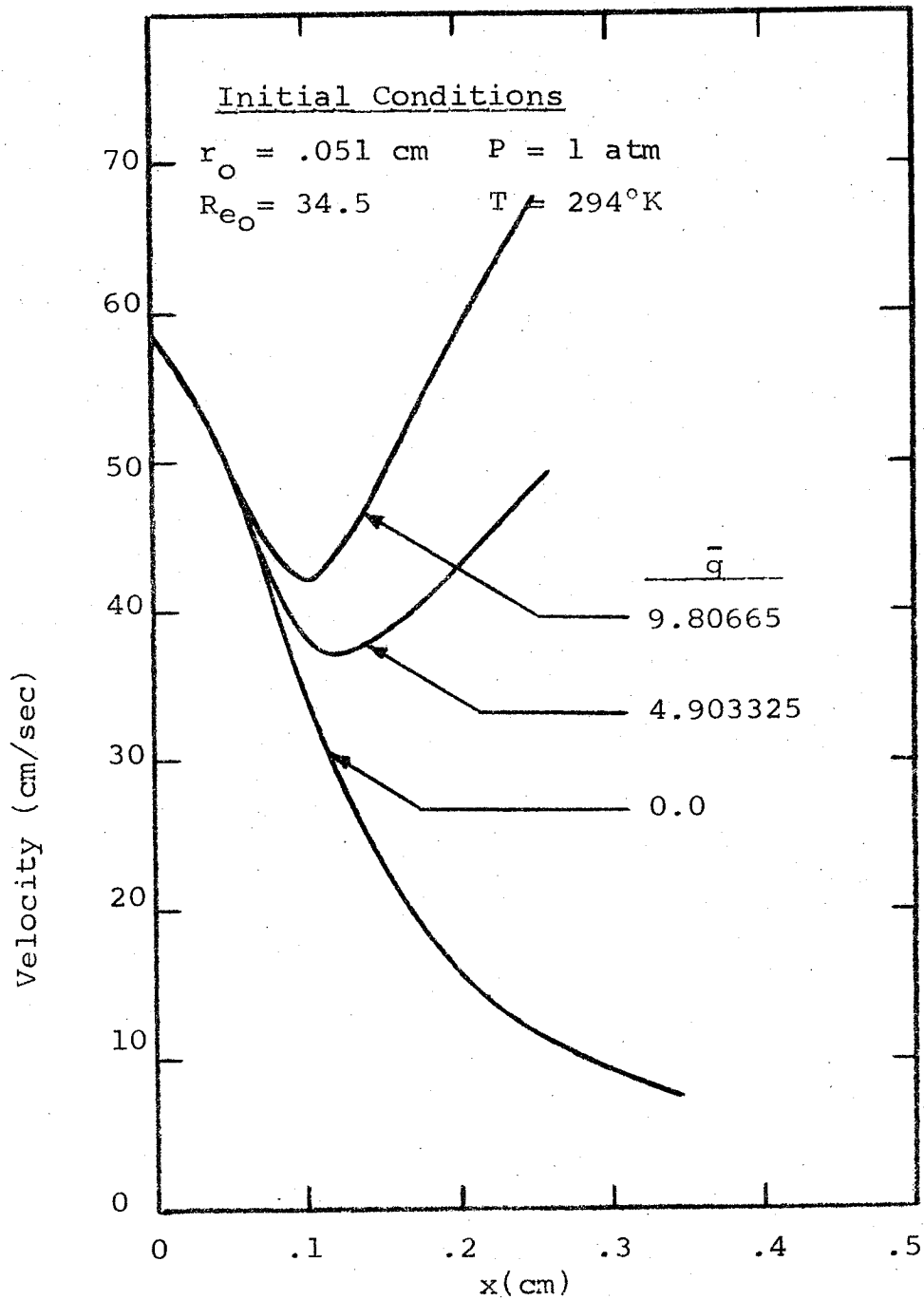


Figure 59. - Centerline velocity as a function of gravity level for propylene in a 50% oxygen-50% nitrogen environment.

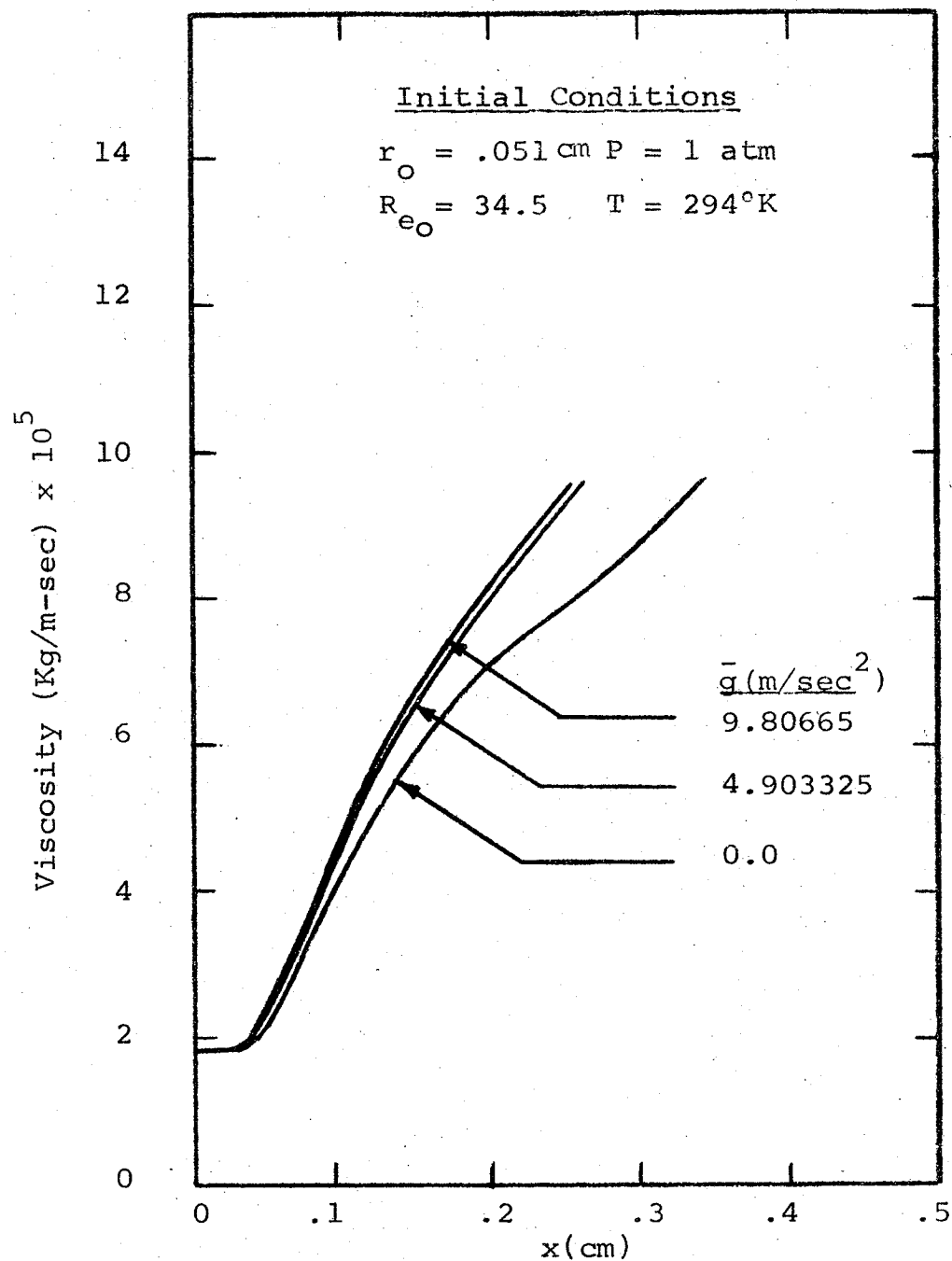


Figure 60. - Centerline viscosity as a function of gravity level for propylene in a 50% oxygen-50% nitrogen environment.

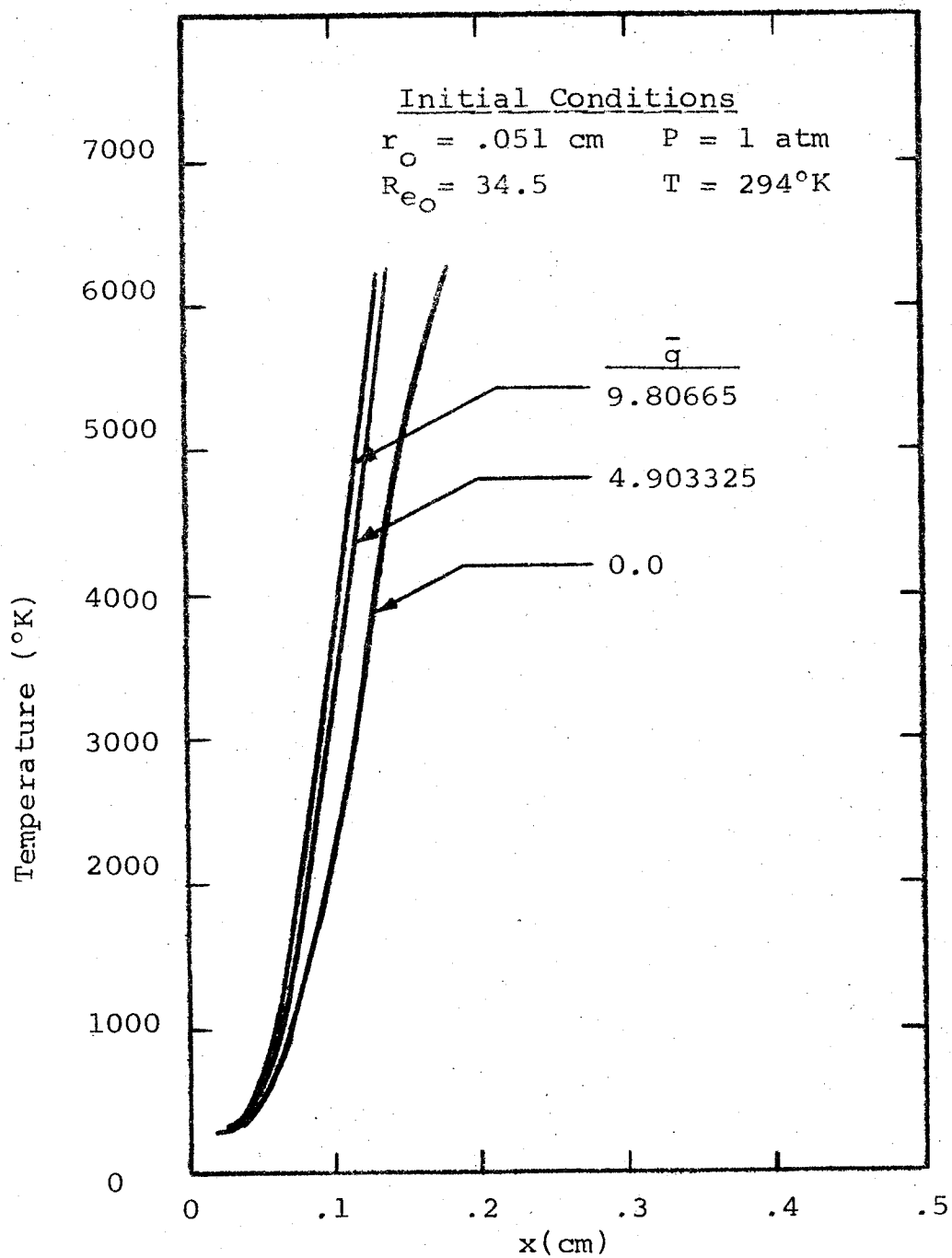


Figure 61. - Centerline temperature as a function of gravity level for propylene in an oxygen environment.

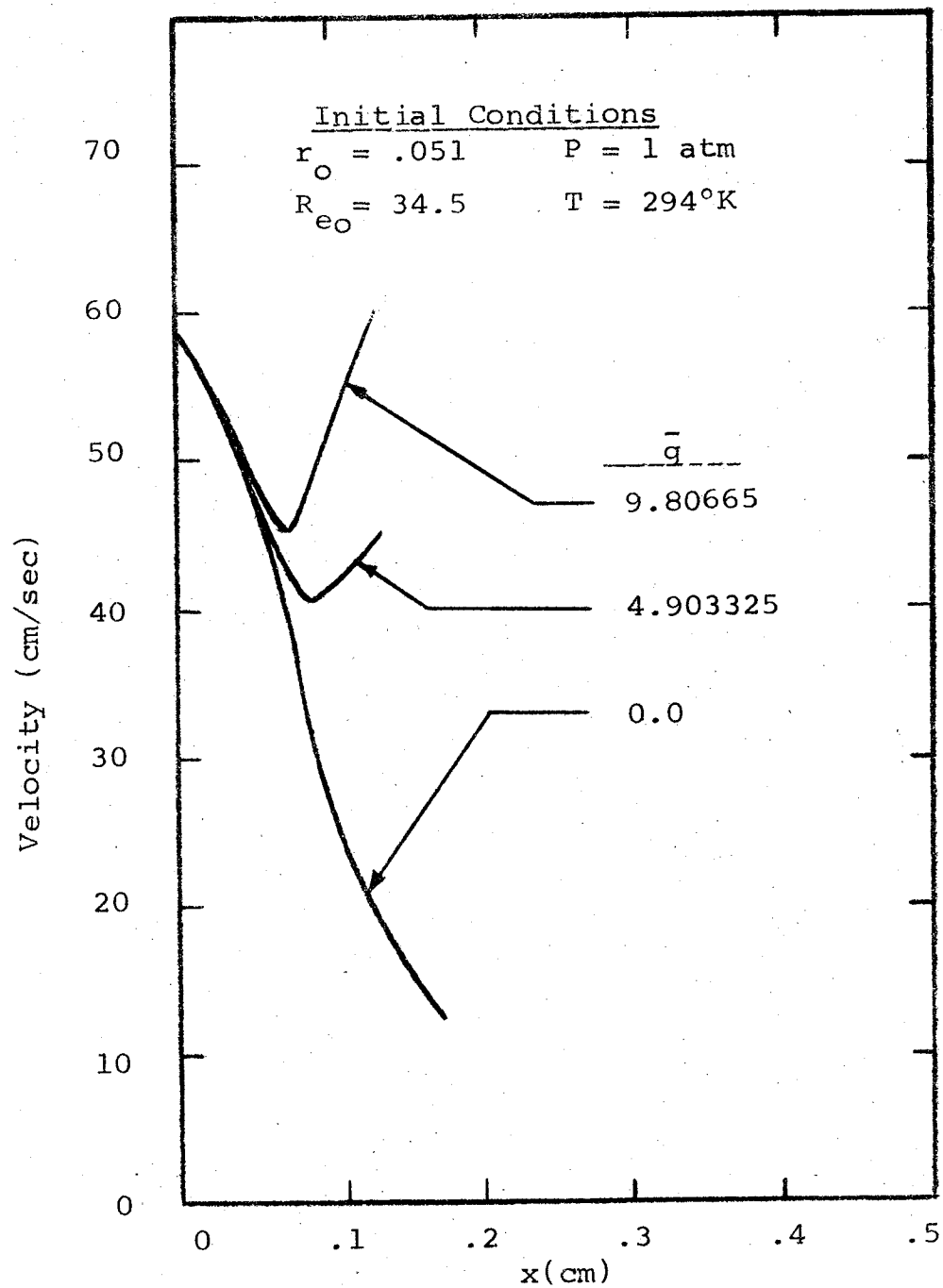


Figure 62. - Centerline velocity as a function of gravity level for propylene in an oxygen environment.

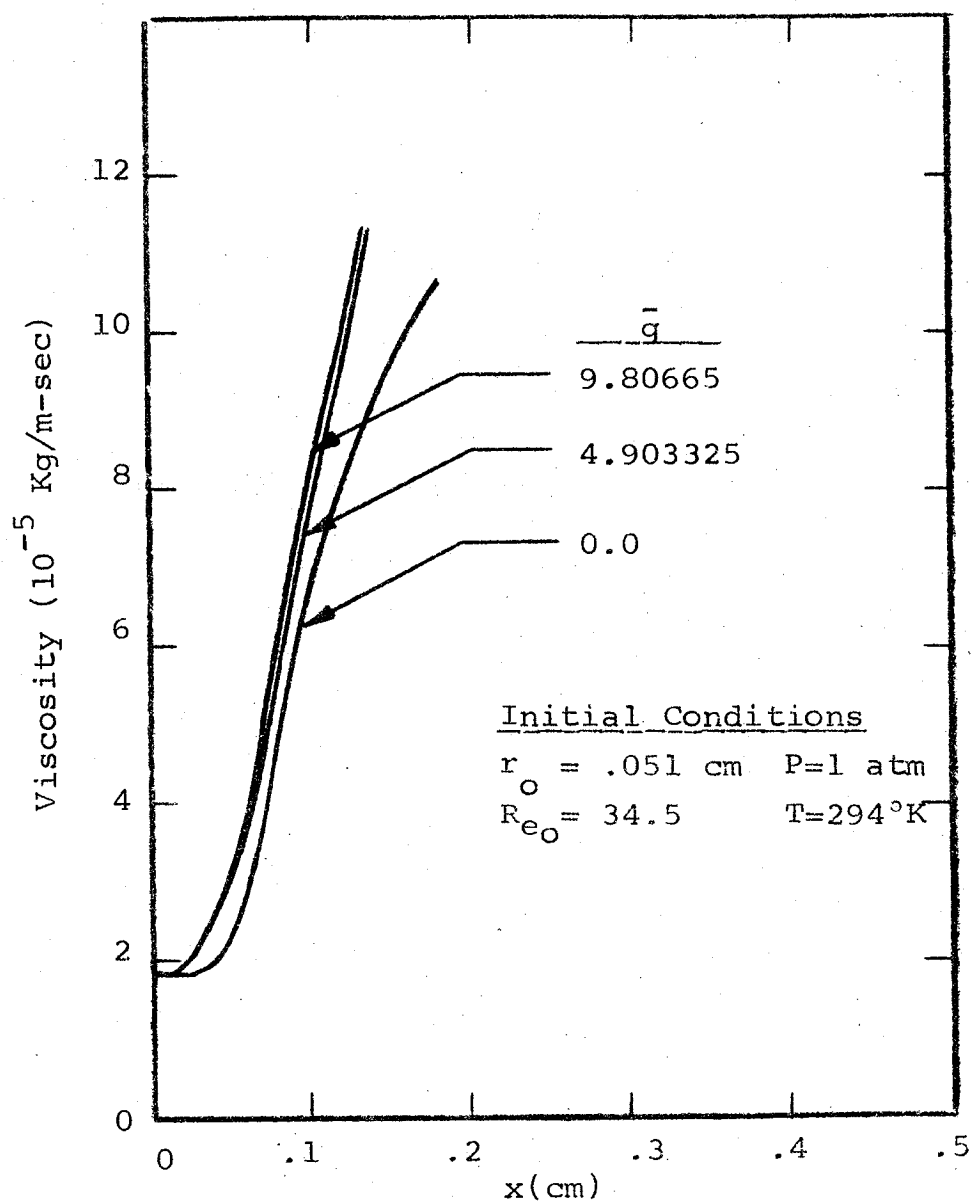


Figure 63. - Centerline viscosity as a function of gravity level for propylene in an oxygen environment.

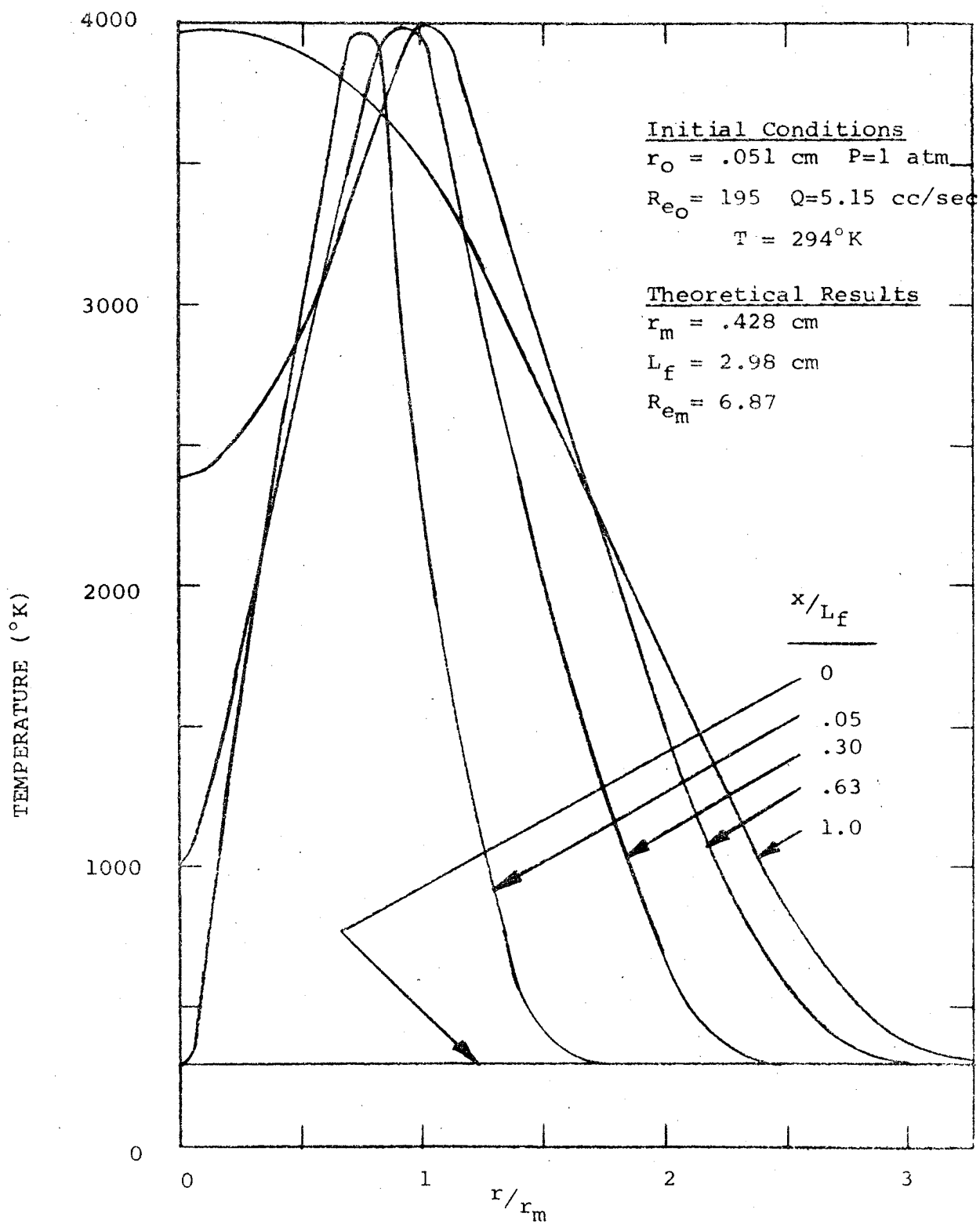


Figure 64. - Methane-50% oxygen evaluation case static temperature radial profiles.

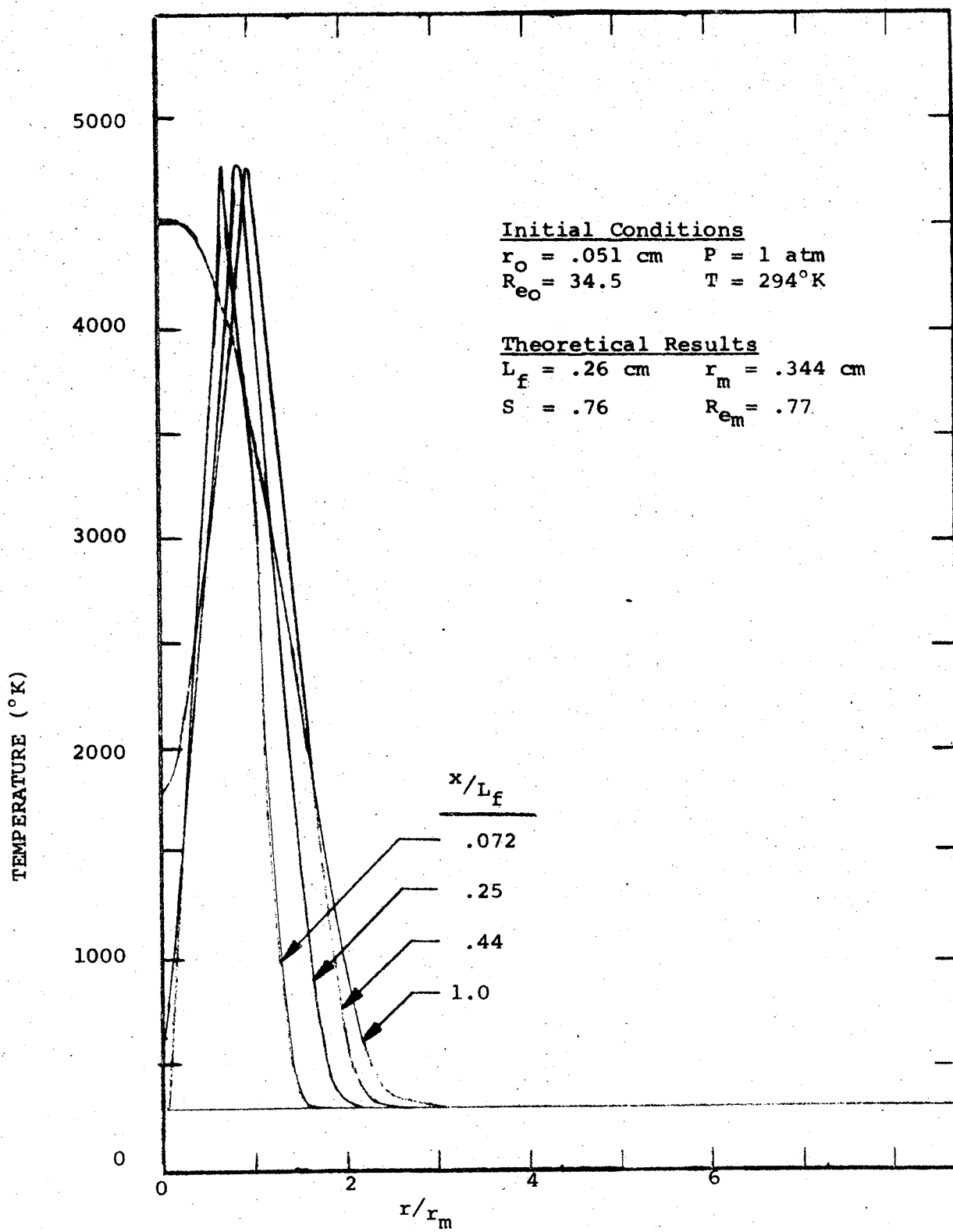


Figure 65. - Propylene-50% oxygen flame radial temperature profiles.

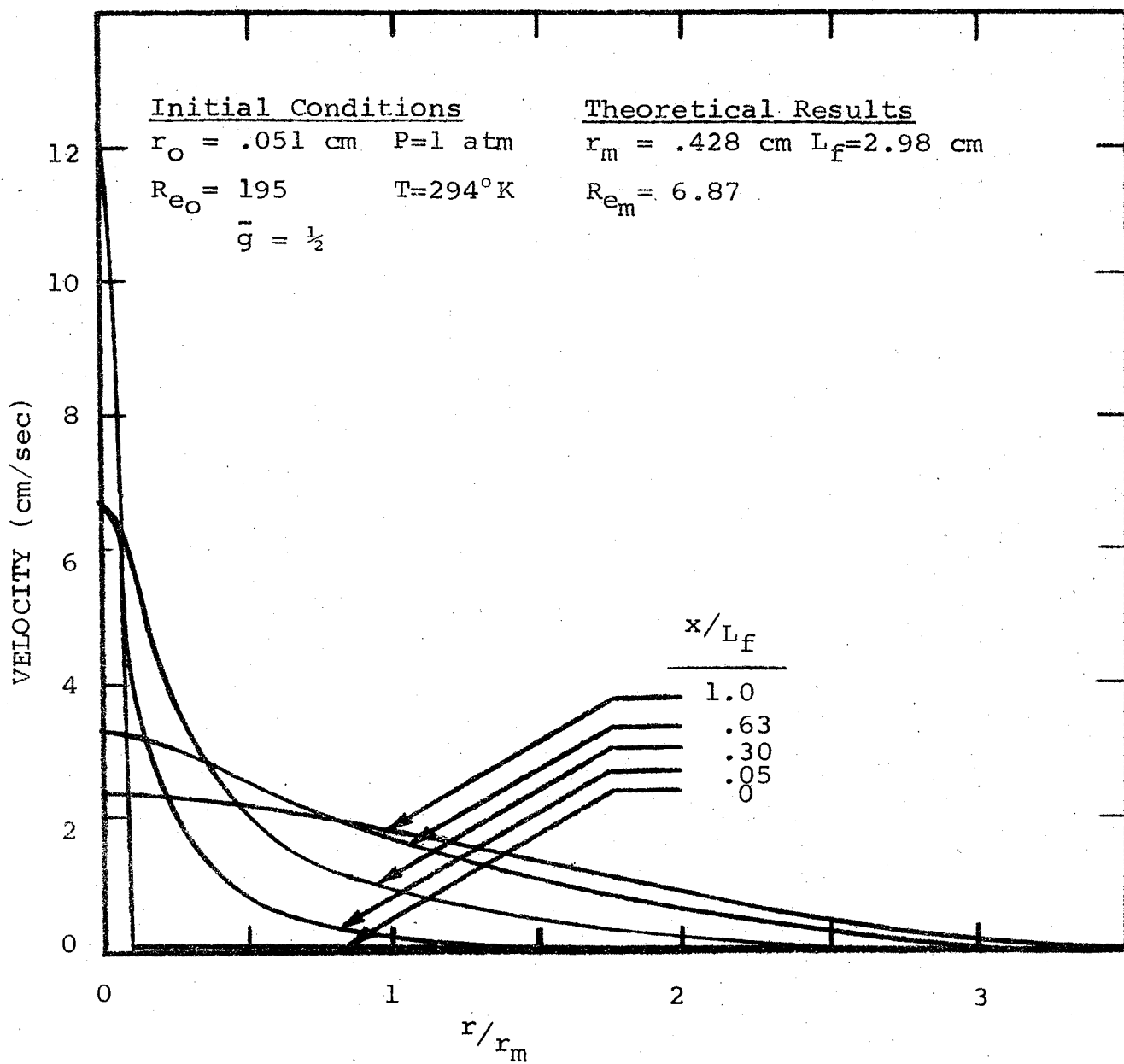


Figure 66. - Methane - 50% oxygen evaluation case velocity radial profiles.

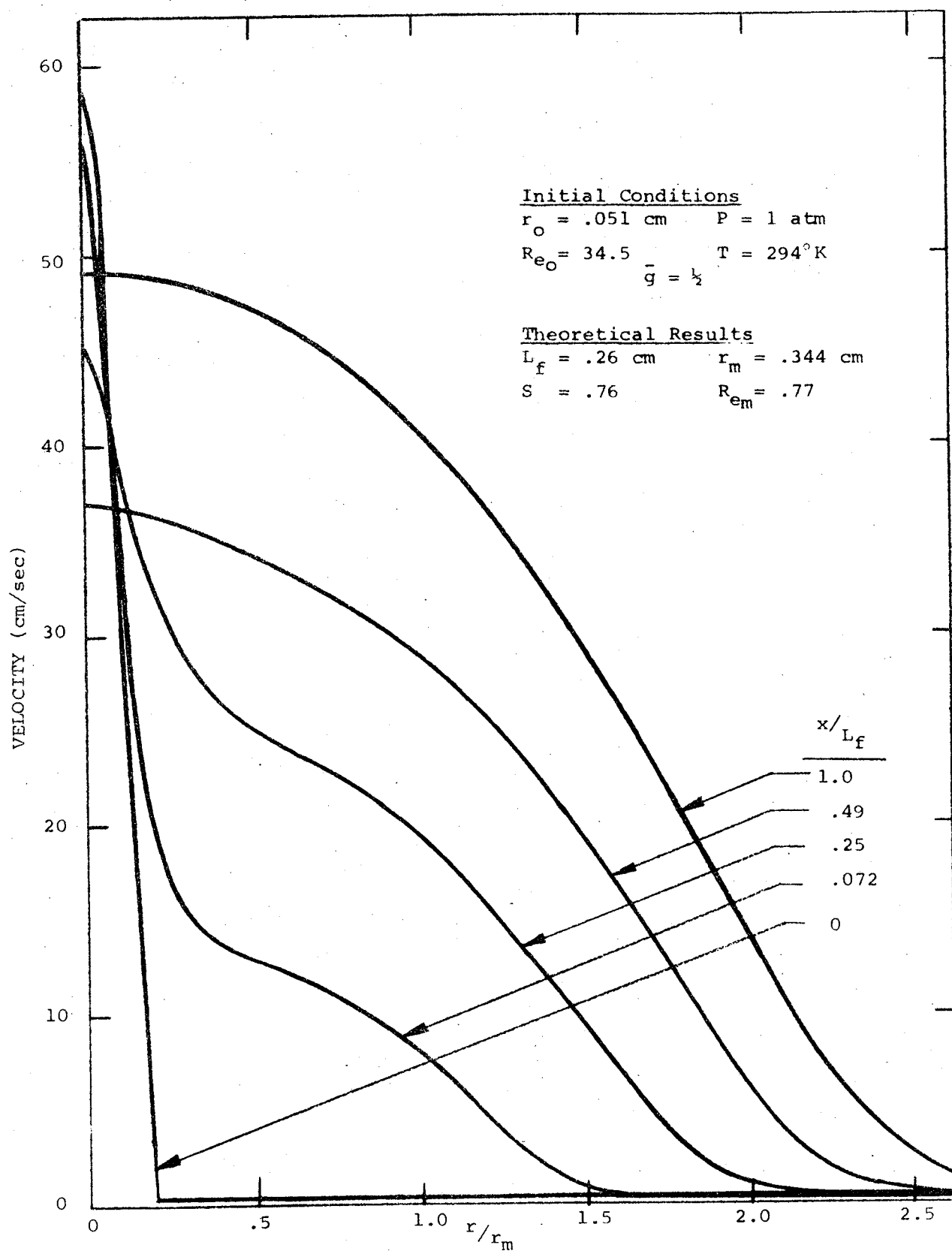


Figure 67. - Propylene-50% oxygen flame radial velocity profiles.

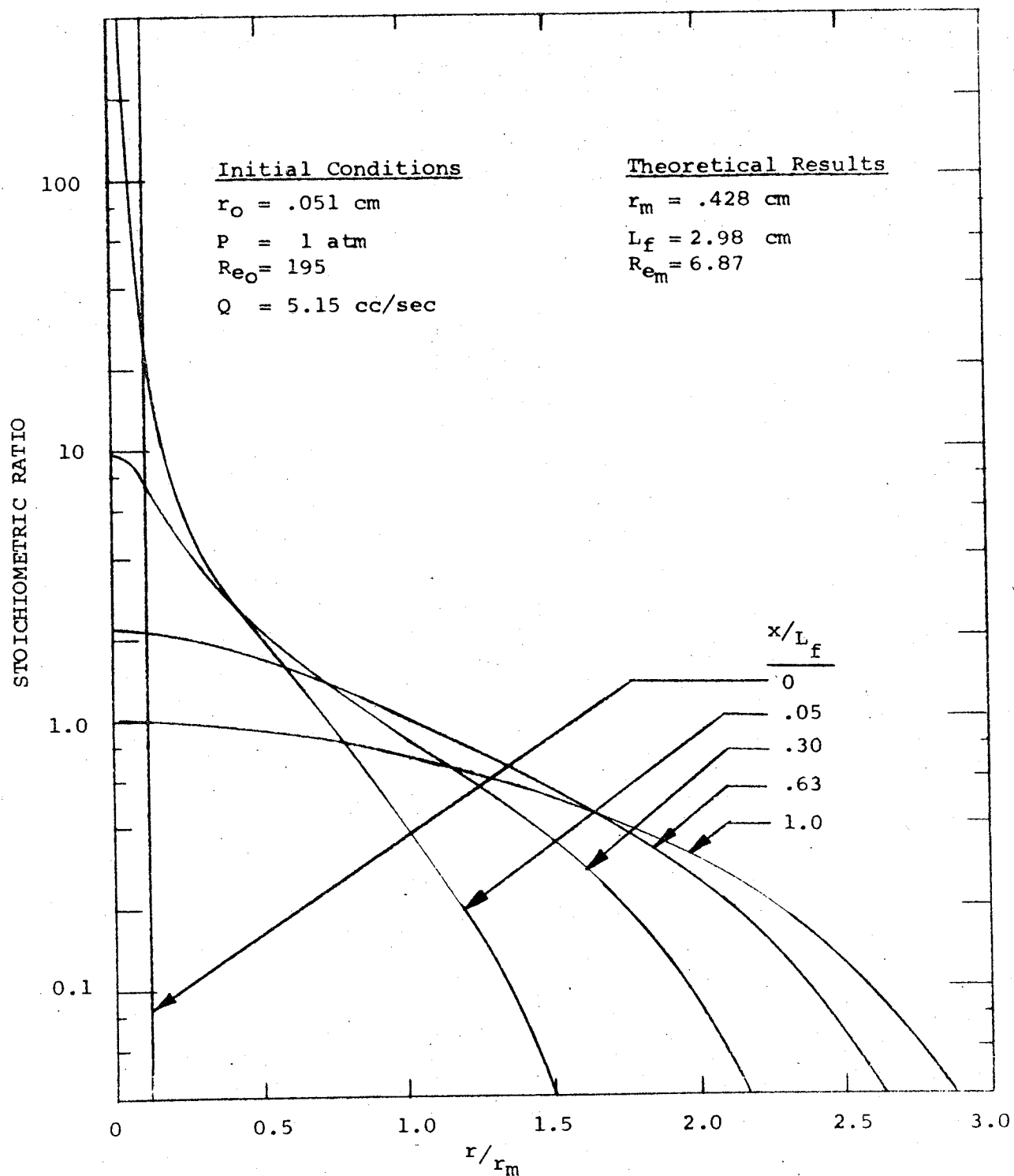


Figure 68. - Methane-50% oxygen evaluation case stoichiometric ratio radial profiles.

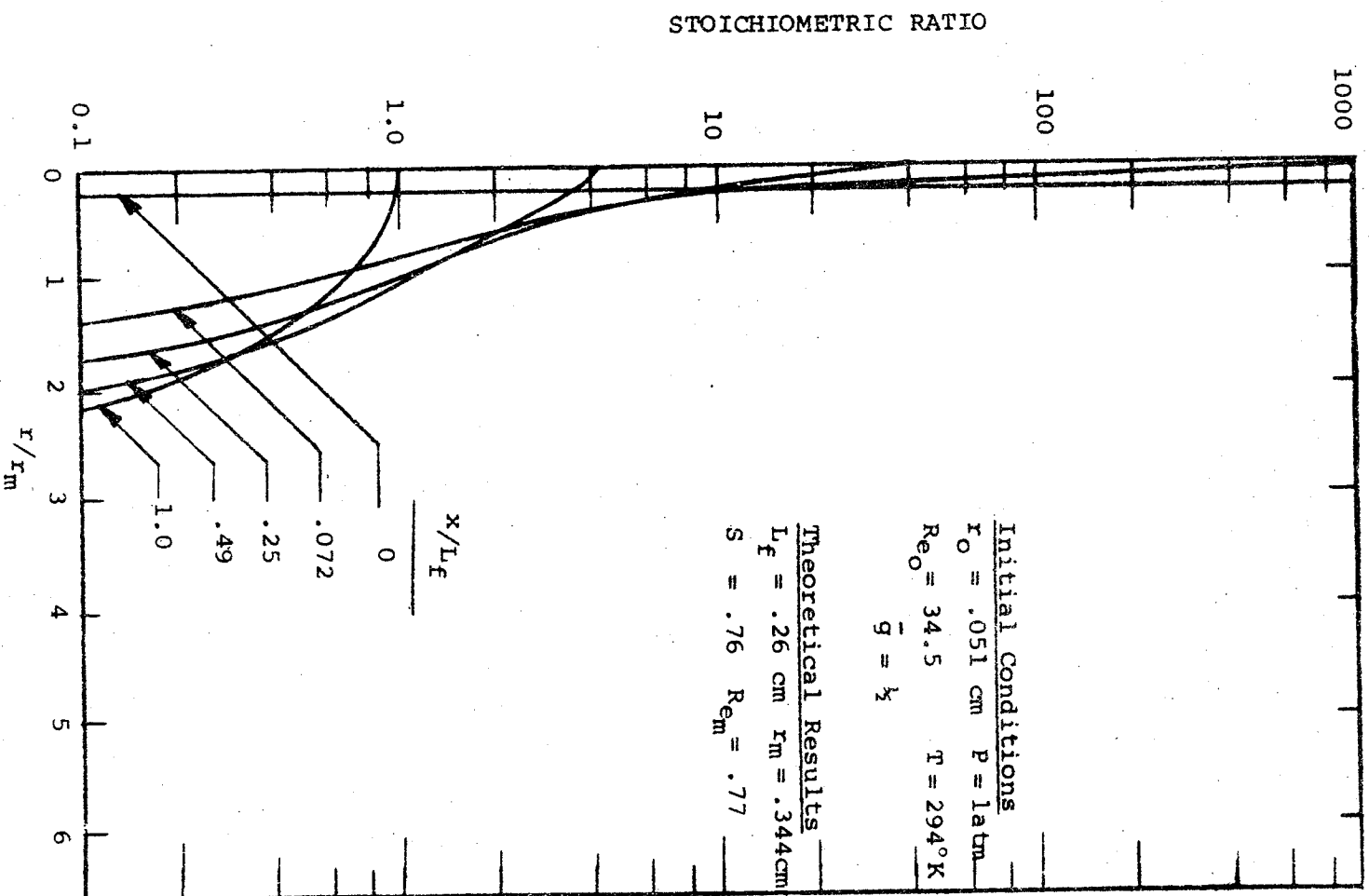


Figure 69. - Propylene-50% oxygen flame radial stoichiometric ratio profiles.

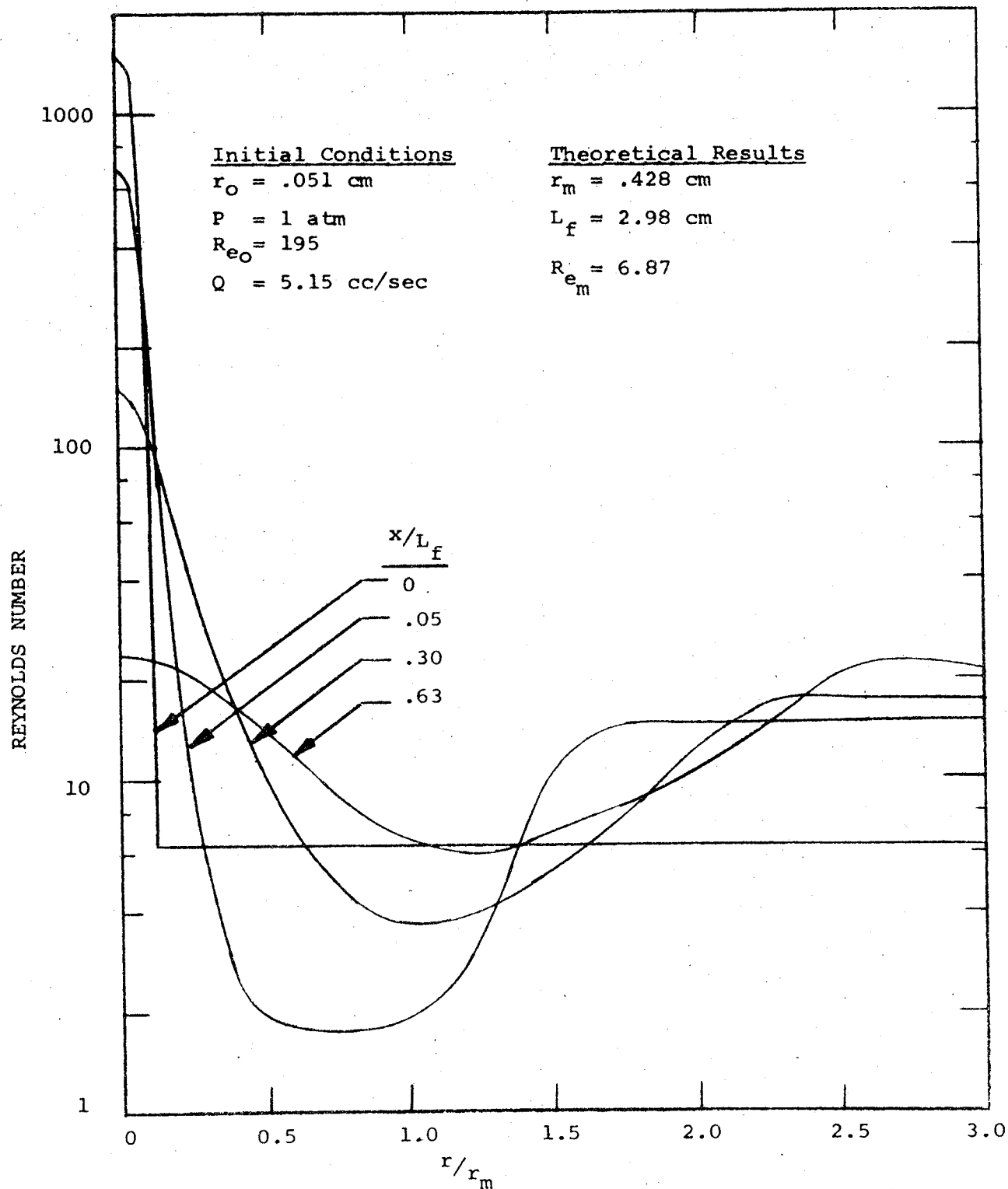


Figure 70. - Methane-50% oxygen evaluation case Reynolds number radial profiles.

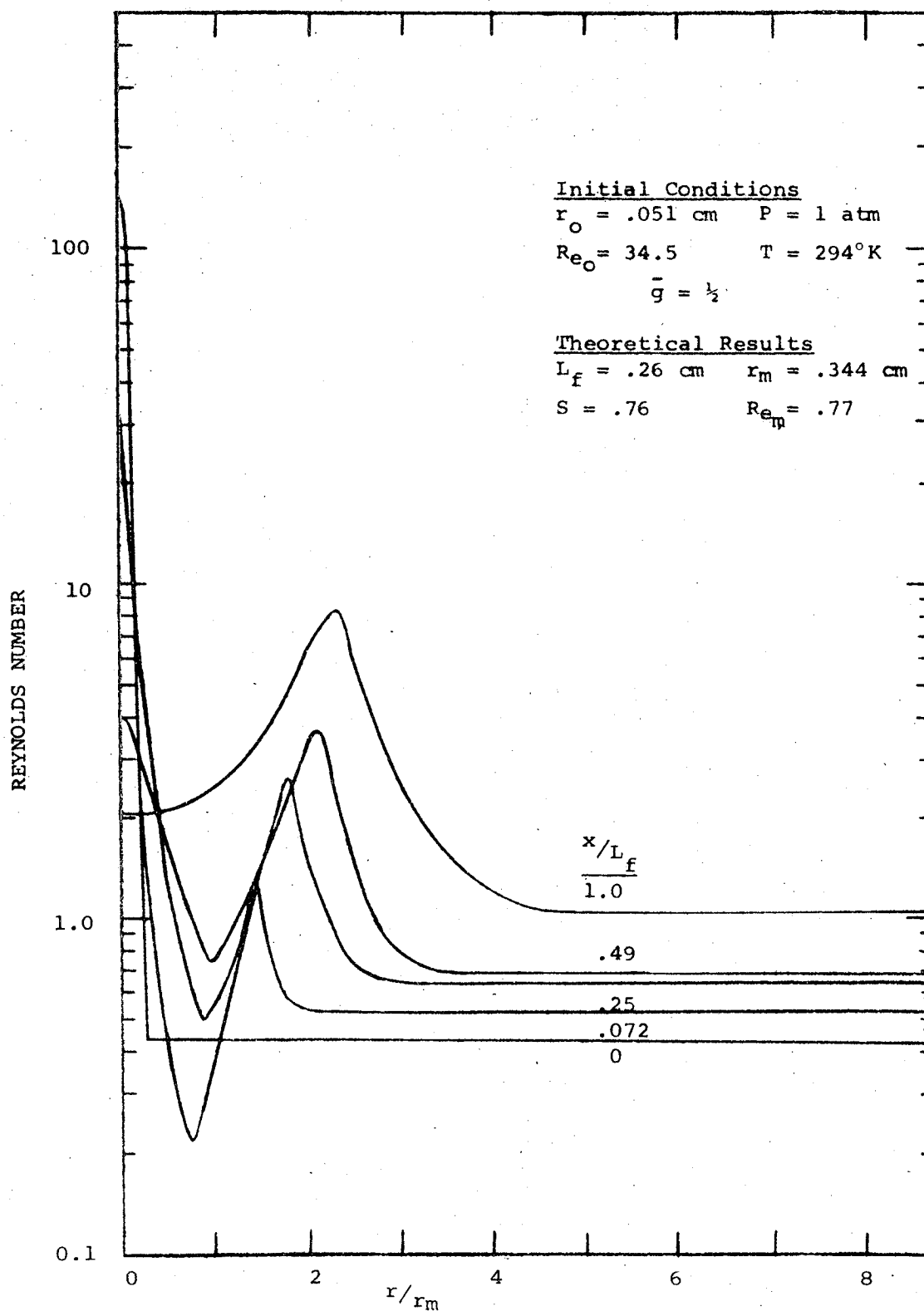


Figure 71. - Propylene-50% oxygen flame radial local Reynolds number profiles.

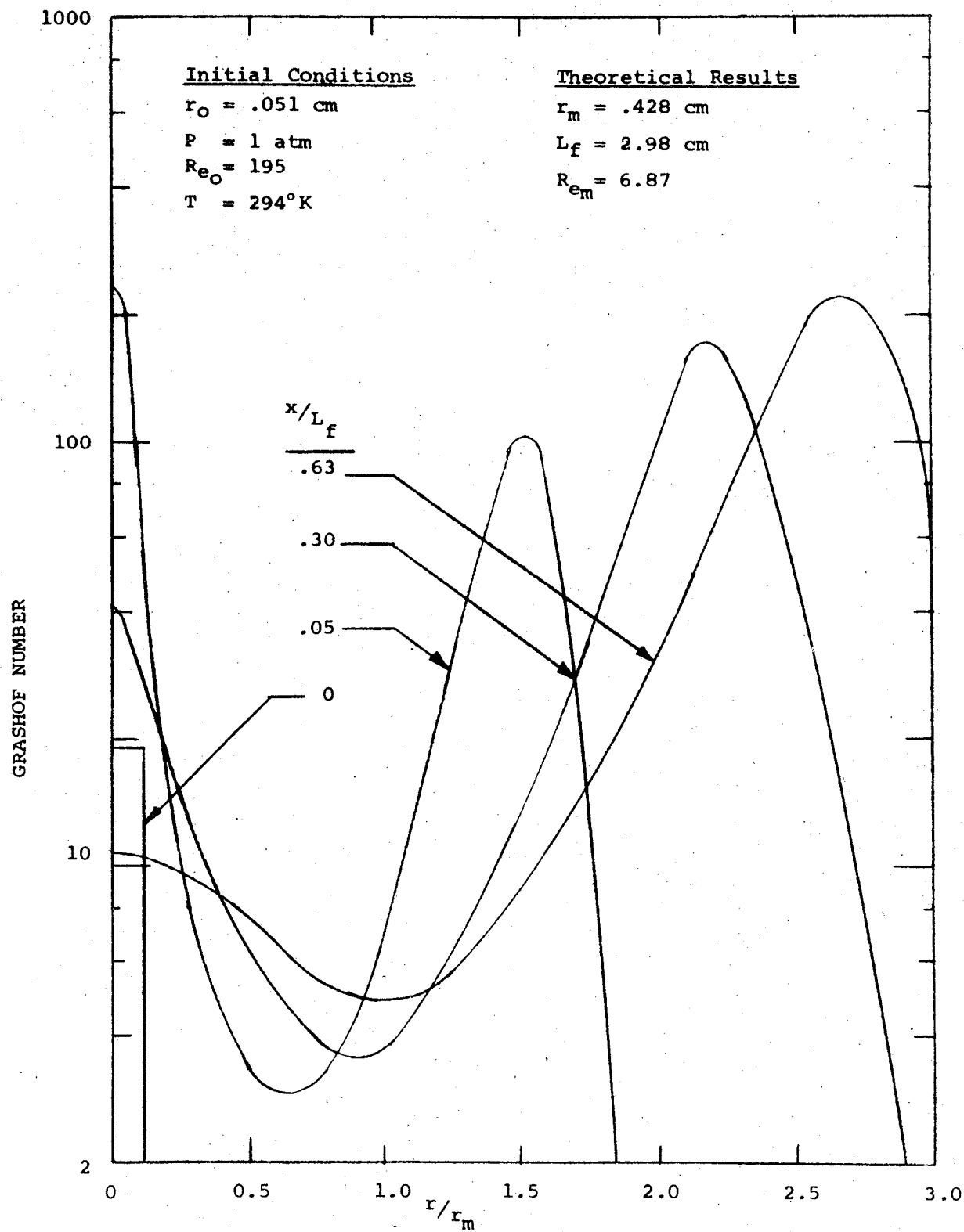


Figure 72. - Methane-50% oxygen evaluation case Grashof number radial profiles.

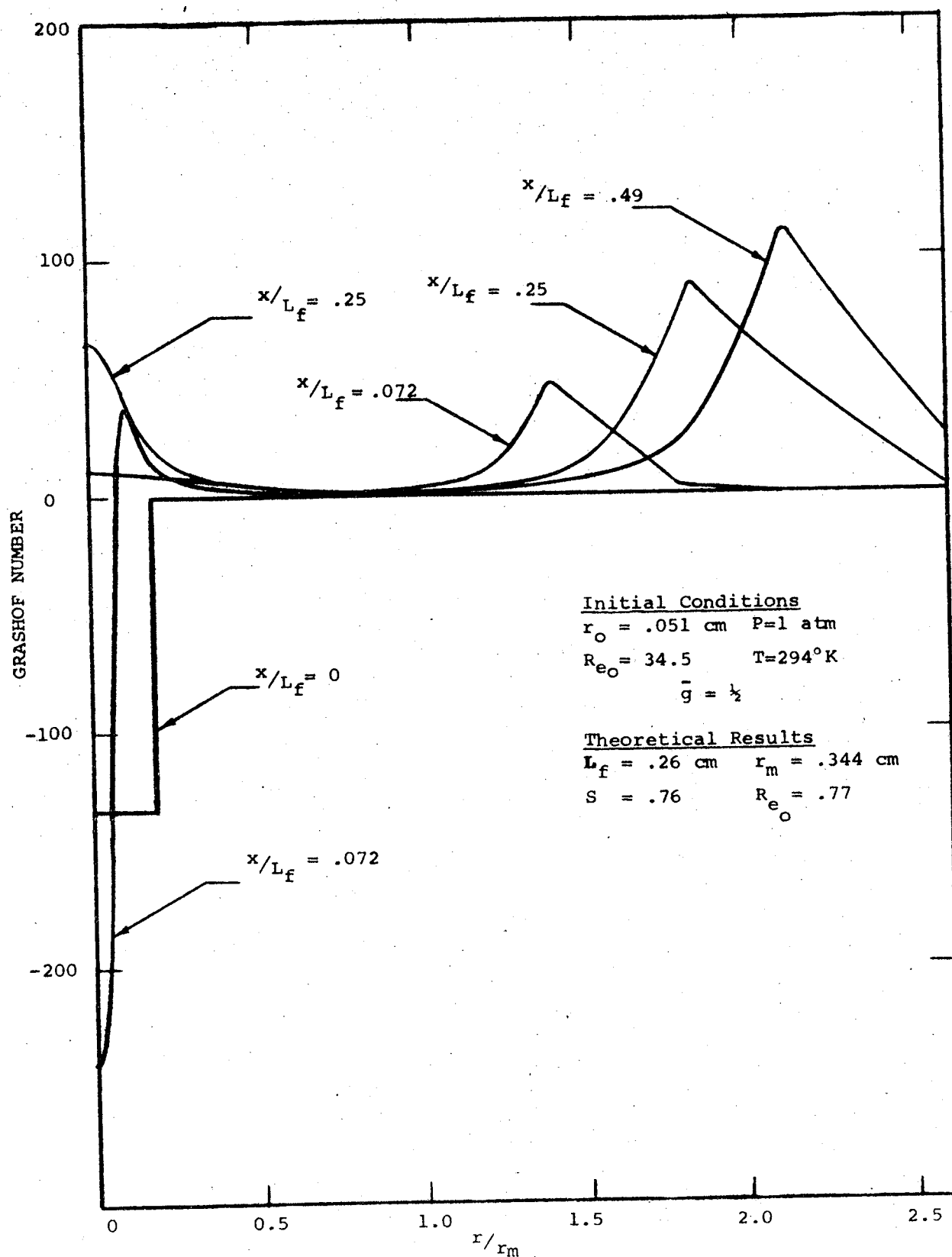


Figure 73. - Propylene-50% oxygen flame Grashof number radial profiles.

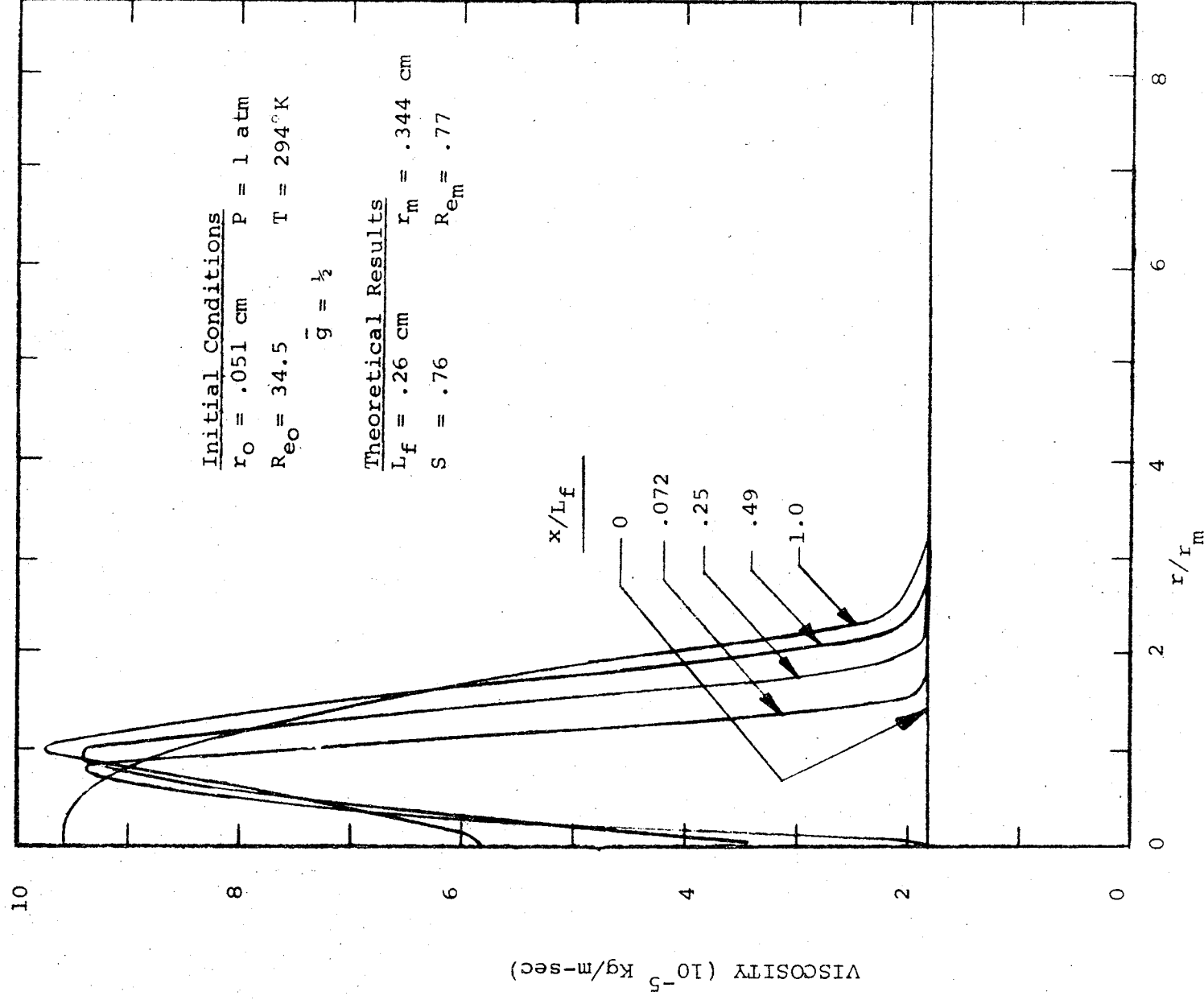


Figure 74. - Propylene-50% oxygen flame radial viscosity profiles

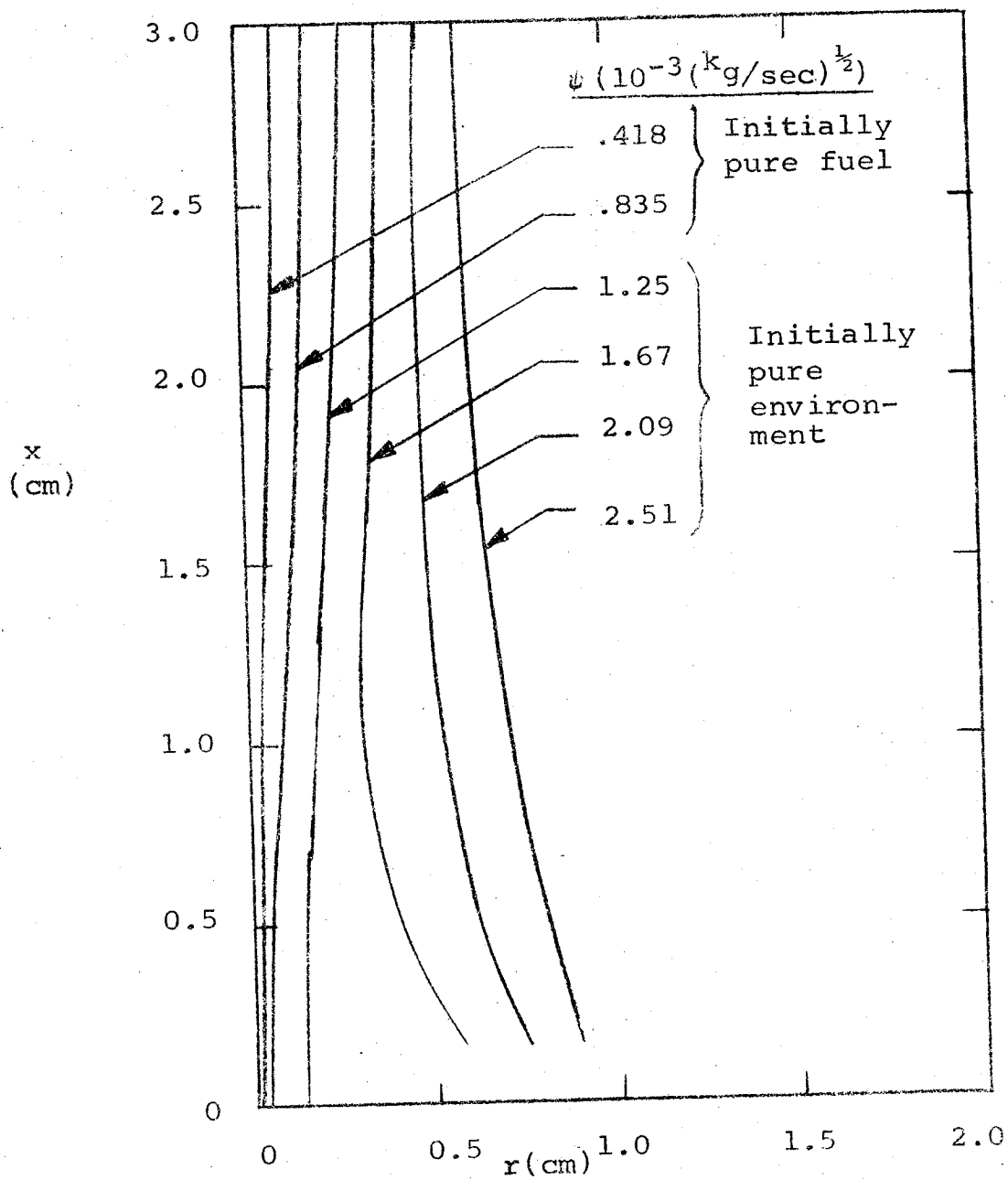


Figure 75. - Methane - 50% oxygen evaluation case flow field streamline map.

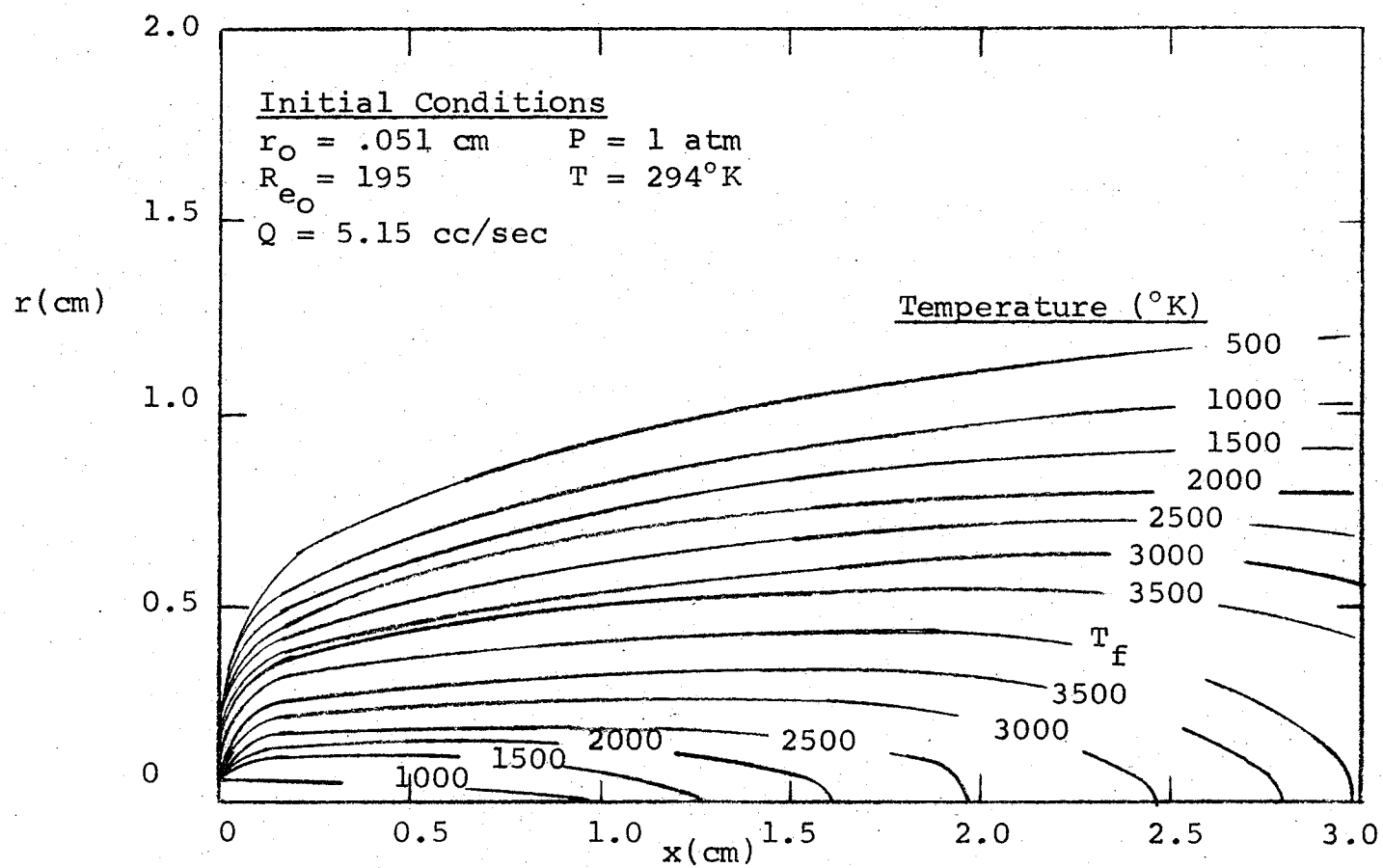


Figure 76. - Methane - 50% oxygen evaluation case flow field isotherm map.

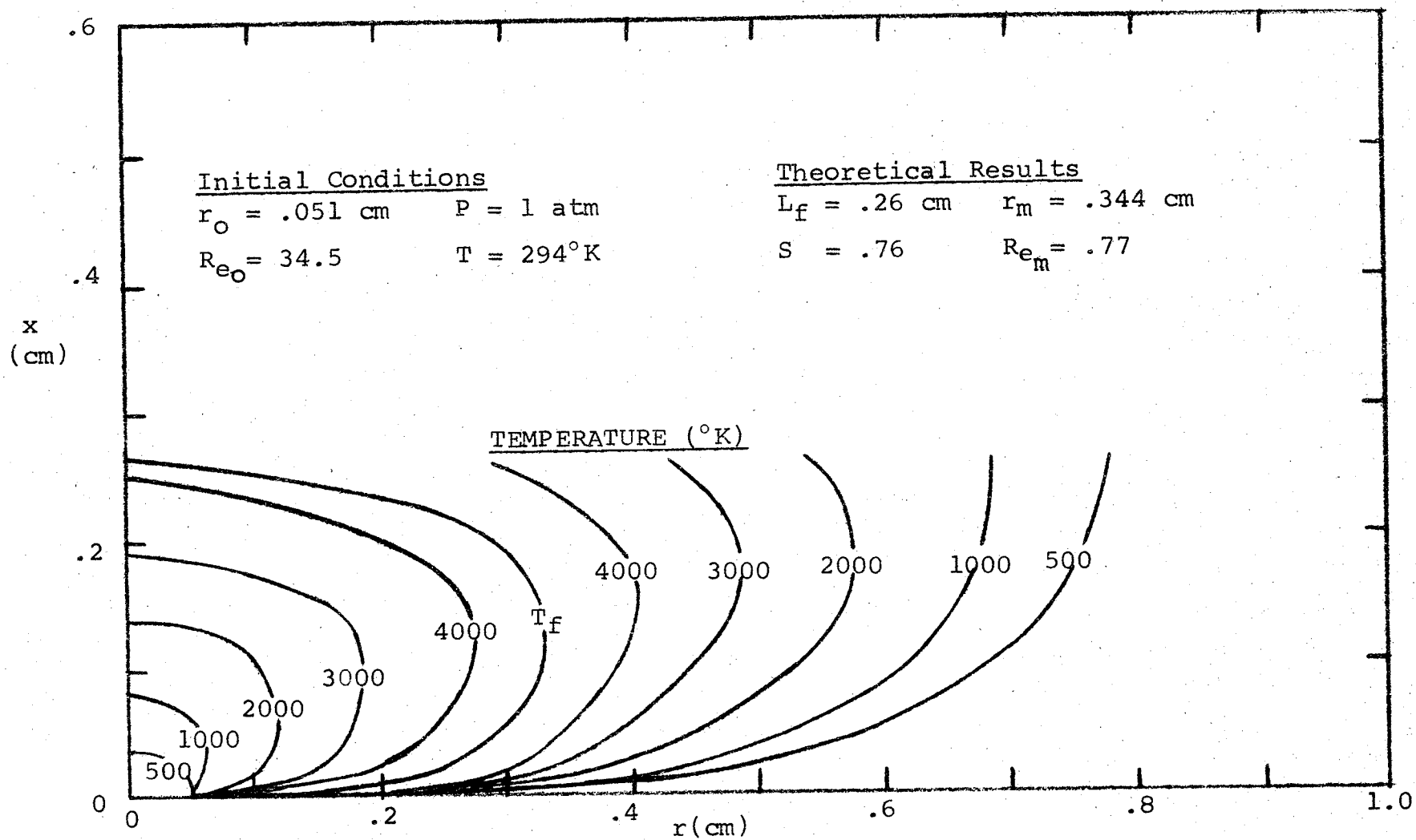


Figure 77. - Propylene-50% oxygen flame isotherm map of the calculated flow field.

DISTRIBUTION LIST FOR NASA CR-12092

	<u>Addressee</u>	<u>No. of Copies</u>
1.	National Bureau of Standards Fire Technology Division Building 225, Room A-45 Washington, D.C. 20234 Attn: Mrs. Miriam W. Rappaport	1
2.	NASA Scientific and Technical Information Facility Box 33 College Park, MD 20740 Attn: NASA Representative	2
3.	4043 Cody Road Sherman Oaks, CA 91403 Attn: Dr. Marvin Adelberg	1
4.	Southwest Research Institute Dept. of Mechanical Sciences P. O. Drawer 28510 San Antonio, TX 78284 Attn: H. Norman Abramson	1
5.	University of Kentucky Lexington, KY 40506 College of Engineering Attn: Dr. John Lienhard	1
6.	National Technical Information Service Springfield, VA 21151	40
7.	Factory Mutual Research Corporation 1151 Boston - Providence Turnpike Norwood, MA 02062 Attn: Dr. John deRis	1
8.	The Pennsylvania State University Combustion Laboratory, Fuel Science Section University Park, PA 16802 Attn: Dr. R. H. Essenhigh	1
9.	Princeton University Guggenheim Laboratories James Forrestal Campus Princeton, NJ 08540 Attn: Prof. Irvin Glassman	1

	<u>Addressee</u>	<u>No. of Copies</u>
10.	Cornell University College of Engineering, Sibley School of Mechanical Engineering Ithaca, NY 14850 Attn: Prof. B. Gebhard	1
11.	University of Massachusetts Department of Mechanical and Aero-Space Engineering Amherst, MA 01002	1
12.	Honeywell Corporate Research Center 500 Washington Avenue South Hopkins, MN 55343 Attn: Dr. Ulrich Bonne	1
13.	General Electric Company Valley Forge Space Technology Center P. O. Box 8555 Philadelphia, PA 19101 Attn: H. G. Lew	1
14.	Harvard University Division of Engineering and Applied Physics Cambridge, MA 02138 Attn: H. Emmons	1
15.	Atlantic Research Corporation Kinetics and Combustion Group, Propulsion Division Alexandria, VA 22314	1
16.	The Johns Hopkins University Applied Physics Laboratory 8621 Georgia Ave. Silver Spring, MD 20910 Attn: Dr. R. M. Fristrom	1
17.	TRW Systems Group Fluid Mechanics Laboratory One Space Park Redondo Beach, CA 90278 Attn: Dr. F. E. Fendell	1
18.	University of Illinois Dept. of Aeronautical and Astronautical Engineering Urbana, IL Attn: Dr. R. A. Strehlow	1
19.	Aero Thermo Corporation 485 Clyde Avenue Mountain View, CA 94040 Attn: Dr. R. M. Kendall	1

	<u>Addressee</u>	<u>No. of Copies</u>
20.	U. S. Army Aberdeen Research and Development Center Ballistic Research Laboratories Aberdeen Proving Ground, MD Attn: Warren W. Hillstrom	1
21.	Federal Aviation Administration National Aviation Facilities Experimental Center Atlantic City, NJ 08405 Attn: Charles M. Middlesworth	
22.	Air Force Aero Propulsion Laboratory Wright-Patterson Air Force Base, Ohio 45433 Attn: APFH/Benito P. Botteri	1
23.	U.S. Department of Commerce National Bureau of Standards Fire Technology Division Gaithersburg, MD 20760 Attn: G. King Walters	1
24.	U.S. Department of Commerce National Bureau of Standards Fire Technology Division Gaithersburg, MD 20760 Attn: Alexander F. Robertson	1
25.	U.S. Naval Research Laboratory Chemical Dynamics Branch Washington, D.C. 20390 Attn: Homer W. Carhart	1
26.	U.S. Department of the Interior Explosives Research Center Bureau of Mines 4800 Forbes Ave. Pittsburgh, PA 15213 Attn: Robert W. Van Dolah	1
27.	NASA-MSC White Sands Test Facility Post Office Drawer MM Las Cruces, NM 88001 Attn: Kenneth B. Gilbreath	1
28.	Lewis Research Center 21000 Brookpark Road Cleveland, OH 44135 Attn: Dr. I. Pinkel (M.S. 6-2) Thomas H. Cochran (M.S. 500/318)	2 50

	<u>Addressee</u>	<u>No. of Copies</u>
29.	NASA Headquarters Washington, D.C. 20546 Attn: MQ/Haggai Cohen DY/Morton Shaw DY/Daniel F. Hayes DY/Philip H. Bolger	 1 1 1 1
30.	NASA - KSC Kennedy Space Center, FL 32899 Attn: IS-PEM-1/Joel R. Reynolds IS-PEM-1/Norris C. Gray	 1 1
31.	NASA-Manned Spacecraft Center Houston, TX 77058 Attn: ES5/J. Howard Kimzey KS/ Richard W. Hautamaki KA/ Kenneth Kleinknecht PT/ Donald A. Arabian EA2/Aleck C. Bond	 1 1 1 1 1
32.	NASA-MSFC Marshall Space Flight Center, AL 35812 Attn: S&E-ASTN-M/Wilbur A. Riehl	 1
33.	NASA-Goddard Space Flight Center Greenbelt, MD 20777 Attn: Leopold Winkler	 1
34.	NASA-Ames Research Center Moffett Field, CA 94035 Attn: SC/John A. Parker SC/George M. Fohlen	 1 1